7-2024

Simulation of a Single Photon Counting Photonic Spectrograph for Direct Imaging of Exoplanet Atmospheres with the Habitable Worlds Observatory

Edwin Alexani
ea2191@rit.edu

Recommended Citation

Alexani, Edwin, "Simulation of a Single Photon Counting Photonic Spectrograph for Direct Imaging of Exoplanet Atmospheres with the Habitable Worlds Observatory" (2024). Thesis. Rochester Institute of Technology. Accessed from

Simulation of a Single Photon Counting Photonic Spectrograph for Direct Imaging of Exoplanet Atmospheres with the Habitable Worlds Observatory

---

M.S. *Master of Science*

in Astrophysical Sciences and Technology

Edwin Alexani

School of Physics and Astronomy

Rochester Institute of Technology

Rochester, New York

July 2024

RIT | College of Science
Astrophysical Sciences and Technology

CERTIFICATE OF APPROVAL

MASTER'S DEGREE THESIS

The Master's Degree Thesis of Edwin Alexani has been examined and approved by the thesis committee as satisfactory for the dissertation requirement for the Master of Science degree in Astrophysical Sciences and Technology.

Dr. Donald F. Figer, Thesis Advisor

Dr. Zoran Ninkov, Committee Member

Dr. Michael Zemcov, Committee Member

Date________________________________

RIT | College of Science
Astrophysical Sciences
and Technology

SIMULATION OF A SINGLE PHOTON COUNTING PHOTONIC SPECTROGRAPH FOR DIRECT IMAGING OF EXOPLANET ATMOSPHERES WITH THE HABITABLE WORLDS OBSERVATORY

By

Edwin Alexani

A Thesis Submitted in Partial Fulfillment of the
Requirements for the Degree of Master of Science in
Astrophysical Sciences & Technology

School of Physics and Astronomy
College of Science
Rochester Institute of Technology
Rochester, NY

July 2024

Approved by:__________________________________ _____
Andrew Robinson, Ph.D Date
Director, Astrophysical Sciences and Technology

Abstract

NASA's highest-priority future flagship astrophysics mission is a large infrared/optical/ultraviolet (IR/O/UV) telescope, the first in a series of new Great Observatories recommended by the 2020 Decadal Survey. The current concept for this telescope is the Habitable Worlds Observatory (HWO), drawing on past design projects such as LUVOIR and HabEx. A key goal for HWO is to identify habitable exoplanets. The HWO will obtain spectra and direct images of distant, dim worlds, necessitating highly sensitive instruments. The HWO will require a coronagraph that achieves a 10^{-10} contrast ratio to suppress the starlight and reveal terrestrial exoplanets. The detector's dark current and read noise must be extremely low to enable high contrast imaging of terrestrial exoplanets, from which only a few photons per hour reach the telescope. These requirements have created a need for single photon counting detectors for HWO.

This paper presents the instrument requirements and design for an optical single photon counting photonic spectrograph (SPCPS) based on simulated observations of an earthlike exoplanet atmosphere. The SPCPS incorporates emerging technologies: a single photon counting CMOS detector and an on-chip astrophotonic spectrograph, the latter offering a smaller and lighter instrument compared to traditional spectrographs. This project identifies the stellar parameter space within which direct imaging of exoplanets in the local galactic neighborhood (∼50 pc) would be possible with HWO. The integration time to reach a desired spectral signal-to-noise ratio (SNR) of the O_2-A band biosignature at 760 nm is determined by using the Earth to simulate exoplanet atmospheric observations around different stars. The integration time and SNR are the key criteria for optimizing the SPCPS system. Initial findings suggest that the SPCPS achieves an SNR of 10 with a 45% error on the equivalent width of the O_2-A band in $\sim 10^3$ hours. This work assesses design requirements for the SPCPS for exoplanet atmosphere characterization and suggests future improvements for design and model considerations.

Contents

List of Figures

List of Tables

Chapter 1

Introduction

The Habitable Worlds Observatory (HWO) is one of NASA's anticipated future IR/O/UV Great Observatories for astrophysics. The 2020 Decadal Survey defines the search for habitable exoplanets as one of HWO's main goals [1]. HWO draws characteristics from both the Habitable Exoplanet Observatory (HabEx) and the Large Ultraviolet Optical Infrared Surveyor (LUVOIR) mission concepts [2] [3].

The HWO aims to directly image habitable worlds and analyze their spectra. Direct imaging is a promising method for finding habitable exoplanets but requires high contrast imaging (HCI) [4] [5]. One tool for achieving HCI is a coronagraph. For a typical Earth twin orbiting a solar analog in the stellar neighborhood (~ 10 pc), the coronagraph must provide a contrast of 10^{-10} for HCI [2] [3]. Despite starlight suppression to increase the signal-to-noise ratio, the exoplanet signal consists of only a few photons per hour, necessitating detectors with extremely low read noise and dark current [6] [7] [8]. Additionally, the spectrograph must have enough resolution to detect biosignatures. While traditional spectrographs can achieve the required resolution, their designs typically feature large and massive optics. For instance, the LUVOIR ECLIPS instrument is expected to weigh about 1000 kg [3] [9].

CMOS single photon counting detectors (SPCD) and on-chip astrophotonic spectrographs (APS) are new, compact, and promising technologies to integrate with the HWO flagship. Commercial CMOS SPCDs are sensitive and widely available, and APS may significantly reduce the size and weight of instruments, thereby lowering mission costs. Combining an SPCD and APS into a single photon counting photonic spectrograph (SPCPS) could reduce the weight and size of future flagship observatories while maintaining the detectability of science targets. As current efforts continue to inform the design of HWO, the available LUVOIR-B mission concept is selected in this study [3]. Using a simulated observation of an Earth twin, we estimate the SNR required to detect the O_2-A absorption band and the SNR achievable by the system. The SNR and exposure time requirements then flow down into the instrument design. This paper presents a simulated observation of an Earth twin with an 8-meter class telescope (LUVOIR-B) equipped with a coronagraph and an SPCPS, and addresses areas of improvement for the design and models.

1.1 Exoplanets and Where to Find Them

Since the discovery of exoplanets at the turn of the century, NASA has confirmed the detection of 5,678 exoplanets[1]. The transit method is the most successful at finding exoplanets thus far. However, the transit method favors short orbital periods, Super-Earths, and Sub-Neptunes. To detect an Earth twin around a Sun-like star, direct imaging will be required. This detection method will provide results for many of the HWO science cases. Habitable exoplanets with liquid water on their surface are expected to be found in the habitable zone of their host star. The water would likely appear in the atmosphere as one of many biosignatures. Biosignatures are gases that may indicate the presence of life (carbon-based) on an exoplanet. A prominent biosignature in Earth's spectrum is the O_2-A band at 760 nm. Current oxygen levels on Earth are maintained by photosynthesis, a biological process. Therefore, the O_2-A band will be used as the case study in this paper.

---

[1] `https://exoplanetarchive.ipac.caltech.edu/docs/counts_detail.html`, numbers reported here have likely changed on the website.

1.1.1 Detection Methods and Exoplanet Types

The primary exoplanet detection methods are transit, radial velocity, gravitational microlensing, and direct imaging. A full list of detection methods with corresponding results is provided in Table 1.1. The transit method has found 4,216 exoplanets to date, 74.25% of all confirmed exoplanets. In edge-on systems, planets transit in front of the host star, causing a measurable and cyclical decrease in the star's brightness. The transit depth and the duration provide information about the planet's radius and orbital velocity. The transit method typically detects planets with short orbital periods, as these offer multiple transit events to confirm the planet's presence over short observation times. Potentially habitable rocky planets have been discovered by transit, notably those around the M-dwarf TRAPPIST-1. This compact system is suitable for discovery by transit but susceptible to tidal locking which may affect habitability [10] [11], especially around flaring M-dwarfs.

Table 1.1: Exoplanet Detection Methods and Yields

Method	Number Confirmed	Percentage
Transit	4216	74.25
Radial Velocity	1089	19.18
Microlensing	222	3.91
Imaging	82	1.44
Transit Timing Variations	29	0.51
Eclipse Timing Variations	17	0.30
Orbital Brightness Modulations	9	0.16
Pulsar Timing Variations	8	0.14
Astrometry	3	0.05
Pulsation Timing Variations	2	0.04
Disk Kinematics	1	0.02
Total	5678	100

Values from `https://exoplanetarchive.ipac.caltech.edu/docs/counts_detail.html` are likely to change from the time of writing.

Transits most frequently find Super-Earths and Sub-Neptunes in close proximity to the host star [12]. This effect is apparent in Figure 1.1. The exoplanets are classified in Figure

1.2. The classification scheme used here is loosely inspired from [13] and [14], the main purpose is to highlight the abundance of Super-Earths (defined here as $1.4R_\oplus$ - $2R_\oplus$) and Sub-Neptunes (defined here as $2R_\oplus$ - $3R_\oplus$). This classification is based solely on the planet's radius. The 2023 Exoplanet Exploration Program Science Gap List [13] defines Earth-sized planets as having a radius between $0.8R_\oplus$ - $1.4R_\oplus$, while [14] defines Earths as $0.5R_\oplus$ - $1R_\oplus$, underscoring the lack of a universally accepted exoplanet classification scheme.

The radial velocity method is the second most successful and has confirmed 1,089 exoplanets. It measures the Doppler shift in the stellar light caused by the gravitational influence of a planet on its parent star [5]. This method favors Hot Jupiters, which are massive and close to their star, thus exerting a greater measurable gravitational tug. This bias is illustrated in Figures 1.3 and 1.4.

While the transit and radial velocity methods have found the most planets to date, they do not yield many potentially earthlike habitable planets. Terrestrial planets have lower size, mass, and luminosity compared to Super-Earth and Sub-Neptune, decreasing the probability of detection by transit and radial velocity [4]. Additionally, these detection methods are biased against larger orbits, where the habitable zone typically lies for most stellar types. For instance, an Earth twin orbiting the Sun has only a 0.5% chance of transiting due to the larger orbit, thus motivating the need for direct imaging, as described in [15].

Only 373 exoplanets (6.57%) have been found using other methods, with 82 directly imaged planets. Of those 82, only 29 exoplanets have radius data, and all are Jupiter-sized objects. Most of these planets were imaged from ground-based telescopes such as the Paranal, W. M. Keck, Gemini, Palomar, and Las Campanas Observatories, and the Subaru Telescope. A few have also been observed by the Hubble Space Telescope, James Webb Space Telescope, and Spitzer. However, the high contrast imaging capabilities of these telescopes are not yet at the level required for HWO, and thus favor Hot Jupiters [5] [16].

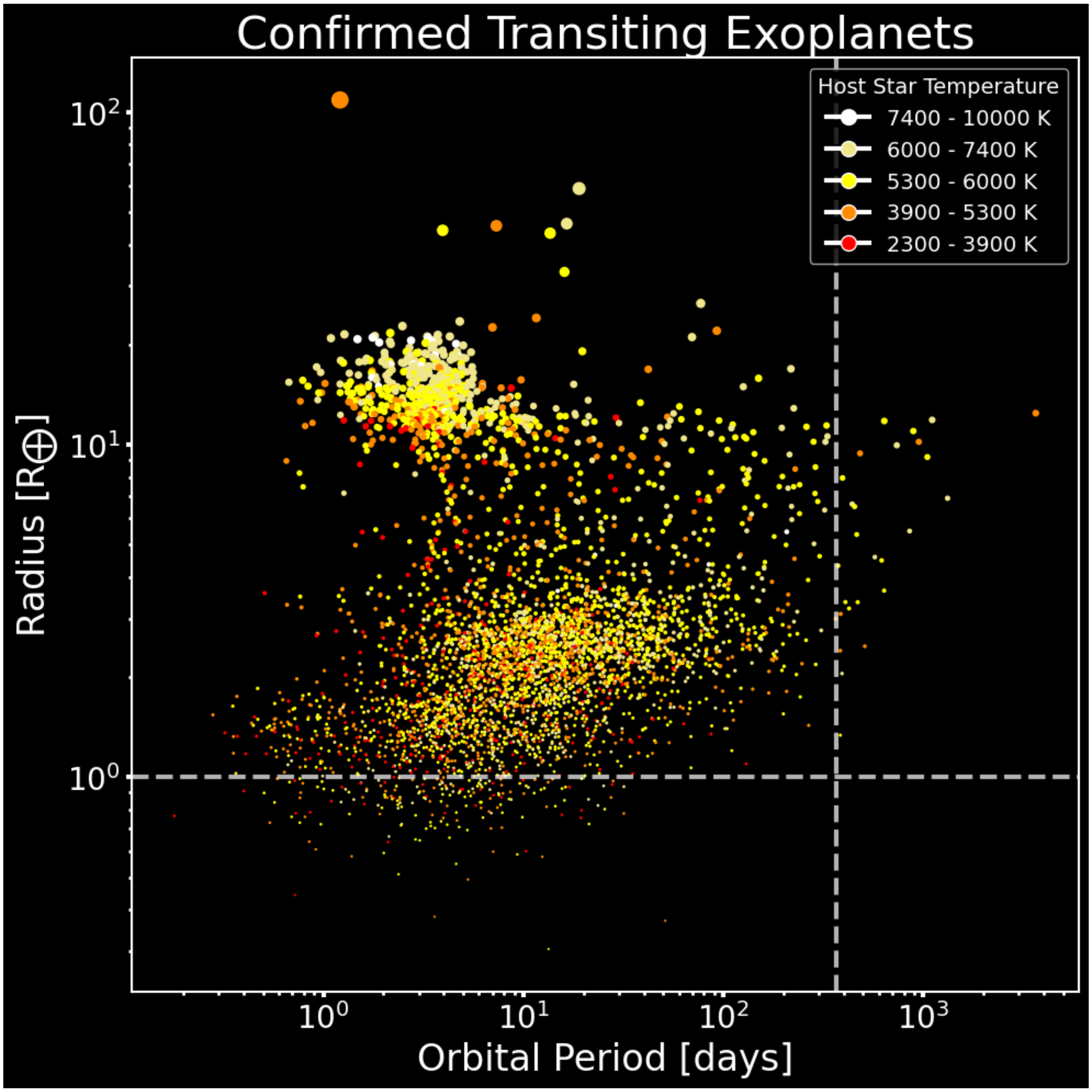

Figure 1.1: The plot above shows 4,234 exoplanets confirmed by the transit detection method. The colors represent the temperature of the stellar host. Hot Jupiters are clustering in the upper left, and Super-Earths and Sub-Neptunes ($1.4R_\oplus$ - $3R_\oplus$) are clustering in the middle. The dashed lines represent the Earth's radius and orbital period. Notice the paucity of exoplanets near the Earth's parameter space.

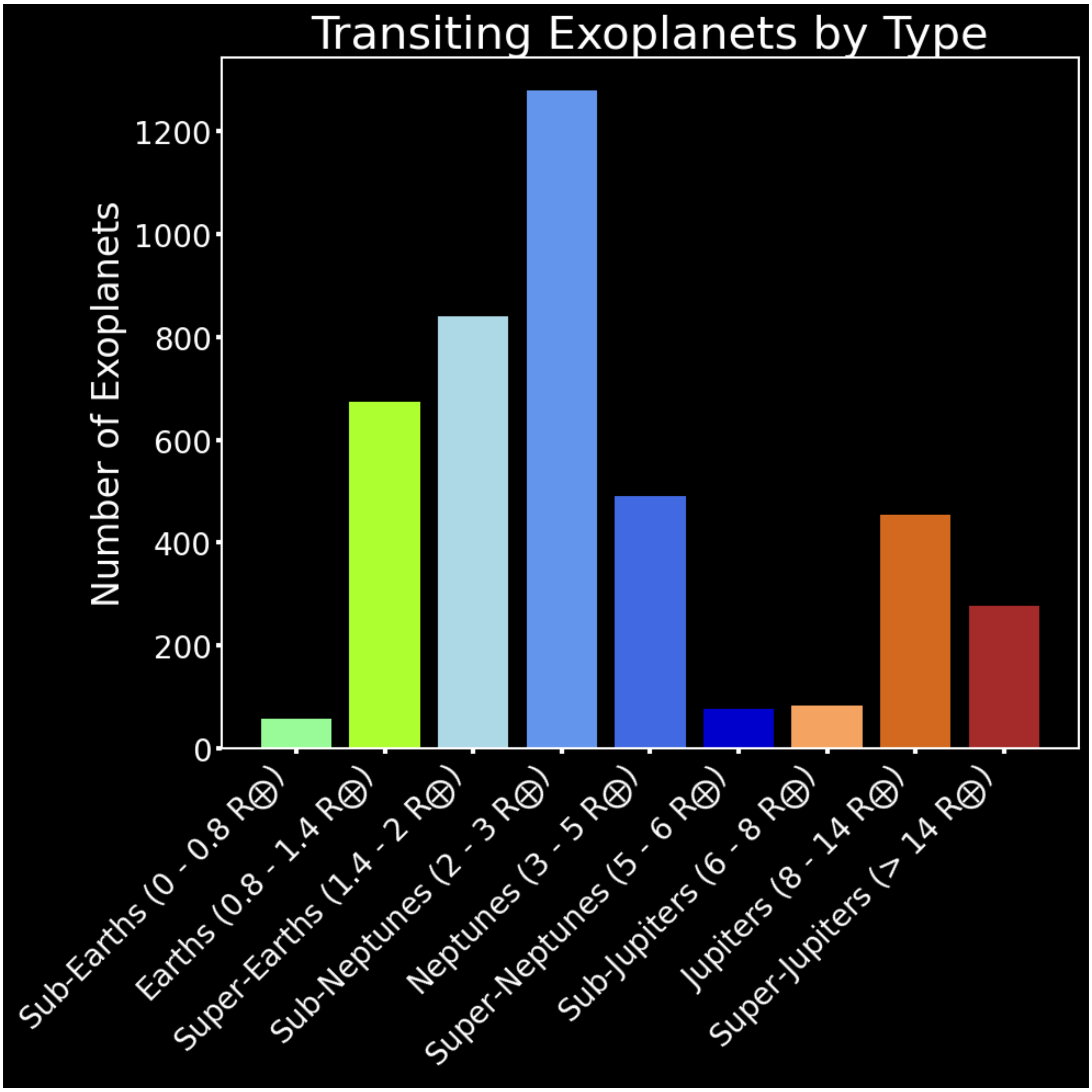

Figure 1.2: The histogram above shows 4,234 exoplanets confirmed by the transit detection method. The planets are categorized using only their radius. The majority of exoplanets confirmed by transit are in the Super-Earth and Sub-Neptune categories. There are no such known equivalent planets in our solar system. The majority of all planets in this plot orbit their Sun-like host star in less than 100 days, and are thus out of the habitable zone.

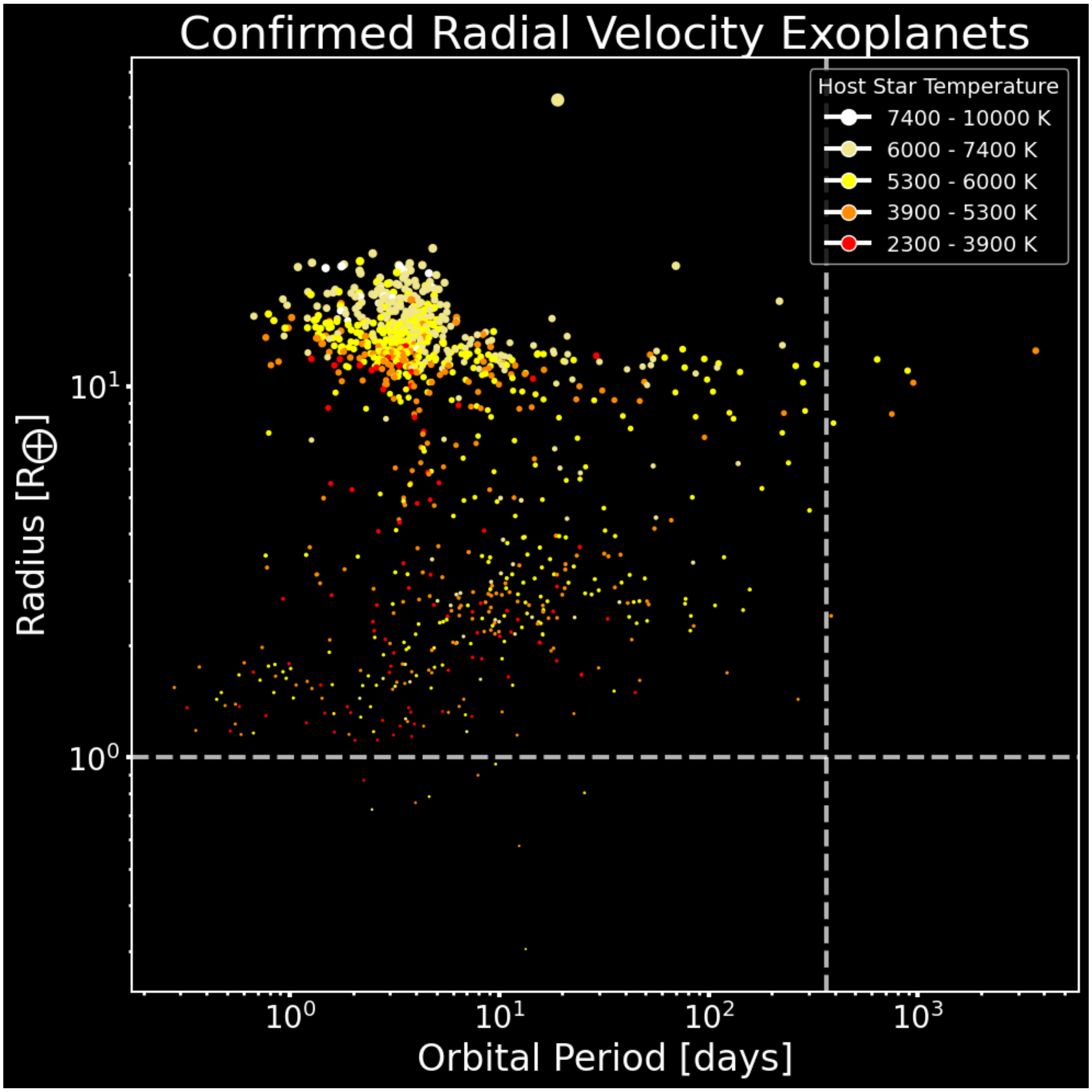

Figure 1.3: The plot above shows 1,010 exoplanets confirmed by the radial velocity detection method. The colors represent the temperature of the stellar host. Notice the Hot Jupiters clustering in the upper left. The dashed lines represent the Earth's radius and orbital period. Notice the paucity of exoplanets near the Earth's parameter space.

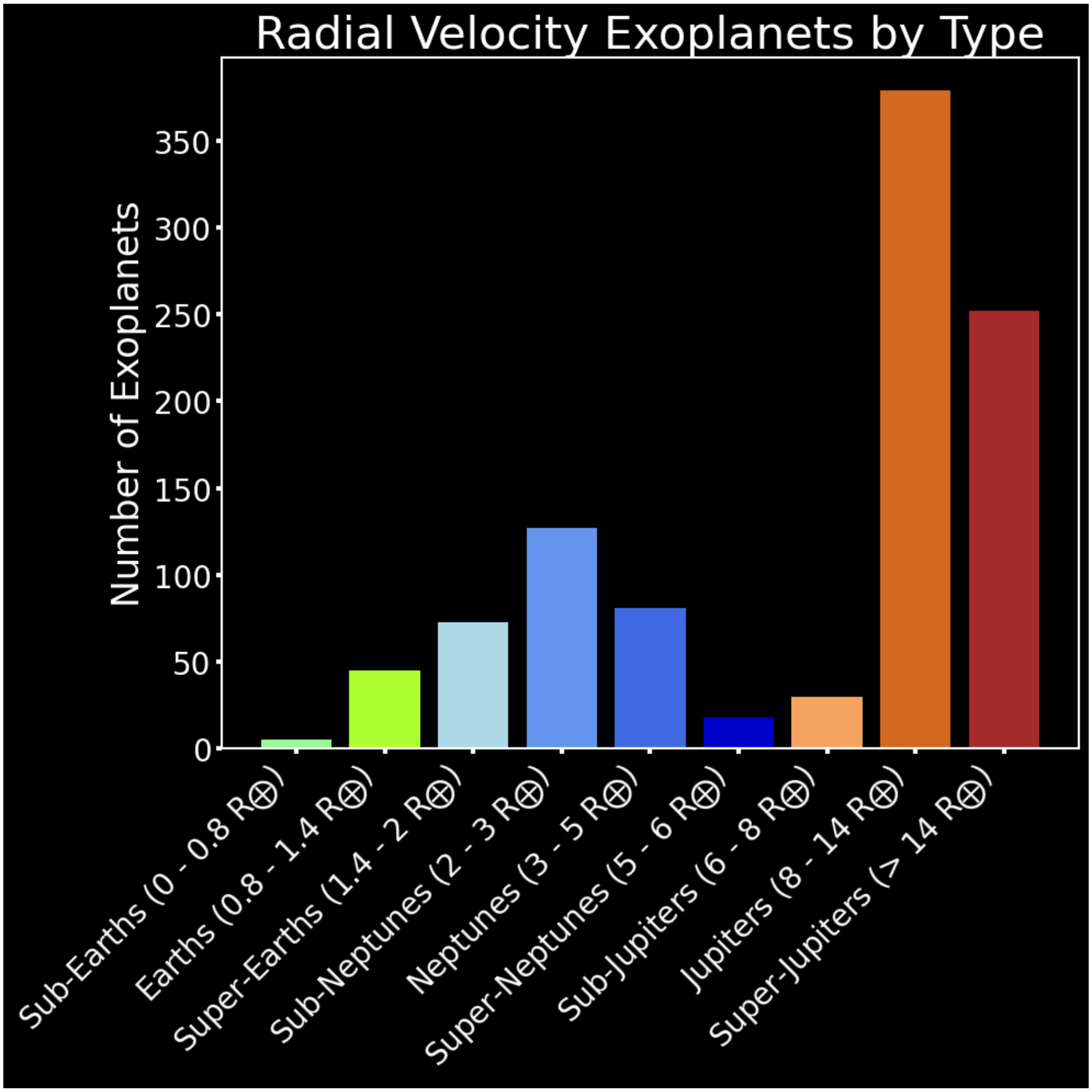

Figure 1.4: The histogram above shows 1,010 exoplanets confirmed by the radial velocity detection method. The planets are binned by radius. The majority of exoplanets confirmed by radial velocity are Hot Jupiters and Hot Super-Jupiters, and orbit their host star in less than 10 days.

1.1.2 Direct Imaging

The Habitable Worlds Observatory will directly image earthlike exoplanets around nearby stars, which is only possible by suppressing the star's light. For a solar system twin located 10 pc away, the host star will be 10^{10} times brighter than the Earth twin. A coronagraph suppresses the host star to achieve HCI and make the planet detectable [2] [3] [17]. Still, many sources of noise degrade this challenging detection, including leakage of starlight, speckles, shot noise, zodiacal dust, exozodiacal dust, detector dark current, and read noise. Careful design can limit the excess light from the coronagraph, and new detectors with low dark current and read noise can reduce detector noise. Minimizing noise is crucial for optimizing the exposure time needed for a credible biosignature detection, especially when spectroscopy divides light from an already faint source.

1.1.3 Biosignatures

The atmosphere of an exoplanet is one of the few observables that can be used to determine its composition, and thus habitability. Biological processes can release gases into the atmosphere that abiotic processes would otherwise deplete. A prime example is the production of oxygen by photosynthesis on Earth. Oxygen is a highly reactive gas that filters out of the atmosphere by oxidizing (rusting) other materials [18]. Photosynthesis has maintained Earth's current oxygen levels, making oxygen a marker of biological processes on Earth. A strong indicator of oxygen's presence in Earth's atmosphere is the deep O_2-A band absorption feature at 760 nm. Other biosignatures, including O_3, CH_4, H_2O, and CO_2, appear throughout the IR/O/UV regimes [19] [20] [21] [22] [23] [24] [25] [26]. Additionally, different forms of life produce different biosignature gases. For instance, Earth's early atmosphere did not have high levels of oxygen but instead had noticeable levels of methane from bacterial life. Although compelling habitable planet candidates with water vapor signatures exist, a Modern Earth analog with a significant O_2-A band remains elusive. A biosignature alone may not guarantee life on an exoplanet without other gases to rule out abiotic processes and false positives. Therefore, an IR/O/UV telescope capable of studying multiple biosignatures is required to discover Earth twins. HWO will search for biosignatures in the IR/O/UV range to rule out abiotic processes and false positives, with many studies developing methods to achieve this [21] [24] [25] [27] [28] [29].

1.2 Low Noise Detectors

Detectors that directly image earthlike exoplanets must have very low dark current and read noise. Suitable detectors include electron-multiplying charge-coupled devices (EMCCDs), skipper CCDs, microwave kinetic inductance detectors (MKIDs), and single photon counting CMOS (complementary metal-oxide semiconductor) sensors. EMCCDs have low read noise and dark current, and exist in large formats [30]. However, the EMCCD architecture clocks the signal charge across many pixels, making EMCCDs susceptible to defective pixels, radiation damage, and charge transfer efficiency degradation [31] [32] [33]. Skipper CCDs have been in development for about 30 years, and have recently shown promise in low noise and low dark current applications [34] [35]. Skipper CCDs also allow non-destructive readout but are not yet commercialized or available in large formats [36]. MKIDs offer high quantum efficiency, low dark current, and have recently shown radiation hardness [37]. However, they are not readily available in large formats and require sub-Kelvin operation provided by resource expensive readout and refrigeration systems [38] [39].

Single photon counting CMOS detectors have low read noise and low dark current [40]. These SPCDs use a physically small and low-capacitance floating diffusion sense node to achieve a high input referred conversion gain ($>$320 μV/e$^-$) [40]. The high gain resolves individual charge carriers, making the devices photon-number resolving. Unlike CCDs, which can propagate single-pixel failures across a pixel row during readout, CMOS detectors use direct readout circuits that isolate the effects of single-pixel failures (e.g., defective pixels, radiation damage, cosmic rays) to the affected pixel. CMOS SPCDs are radiation tolerant and have low power consumption [41][42]. Additionally, CMOS detectors are part of the multibillion-dollar cellphone camera industry, making them commercially available and leveraging third party research and development [43]. Furthermore, the dark current per pixel in CMOS SPCDs is comparable in magnitude to those of EMCCDs, encouraging the move towards CMOS devices in astronomy (see Table 1.2). Given the performance requirements for direct imaging and HCI applications for HWO, the CMOS SPCD is the detector candidate in this study. CMOS SPCDs offer low read noise, low dark current, radiation tolerance, and are commercially available in many formats.

The Strategic Astrophysics Technology (SAT) program Grant No. 80NSSC24K0372 supports our team in the Center for Detectors (CfD) at RIT in characterizing BAE Systems Imaging Solutions Inc.'s HWK4123 CMOS sensors (shown in Figure 1.5) and the Hamamatsu Photonics K.K. C15550-20UP ORCA Quest camera. The ORCA Quest camera uses HWK4123 sensors, and the quantum efficiency reported by [44] is plotted in Figure 1.6. Quantum efficiency defines how well a system can convert photons into electrons, where zero represents total photon loss.

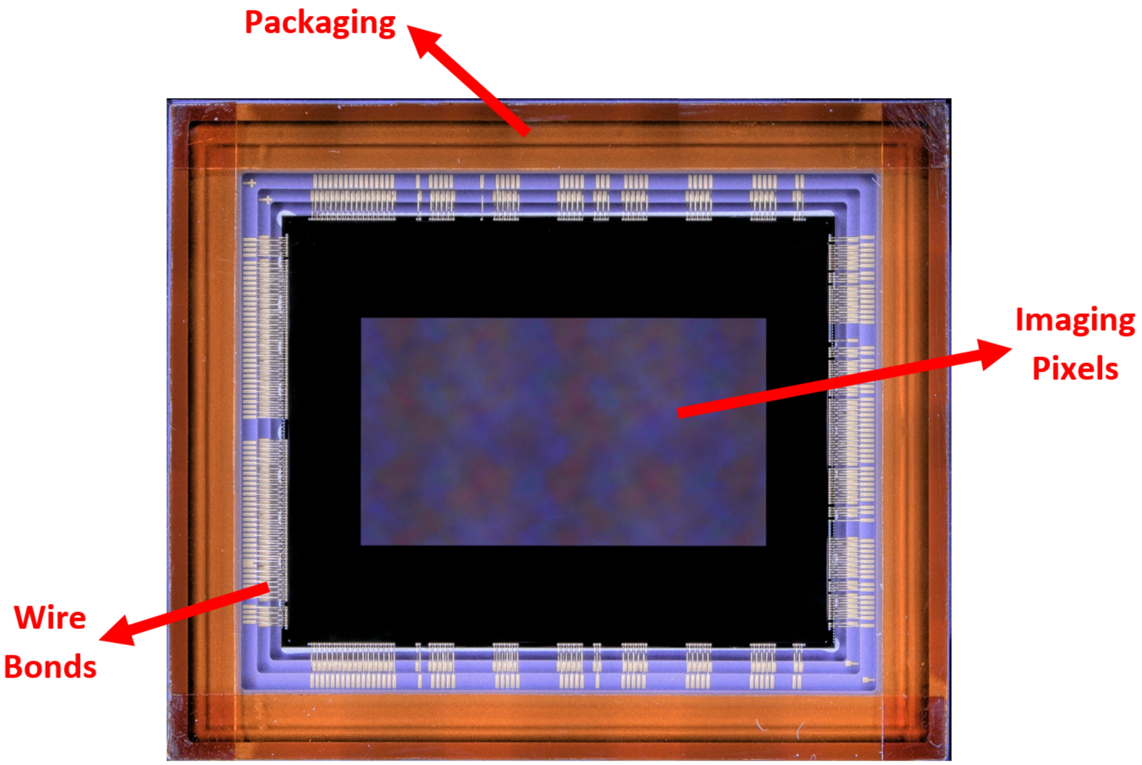

Figure 1.5: The image shows the BAE HWK4123 CMOS single photon counting detector. It measures 3.6 × 3.1 cm and has 9 Mpixels of size 4.6 μm.

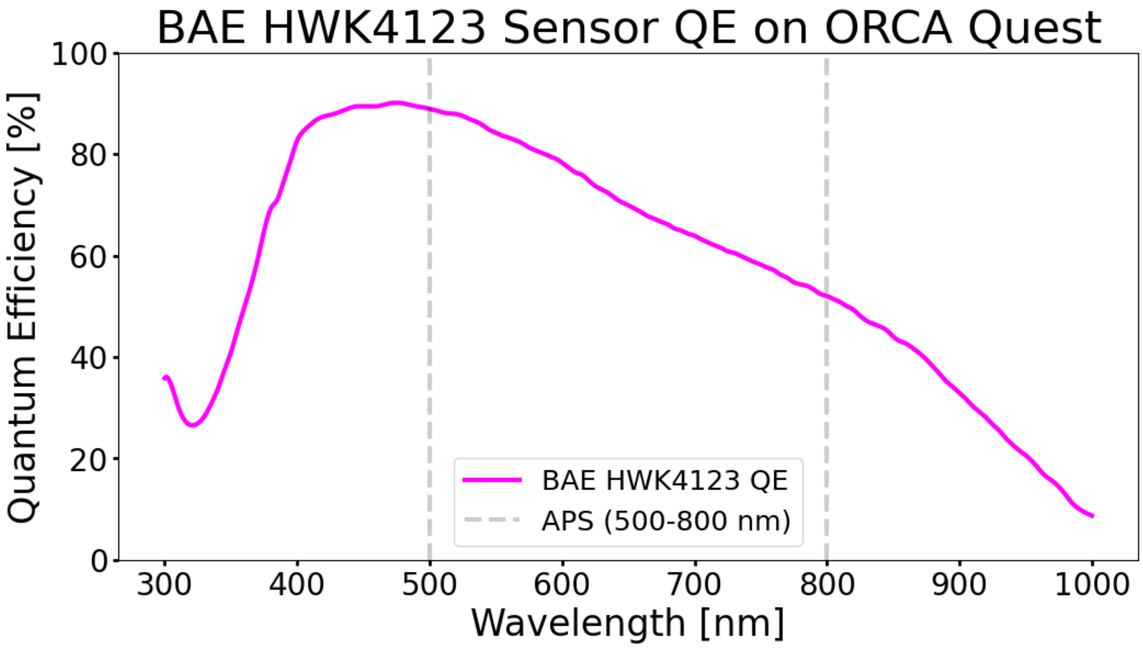

Figure 1.6: The curve shows the ORCA Quest camera QE. The QE of the detector is above 50% for the astrophotonic spectrograph's (APS) operating range (500 – 800 nm).

Table 1.2: State of the Art Detector Performance

Detector	CMOS SPCD [44]	EMCCD [45]	Skipper CCD [35]	MKID [46]
Model	BAE HWK4123	HNü 1024-1MP	SENSEI	ARCONS
Pixel Size [μm]	4.6	13	15	222
Dark Curr. [e$^-$/s/pix]	$1.63 \times 10^{-5\,a}$	$7.0 \times 10^{-5\,b}$	$\sim 3.8 \times 10^{-4\,c}$	$\sim 0\,^d$
Read Noise [e$^-$/pix]	0.27	0.1	~ 0.14	$\sim 0\,^d$

[a] interpolated value from [47], see Section 2.2.3, at 183 K.

[b] reported value from [45] for the ALPHA model, at 183 K.

[c] calculated from Figure 10 in [35], at 185 K.

[d] ARCONS reported with no dark current (at 110 mK) and no read noise by [46] and [48].

1.3 Astrophotonic Spectrograph

Astrophotonics is an emerging field that applies photonic technologies to astrophysical instrumentation. Broadly defined, photonics is the study of light and using light in technology. Historically, notable contributors are Mozi (China, camera obscura), Ibn al-Haytham (Iraq, highly cited by modern counterparts such as Newton, Huygens, Kepler, and Galileo), and Euclid (Greece, geometrical optics). In the modern era, the term "photonics" which emerged in the 1960-70s emphasizes technological applications, such as optical fibers in telecommunications. Photonic technologies are being developed and used in astrophysical applications, such as adaptive optics for ground-based telescopes [49] [50] [51] [52] [53]. Another photonic technology is the astrophotonic spectrograph (APS), which leverages arrayed waveguide gratings to produce a discrete spectrum. The APS shows great potential for integration in astronomical instruments, with most advancements being in the NIR domain and recent efforts targeting the optical range [54] [55] [56] [57] [58] [59] [60].

This section describes the basic design of an APS. An optical APS design is shown in Figure 1.7, and the APS components described above are identified in Figure 2.3. A detailed description of general APS geometry is provided in the foundational paper by [61]. Light enters an optical single-mode fiber (SMF), which strictly allows the fundamental mode of the light to propagate to prevent excitation of higher modes, mode conversion, and thus degradation of the signal [61]. The SMF guides the light to the free propagation region (FPR). This region allows the light the spread until it reaches the arrayed waveguides (AWG) which are made of SMFs. Each waveguide is $m\lambda$ longer than its preceding neighbor, where m is the spectral order of diffraction. That is, the length difference is $\Delta L = m \cdot \frac{\lambda_c}{N_g}$, where m is the spectral order, λ_c is the central wavelength, and N_g is the effective index of the waveguide [61]. This path difference allows for constructive interference of the light. The light then travels through a second FPR. The focusing of light in the second FPR follows a circular image plane, which is typical of Rowland-type mountings (see Figure 1b of [61], Figure 10 of [62], and Figure 1.7). The output fibers are then placed at the focal points on the Rowland circle for each wavelength channel to provide the output spectrum [63].

The discretized APS output differs from a traditional spectrograph, which produces a continuous spectrum. Object location information is lost when using an APS, meaning the spectrum's position on the detector's surface does not correlate with the object location in the telescope optics image plane. Instead, the input fiber is positioned at the object's image location and the output spectrum is imaged on the detector. The APS is extremely compact, measuring just a few centimeters, and can be stacked for multi-object spectroscopy [64].

Key spectrograph performance metrics for APS include resolving power, free spectral range, crosstalk, and throughput. Resolving power is defined as the central wavelength of the channel divided by the channel spacing (bandwidth), expressed as $R = \lambda/\Delta\lambda$. The channel bandwidth is the wavelength difference between adjacent Gaussian peaks of the discretized transmission response from the AWG.

The spectral orders from the AWG follow the cyclical output of conventional diffraction gratings. In conventional gratings, higher order modes repeat at a distance $m\lambda$ away from the fundamental mode. In an AWG, the free spectral range (FSR) determines how far, in wavelength space, the higher order modes will appear from the fundamental mode. Properly selecting the FSR avoids cross dispersion of higher modes into neighboring channels. An output channel with a Gaussian distribution centered at λ will have higher order peaks at $\lambda \pm$ FSR, $\lambda \pm 2$ FSR, and so on. Therefore, the FSR must be at least as large as the wavelength range that the APS will cover. This ensures that the first higher order of the lowest wavelength channel falls beyond the fundamental mode location of the highest wavelength channel, and so forth for all channels.

Channel crosstalk, broadly defined, is the contamination of a given spectral channel by other channels. Several mechanisms contribute to crosstalk, such as receiver crosstalk (coupling of light distribution), aperture truncation (finite width of array modulates power), mode conversion (excitation of first-order mode at junctions), coupling in the array (at input and output from phase distortion), phase transfer incoherence (due to imperfections), and background radiation (light scattered within arrays) [61] [62] [65].

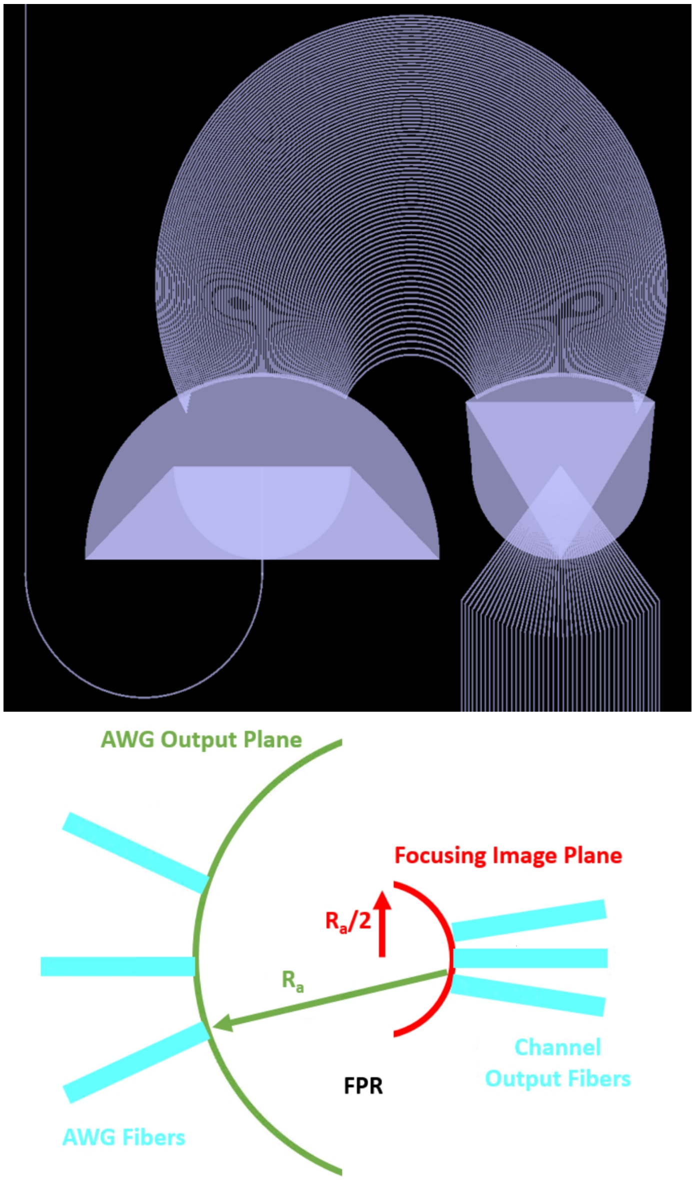

Figure 1.7: (top) The image provided by Pradip Gatkine shows a model for the optical astrophotonic spectrograph. It has a 300 nm free spectral range spanning 500 – 800 nm. The APS has 46 output waveguides, each with a diameter of 6 μm and a core-to-core spacing of 100 μm. Each channel has a spectral bandwidth of ∼6.5 nm. The input fiber is located at the bottom right, above which is the first propagation region. The arrayed waveguides are the multiple curved fibers in the center of the image. The second propagation region is the Rowland circle in the bottom left, from which the output waveguides produce the spectrum. (bottom) The diagram shows a simplified version of Figure 1b of [61] and Figure 10 of [62] for the Rowland-mount type geometry. The AWG fibers are in a circle of radius R_a, and the focal plane for the constructive interference pattern follows a circle of radius $R_a/2$. The output channel fibers are located where the constructive interference of the channel occurs.

1.4 Telescopes and Coronagraphs

LUVOIR and HabEx are telescope designs with a shared goal of finding habitable exoplanets. Concepts and ideas from both may be incorporated into HWO, a 6 m class telescope recommended to NASA by the 2020 Decadal Survey [1]. The HWO design is an active area of collaboration, with ongoing efforts actualizing the mission concept. HabEx is a 4 m class telescope with an external starshade working in tandem with an internal coronagraph. The HabEx coronagraph is required to provide a contrast of order 10^{-10}. LUVOIR offers two designs: a 15 m class telescope (LUVOIR-A) and an 8 m class telescope (LUVOIR-B), both with coronagraphs (ECLIPS-A and -B) designed to reach the contrast ratio of 10^{-10} necessary for detecting habitable exoplanets [3]. To avoid confusion later in the text, I define "higher" contrast ratios for cases in which the exoplanet and star contrast is closer to 1, so the star outshines the planet less. Correspondingly, I define "lower" contrast ratios for cases in which the exoplanet and star contrast is closer to 0, so the star outshines the planet more.

Coronagraphs have an inner working angle (IWA) determined by the central portion of the image being suppressed, and an outer working angle (OWA) set by the optics of the system. For LUVOIR-B, the IWA is designed as $IWA = \frac{7}{2} \cdot \frac{\lambda}{D}$, and the OWA is as $OWA = 64 \cdot \frac{\lambda}{D}$, where λ is the observed wavelength and D is the telescope diameter. These angles are expressed in radians, which can be converted to arcseconds. The IWA, OWA, and distance to the stellar system restrict the observable region of the system when using a coronagraph. For example, the IWA for a LUVOIR-type mission would exclude the inner 0.5 au of a solar system twin, rendering a planet like Mercury undetectable [15].

1.5 Stellar Spectral Types

The Morgan-Keenan spectral classification system sorts stars based on their luminosity and surface temperature. Stars of the same spectral type have similar luminosity, mass, and radius. The luminosity determines the photon flux received by a planet at a specific distance from its host star, and thus the location and size of the habitable zone (HZ). The main sequence lifetime depends on stellar mass and luminosity, and affects the amount of time for which a stellar system maintains a stable HZ. The apparent size of the HZ also affects the detectability of habitable planets due to constraints from the coronagraph's inner and outer working angles.

1.5.1 Stellar Lifetime

The stellar main sequence lifetime depends on the star's mass and luminosity, and thus spectral type. This lifetime influences the duration for which a stellar system provides stable conditions for life to develop. To first order, the main sequence lifetime of a star is:

$$\tau = \frac{\eta \cdot M_\star \cdot c^2}{L_\star} \cdot \frac{1}{3.154 \times 10^7} \quad [years] \tag{1.5.1}$$

where η is the efficiency of fusion, adopting a value of 0.0007 from the Sun, and 3.154×10^7 converts from seconds to years. Main sequence lifetimes are plotted in Figure 1.8.

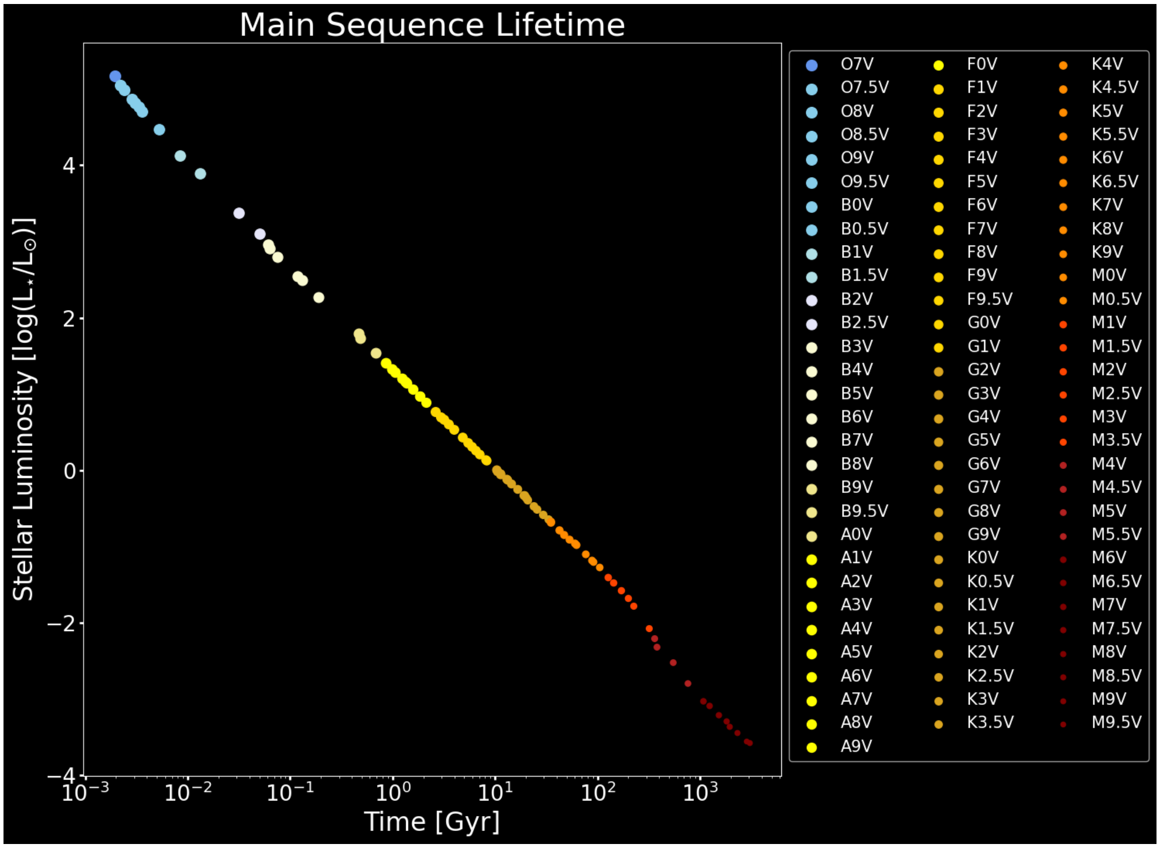

Figure 1.8: The plot above shows the main sequence lifetime of stars using Equation 1.5.1.

A typical O star runs out of fuel and explodes after about 10 million years. Luminous, short-lived stars cannot provide stable conditions for enough time to allow life to develop. In fact, the Earth took 10 to 500 million years to cool down from its formation before liquid water could remain on its surface. Before cooling, life on the planet would be virtually impossible. The cooling time is debated after the discovery of 4.4 billion-year-old zircon crystals which support faster cooling [66]. For this paper, I restrict the upper luminosity of stars to F0V stars, which last roughly 2 billion years on the main sequence — enough time to allow the Earth's Great Oxygenation Event to occur [18].

1.5.2 Habitable Zone

The habitable zone around a star is broadly defined as the distance from the star at which a planet may maintain liquid water. The 2020 Decadal Survey [1] and 2023 Exoplanet Science Gap [13] adopt the conservative HZ of 0.95 – 1.67 astronomical units (au) first discussed in [10]. Using this definition for the solar system's HZ, the equations to express the HZ inner edge (r_{inner}), outer edge (r_{outer}), and the location at which a planet receives the same photon flux as the Earth ($r_{HZ} = r_{\oplus}$) are:

$$r_{inner} = 0.95 \cdot \sqrt{\left(\frac{L_\star}{L_\odot}\right)} = 0.95 \cdot \left(\frac{R_\star}{R_\odot} \cdot \left(\frac{T_\star}{T_\odot}\right)^2\right) \quad [au] \tag{1.5.2}$$

$$r_{HZ} = r_{\oplus} = 1.00 \cdot \sqrt{\left(\frac{L_\star}{L_\odot}\right)} = 1.00 \cdot \left(\frac{R_\star}{R_\odot} \cdot \left(\frac{T_\star}{T_\odot}\right)^2\right) \quad [au] \tag{1.5.3}$$

$$r_{outer} = 1.67 \cdot \sqrt{\left(\frac{L_\star}{L_\odot}\right)} = 1.67 \cdot \left(\frac{R_\star}{R_\odot} \cdot \left(\frac{T_\star}{T_\odot}\right)^2\right) \quad [au] \tag{1.5.4}$$

where "$_\star$" indicates parameters for the star, and "$_\odot$" indicates solar values.

The stellar type affects the location and size of the habitable zone, as shown in Figure 1.9. Since r$_{HZ}$ defines the location at which a planet receives the same photon flux as Earth, the amount of light reflected by the planet should be roughly the same (ignoring stellar temperature-dependent spectral features), regardless of stellar spectral type (see Figure 2.10).

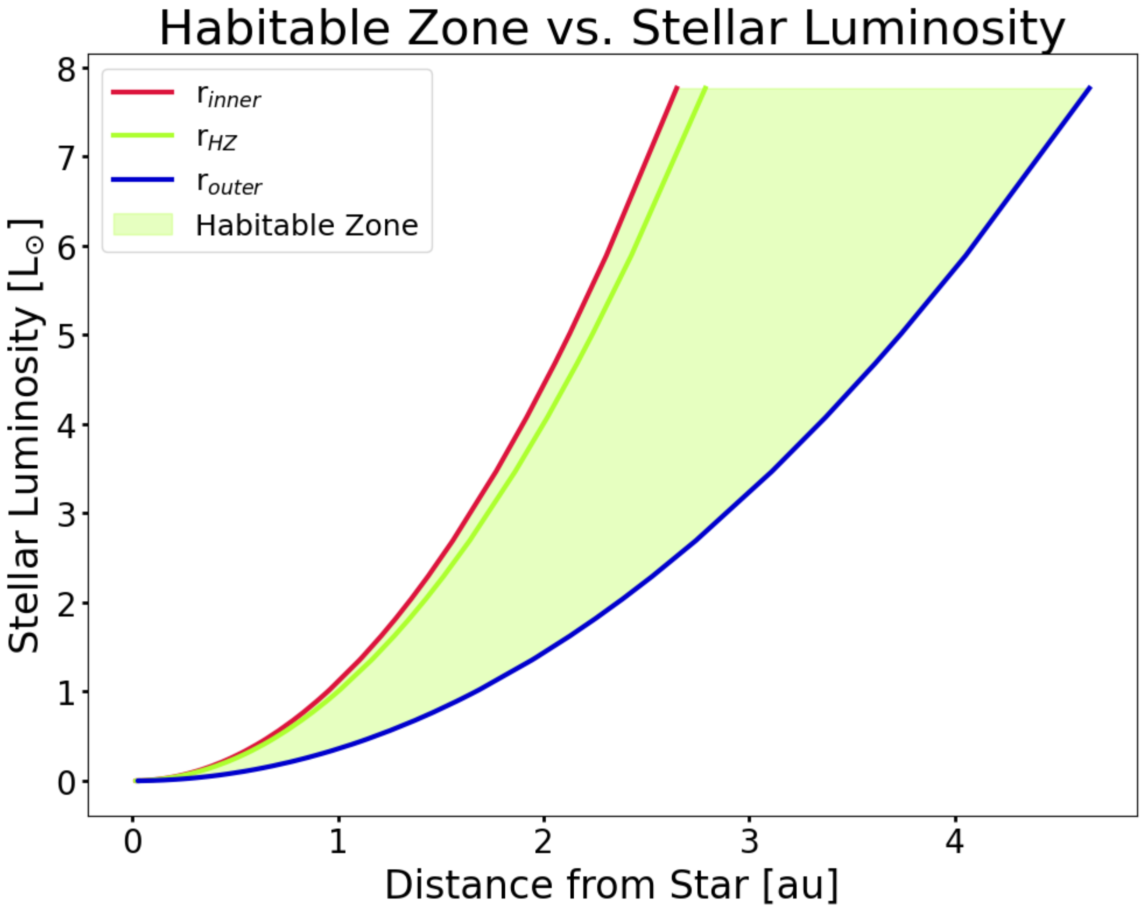

Figure 1.9: The plot above shows the habitable zone for stars from spectral type F0V to M9.5V. The more luminous the star is, the farther away and larger the HZ becomes.

However, the contrast ratio between the star and the planet will differ, with more luminous stars outshining the planet to a greater extent. That is, the light scattered by a coronagraph for a more luminous star has higher amplitude (e.g. Airy disk), thus outshining the planet more. This effect is shown in Figure 2.5. Additionally, the apparent angular size of the HZ based on spectral type has implications for observations, as discussed below.

1.5.3 Inner and Outer Working Angles

The more luminous a star is, the farther away and larger the habitable zone is, as shown in Figure 1.9. Consequently, lower luminosity M, K, G dwarfs will have smaller and closer HZs than their more luminous O, B, A counterparts. The location of the HZ spans a distance from the star, which translates into an angle in the sky. The angle α is defined by the distance to the stellar system, d, and the location of the HZ relative to the star, r_{HZ}, as shown in the following equation:

$$\alpha = 206265 \cdot \arctan\left(\frac{r_{HZ}}{d}\right) \quad [arcseconds] \tag{1.5.5}$$

where the units for r_{HZ} and d must match, and the prefactor converts the angle from radians to arcseconds (as). The results of Equation 1.5.5 are in Figure 1.10 .

The apparent angular size of the habitable zone constrains the spectral type of star that can be observed. The HZ may fall within the IWA for faint stars, or beyond the OWA for bright stars. For a distance of 10 pc, the outer edge of the HZ for K5V dwarfs appears at the IWA of LUVOIR-B at 760 nm (0.068 as). Conversely, the inner edge of the HZ of a B8V star coming into view from the OWA of LUVOIR-B at 760 nm (1.25 as). For this paper, the lower brightness limit is set to K5V stars due to the IWA, and the brightest stars considered are F0V stars due to main sequence lifetime constraints.

1.6 Structure and Context of Research

This project focuses on the simulation of a new instrument, the SPCPS, for the application of direct imaging of terrestrial exoplanets. The SPCPS incorporates new and compact technologies: the CMOS single photon counting detector (SCPD) and the astrophotonic spectrograph (APS). This work demonstrates the versatility of astrophotonics in providing new instruments for astrophysical applications. The CMOS SPCD has very low dark current and read noise, which are required to directly image earthlike exoplanets which emit only a few photons per hour per spectral bin (see Figure 2.11). The APS provides the spectrum of the exoplanet, which helps identify the presence or absence of biosignatures.

To understand the requirements for the instrument design, the science target is simulated to establish observational constraints. The Methods section outlines the selected technology parameters: APS in Section 2.1, CMOS SPCD in Section 2.2, telescope in Section 2.4. A brief

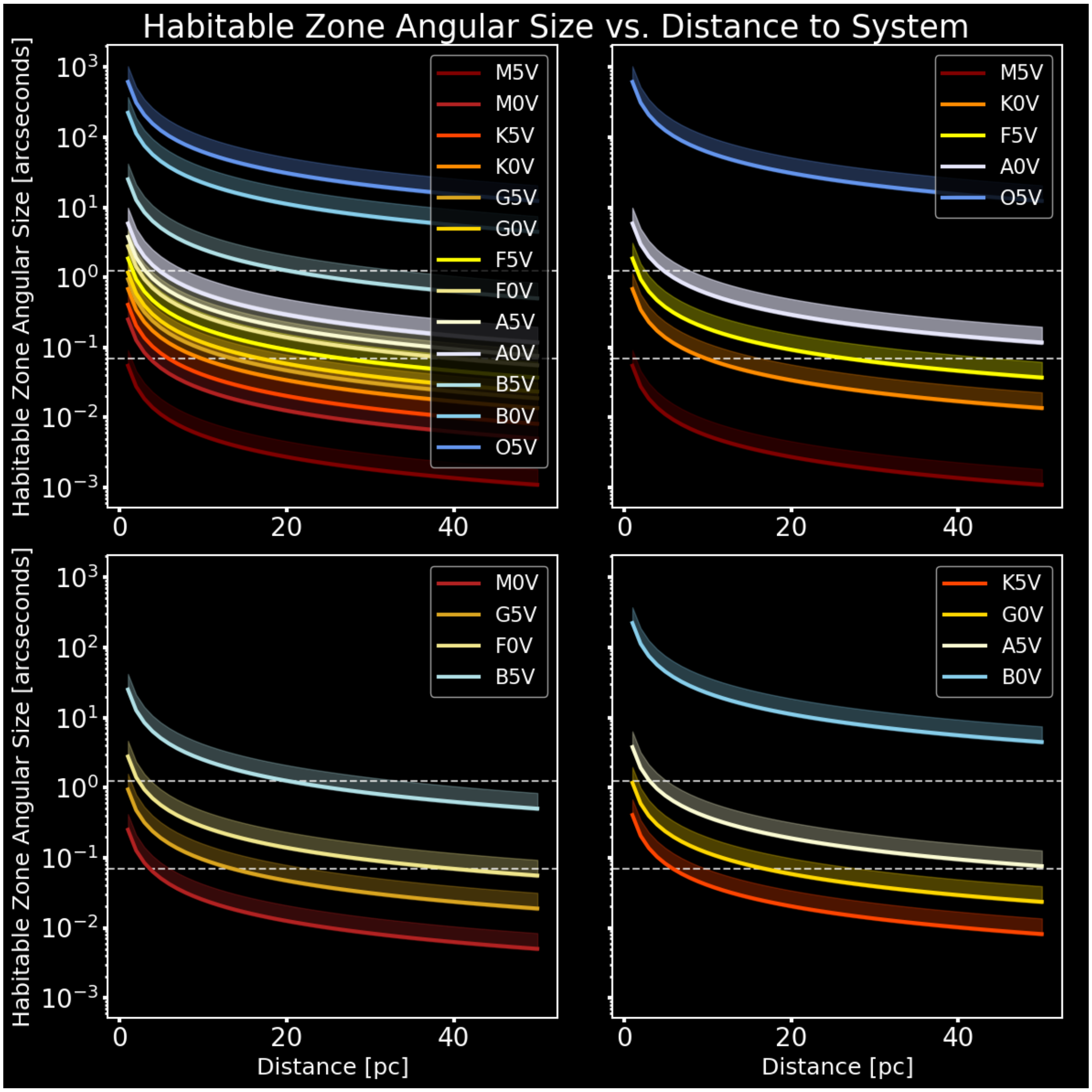

Figure 1.10: Shown above are the angular sizes of the habitable zone as a function of distance depending on the spectral type of the star. The lower horizontal dashed line is the IWA and the upper dashed line is the OWA, for LUVOIR-B at 760 nm. Notice that, for M5V stars, the HZ falls within the IWA below 1 pc and is suppressed by the coronagraph. The solid color curves represent the location at which a planet would receive the same flux as the Earth does around the Sun. The shading represents the inner and outer edges of the HZ.

description of the instrument layout is provided in Section 2.3, with a more detailed view in Section 2.6. The simulation of the stellar system and exoplanet is covered in Section 2.5.

The open-source software exoVista generates the spectrum of the star, exoplanet, and an exozodiacal dust map for the simulated stellar system. Section 2.5 describes how exoVista produces these parameters, and how they are used to derive a signal-to-noise ratio (SNR) which drives system requirements on the instrument. The SNR for an observed biosignature can be derived using the equivalent width of the line (see Equation 2.5.6), and then compared to the SNR that uses astronomical sources and instrument characteristics (see Equation 3.1.1).

The Results section describes the integration times required to reach a desired SNR for the direct observation of the O_2-A band. The Discussion section explores the current instrument design and future improvements. The Conclusion section summarizes the findings and discoveries of this work.

Chapter 2

Methods

This section describes the technologies used for the single photon counting photonic spectrograph, the telescope specifications, and the models for the astronomical sources. The astrophotonic spectrograph is described in Section 2.1, the CMOS single photon counting detector in Section 2.2, the basic SPCPS design in Section 2.3, the model telescope in Section 2.4, the astronomical sources in Section 2.5, and the parameters for the SPCPS model with observation requirement flow down in Section 2.6.

2.1 Visible Band Astrophotonic Spectrograph

The astrophotonic spectrograph in this project being developed by Pradip Gatkine and his group, who have extensive expertise in designing and characterizing this technology [50] [63] [67] [68] [69] [70] [71]. The materials selected for the APS are SiN and doped-SiO_2, which are promising for low loss of light in the optical regime [56][72] and will inform a comparative performance study. The spectrograph is required to have an FSR of 300 nm such that the APS can cover the optical range from 500 - 800 nm without higher spectral order overlap from other channels. The APS will have 46 output waveguides with a physical diameter of 6 μm. The output channels have an equal bandwidth of $\Delta\lambda$~6.5 nm. The resolution $R=\lambda/\Delta\lambda$ is given by the central wavelength λ of the channel and the bandwidth $\Delta\lambda$. For instance, a channel centered at 763 nm will have R~120. This resolution is close to that required for an

O_2-A band detection, owing to the feature's full-width at half-maximum of ∼5 nm and central wavelength of 760 nm yielding R∼140 [20]. The channel cores are spaced 100 μm apart on the chip to minimize channel output coupling. The expected channel crosstalk will be less than or about 1% by design, and is thus omitted as a source of noise from this study. The estimated channel throughput is 30% for all channels, based on projections from a NIR astrophotonic spectrograph using SiN [56]. The APS under development should perform similarly to the NIR APS. The APS parameters for this study are listed in Table 2.1.

Table 2.1: Astrophotonic Spectrograph Parameters

Parameter	Value	Notes
Format	46 channels	-
Channel Bandwidth	6.5 nm	uniform
Operating Range	500 - 800 nm	-
Free Spectral Range	300 nm	-
Waveguide Diameter	6 μm	-
Channel Core-to-Core Spacing	100 μm	-
Channel Crosstalk	<1%	-
Throughput*	30%	all channels

* estimate based on [56]

2.2 CMOS BAE HWK4123 Single Photon Counting Detector

The devices selected for this study are the BAE HWK4123 CMOS SPCD and the Hamamatsu Photonics K.K. C15550-20UP ORCA Quest camera. The ORCA Quest camera uses BAE HWK4123 sensors. Their characterization is part of a NASA-funded effort in the CfD (SAT Grant No. 80NSSC24K0372). The HWK4123 sensor is shown in Figure 1.5 and the ORCA Quest quantum efficiency [44] is depicted in Figure 1.6. Both technologies are in the early stages of characterization by the CfD, which has thus far measured read noise and dark current at 253 K. These preliminary measurements provide order of magnitude information, but are not yet reliable. As such, the simulations in this work rely on published and estimated values for the dark current and read noise as listed in Table 2.2. Future work on this project will use the HWK4123 sensor characterization by the CfD once the devices are better understood.

2.2.1 Relevant Parameters

To simulate the SPCPS instrument performance for exoplanet observations, detector noise must be included in SNR calculations. The primary sources of detector noise are dark current and read noise. Dark current competes with the low photon flux from the exoplanet, while read noise accumulates with the number of frames used to create a stacked image to improve SNR. Other sources of detector noise exist, such as clock induced charge (CIC), but are assumed to be negligible and thus omitted from this preliminary study.

Dark current is the amount of charge accumulated in a detector pixel in the absence of photons. It is measured in electrons per second per pixel (e^-/s/pixel). The dark current count rate is the product of the number of pixels n_{pix} on which the APS channel is imaged and the average dark current i_{dark}:

$$DC = i_{dark}(T) \cdot n_{pix} \quad [e^-/s] \tag{2.2.1}$$

The dark current depends on the detector temperature, and decreases for lower temperatures.

Read noise, broadly defined, is the uncertainty of the measured voltage (and thus charge) on the pixel. The total read noise is the product of the number of pixels n_{pix}, the number of reads n_{reads}, and the read noise per pixel “rn”:

$$RN = rn \cdot n_{reads} \cdot \sqrt{n_{pix}} \quad [e^-] \tag{2.2.2}$$

These equations will be used later to calculate the achievable SNR (SNR_{achi}) by the system (Equation 3.1.1). This study does not consider the limiting effect of cosmic rays on the maximum integration time per frame, but it will be addressed in future model improvements. Cosmic ray hits restrict the readout time for a sensor, as their effects (secondary photons) accrue in the detector pixel storage well. The maximum integration time per frame determines the number of frames needed to satisfy the total observation time required to reach a desired SNR. The number of frames required defines the value of n_{reads}. Thus, the parameter space of cosmic ray hits and the storage well of the detector as competing limiting factors in the maximum integration time per frame is unexplored in this paper.

Currently, the maximum integration time per frame is obtained by finding the integration time for which an observation would fill the detector's pixel to half of the storage well depth of the pixel. The contributing photon sources are the detector dark current and the astronomical sources described in Section 2.5. The storage well of a pixel can hold a certain number of electrons before the pixel becomes saturated. To avoid the non-linear response regime of CMOS devices as the pixels approach saturation, the upper limit for the storage well is set to half full.

2.2.2 Preliminary Measurements

The CfD is currently integrating the ORCA Quest camera with the Rochester Imaging Detector Laboratory (RIDL) systems to characterize relevant metrics, such as dark current and read noise.

Dark current measurements require an environment devoid of photons. Initial attempts to couple the ORCA Quest camera to a dark integrating sphere at RIDL were unsuccessful due to unresolved light leaks. The darkest environment achieved for the Quest involved placing aluminum tape on the lens cap in a dark room. Dark current can then be measured by fitting the slope of integrated charge over time. However, the ORCA Quest is a commercial camera that attempts to automatically subtract dark current from its images. For such cases, dark current is calculated from the slope of increasing variance in the signal against integration time [73].

The dark current integration region is defined as the central 128×128 pixels of the camera in our experiment. This region is chosen to avoid vignetting on the detector surface caused by the C-mount lens on the ORCA Quest camera. For each integration time, 10,000 frames are collected to measure the variance per pixel. The variances are averaged to represent each integration time. The measured values are shown in Figure 2.1. The dark current slope of the Quest is measured to be 0.045 e^-/s/pixel at 253 K, nearly 3 times the 0.016 e^-/s/pixel reported by [74]. Due to this discrepancy and the lack of measured values at lower temperatures, dark current values are modeled according to the treatment in Section 2.2.3.

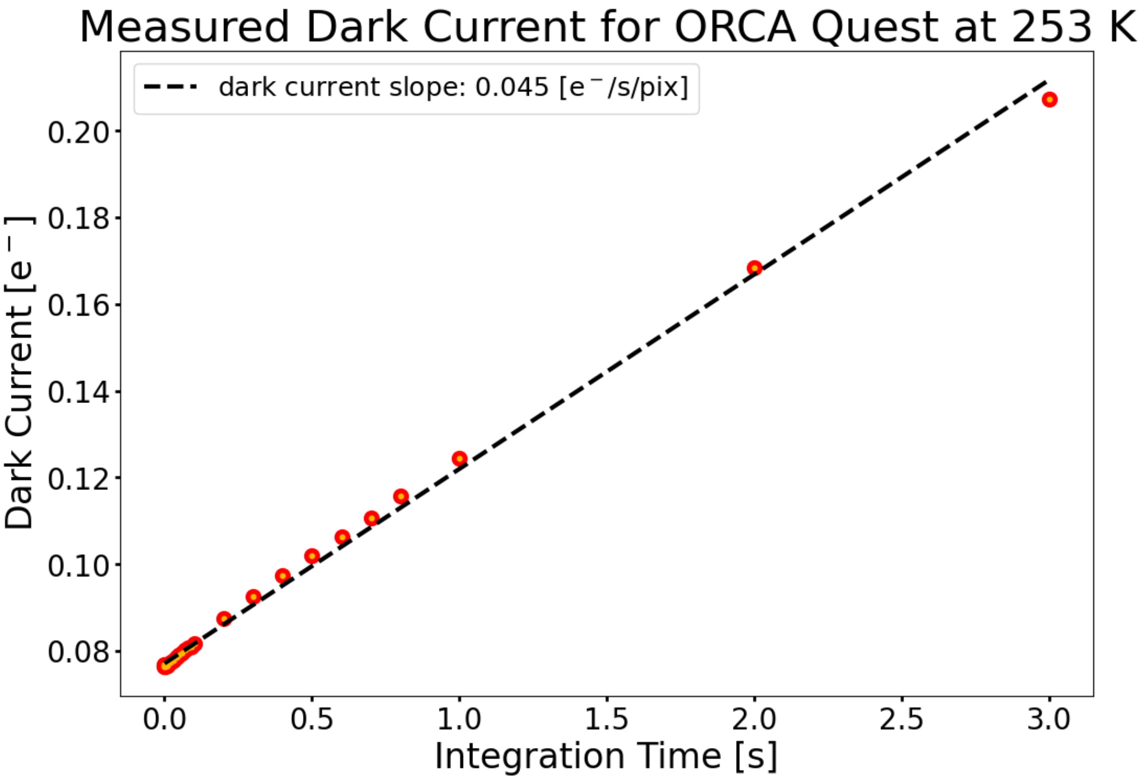

Figure 2.1: Plotted above are the measured dark current values for different integration times.

Read noise can be measured by using the shortest integration time and averaging the signal accrued per pixel. The short integration time prevents dark current from contributing significantly to the signal, leaving "only" the read noise. The shortest integration time achievable by the ORCA Quest camera is 172 μs. Using this integration time, 10,000 frames were taken for the entire 4096 × 2304 pixel array and averaged to provide a read noise measurement per pixel. Note that these measurements may include readout electronics noise, 1/f noise, random telegraph noise, and reset kTC noise. Since the sensor on ORCA Quest cannot be isolated, it is impossible to constrain the other sources of noise. Therefore, the measurements described above are treated as the read noise. The measured values are shown in Figure 2.2. The read noise distribution shows a hot tail, which has been reported for other CMOS SPCDs [42]. The mean read noise is 0.27 e^- which agrees with the mean 0.24 e^- reported by Hamamatsu [74].

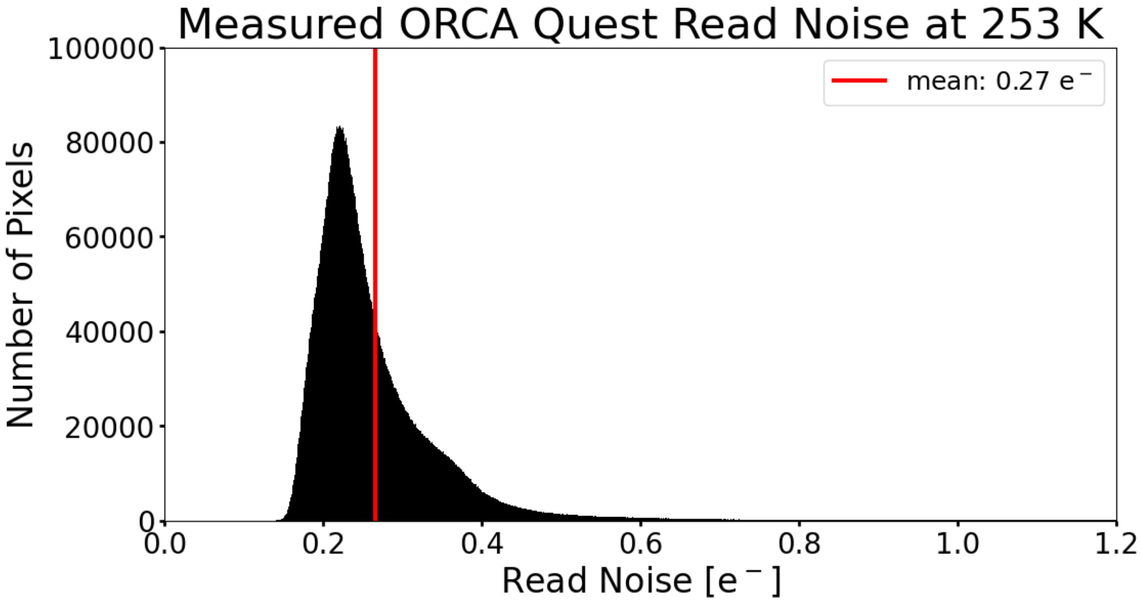

Figure 2.2: Plotted above is the measured read noise for ORCA Quest. The mean value is in agreement with Hamamatsu's reported value.

2.2.3 Estimated Values

Presented below are two methods to model dark current based on published values. The first method uses the doubling temperature, the second method scales interpolated and extrapolated values from previous measurements made by the CfD for another SPCD, the Quantum Image Sensor (QIS) [42]. The dark current values listed in Table 2.2 are evaluated for the telescope specification temperatures listed in Table 2.3.

The doubling temperature calculation requires one set of corresponding temperature and dark current values, and the temperature change for which the dark current doubles. The values used to set up the doubling temperature estimate are the reported dark current of 2 e^-/s/pix at 303 K by [47] and a doubling temperature of 8 K measured for the QIS [42]. Reported values for the HWK4123 dark current at 253 K and 237 K are 0.016 e^-/s/pix and 0.006 e^-/s/pix respectively [74], obtained for the ORCA Quest camera which uses BAE HWK4123 sensors. These values align with the doubling temperature estimates, which are 0.026 e^-/s/pix and 0.007 e^-/s/pix at 253 K and 237 K respectively. No measurements below those temperatures have been reported for this sensor.

However, the QIS characterization reports values down to 180 K. The QIS is a silicon device that appears to have a dark current floor below ~ 250 K [42]. In fact, the dark current floor for silicon devices is the subject of investigation by other groups, such as for UV EMCCD devices[1]. This suggests that the doubling temperature method may not be valid at lower temperatures for silicon devices (and thus the HWK4123 sensors).

The scaling method uses measured dark current values from the QIS detector and adjusts them based on the area of the pixels. The pre-radiation values provided in Figure 12 of [42] appear to show two coarse linear regimes above and below 250 K. The slope above 250 K is about 2.5×10^{-4} e^-/s/pix/K, and about 2.5×10^{-6} e^-/s/pix/K below 250 K. Using these two regimes, the dark current values can be interpolated and extrapolated for the QIS. Then, multiplying the estimated values by the areal ratio of the pixels scales the results, assuming a similar pixel thickness. The QIS has 1.1 μm pixels, whereas HWK4123 has 4.6 μm pixels. This method accounts for the apparent dark current floor for CMOS devices. The rest of the paper uses the values from the dark current floor and scaling method (column [b] in Table 2.2).

Table 2.2: Single Photon Counting Detector Parameters

Parameter	CMOS BAE HWK4123		Notes
Format	4096 × 2304 pixels		-
Pixel Size	4.6 μm		-
Read Noise	0.23 e^-/pix		median
Storage Well Depth	7,000 e^-		
Dark Current [a,b] [e^-/s/pix]	*3.4×10^{-9}* [a]	0.00092 [b]	70 K
	4.5×10^{-6} [a]	0.0046 [b]	153 K
	2.0×10^{-5} [a]	0.0053 [b]	170 K
	0.11 [a]	0.072 [b]	270 K
Quantum Efficiency	87%	500 nm	Figure 1.6
	61%	760 nm	
	56%	800 nm	

[a] values estimated from [47].
[b] values estimated from [42].

---

[1] `https://spie.org/astronomical-telescopes-instrumentation/presentation/Advancing-Ultraviolet-Detector-Technology-for-future-missions--Investigating-the/13093-26`

We note that dark current is one of the highest contributors of noise in the exoplanet direct imaging application. The required integration time for a desired SNR is highly sensitive to dark current. The values used in this paper are estimates that will be updated upon completion of the HWK4123 characterization. At the moment, it is unclear whether the dark current floor at lower temperatures exists for all devices, and the one selected here. This will be determined by the sensor characterization in the CfD, as well as research from other groups. If the HWK4123 can be modeled with doubling temperature at lower temperatures, then the integration times will decrease. The dark current floor method provides a conservative upper value for the HWK4123 sensor dark current and is used out of caution.

2.3 Overview of the SPCPS Instrument Design

The preliminary design for the single photon counting photonic spectrograph (SPCPS) is simple and compact. The instrument excludes telescope components upstream of the astrophotonic chip (i.e. mirrors, Lyot stops, coronagraphs, etc), as well as refrigeration and data acquisition systems. Instead, SNR calculations account for the upstream components with terms such as the telescope throughput.

The instrument design is constrained by the SNR requirements. The SPCPS presented here assumes that light from the target object (exoplanet) enters the APS from a single-mode input fiber. The APS produces the discretized 46-channel spectrum through the output fibers. The light then propagates in free space and reaches a collimating lens, followed by a camera lens. The detector sits at the focal plane behind the camera lens and captures the spectrum. A simple schematic illustrates this setup in Figure 2.3. Paraxial (perfect) lenses neglect wavelength-dependent effects of light propagation and are used here for simplicity. Future work will involve inserting real lenses into the system and deriving new design requirements by including wavelength-dependent effects. For instance, the channel spot size on the detector surface will differ based on the channel's central wavelength.

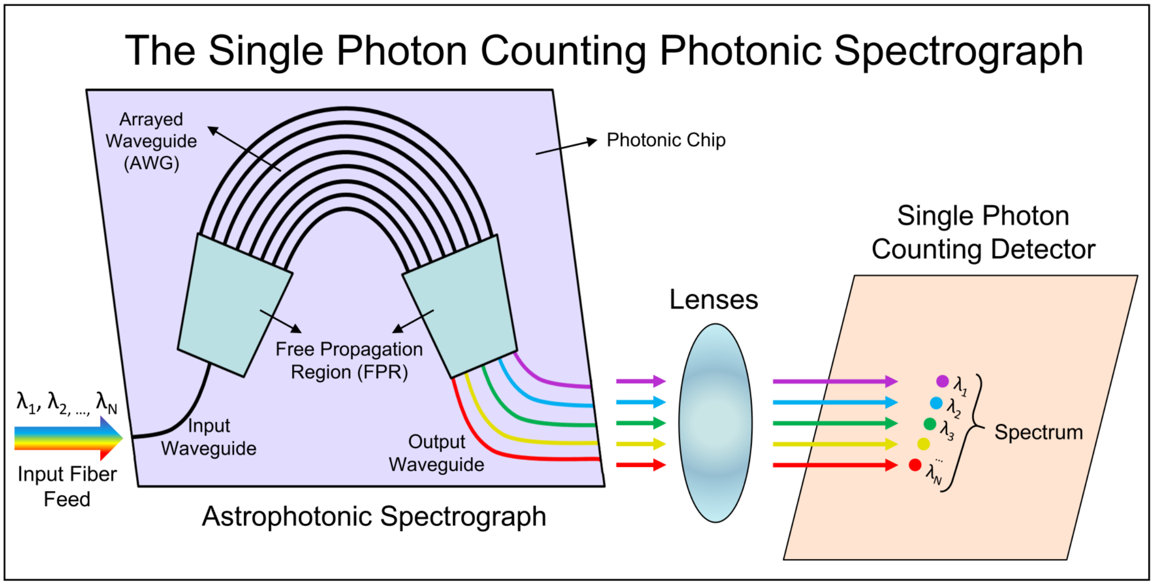

Figure 2.3: Shown above is a schematic of the SPCPS. Light from the targeted object passes through a single-mode fiber connected to the APS that creates the output spectrum. The spectrum then reaches a collimating lens, followed by a camera lens, and the detector receives the final image. The current design uses paraxial lenses, which ignore wavelength-dependent effects.

2.4 Telescope Specifications

The Habitable Worlds Observatory, LUVOIR, and HabEx share the objective of discovering an Earth analog. The important telescope system parameters for this study are the telescope aperture diameter, end-to-end throughput, the contrast ratio necessary for the coronagraph, the detector operating temperature, and detector read noise and dark current. Relevant telescope parameters are listed in Table 2.3. The aperture diameter controls the photon collecting area for all astronomical sources in the field of view. The end-to-end throughput is broadly defined as a measure of the loss of light as it travels through different telescope components, analogous to a detector's quantum efficiency. The contrast ratio for the coronagraph determines the amount of starlight that can be suppressed from the image field before it is captured by the detector. The detector operating temperature affects the thermal dark current rate.

The HWO design is in its infancy, with ongoing efforts and recent moves by the United States Congress to ramp up its realization. Future iterations of this project will benefit from

Table 2.3: Telescope Specifications

Telescope	**HWO** +	**LUVOIR** [3]		**HabEx** [2]	
Model	-	LUVOIR-A	LUVOIR-B	-	
Diameter	6 m	15 m	8 m	4 m	
Telescope Temperature	270 K	270 K		≥ 260 K	
Direct Imaging Instrument	-	ECLIPS-A	ECLIPS-B	SSI (starshade)	HCG (coronagraph)
Contrast Ratio	1×10^{-10}	1×10^{-10}		1×10^{-10}	2.5×10^{-10}
Detector Temperature	-	170 K *		153 K	77 K (A) 153 K (B)
Dark Current	5×10^{-4} [75]	3×10^{-5} e^-/pix/s		$< 10^{-4}$ e^-/s	
Read Noise	0.1 e^-	0 e^-		< 0.1 e^- RMS	

+ using default parameters found at `https://hwo.stsci.edu/coron_model`, which cites [75].
* assumed to be same as HDI from Table 8-5 in [3].

relevant values from the upcoming HWO design. For now, LUVOIR-B is the telescope considered in this study. It is an 8 m telescope, close to the 2020 Decadal Survey's recommended 6 m flagship [1]. Finally, the telescope throughput is estimated at 20% by using throughput values for the Hubble Space Telescope instruments[2] ($\sim 20 - 30\%$) [76] and Table B-9 from [77].

2.5 Astronomical Sources

ExoVista is a comprehensive open-source tool capable of generating random and user-specified stellar systems, and the different astronomical sources within them [78]. This project focuses on a specific case: identifying an Earth twin and detecting the O_2-A band. The stellar systems modeled in this study have host stars from spectral type K5V to F0V, omitting non-integer classes (F9.5V, K0.5V, etc). The spectrum of Modern Earth is used for the different stellar systems. A solar system twin (hereafter named SST) located 10 pc away is also defined, with different Earth eons: Archean Earth, Hazy Archean Earth, Modern Earth, and Proterozoic Earth with low and high levels of oxygen. This highlights that not all habitable planets will

---

[2] `https://www.stsci.edu/hst/instrumentation/wfc3/performance/throughputs`

show a deep O_2-A band feature, contingent upon the life they currently harbor. The SST is the highlighted case study, and results for other systems are in Appendix B and Appendix C.

Default parameters for the exozodiacal dust disk, the Earth's orbit, and stellar system inclination for the solar system twin are used as provided in the exoVista solar system.dat file. All sources for the data used by exoVista are provided in Table 1 of [78]. The exact procedure and execution of the exoVista software is described in Appendix D for a Windows operating system. The stellar system parameters are scaled linearly for other spectral types for the habitable zone r_{HZ} using Equation 1.5.3. The stellar system evolves over time to provide information at different orbital positions, which affects the contrast ratio due to the phases of the exoplanet. ExoVista generates the spectrum of the star, the contrast ratio of the planet against the star, and the contrast ratio for the exozodiacal dust. The planetary contrast ratios are shown in Figure 2.4 and Figure 2.5. The data for the planetary albedo (and thus spectra) are from [79]. The effect of orbital position on the contrast ratio is shown in Figure 2.6.

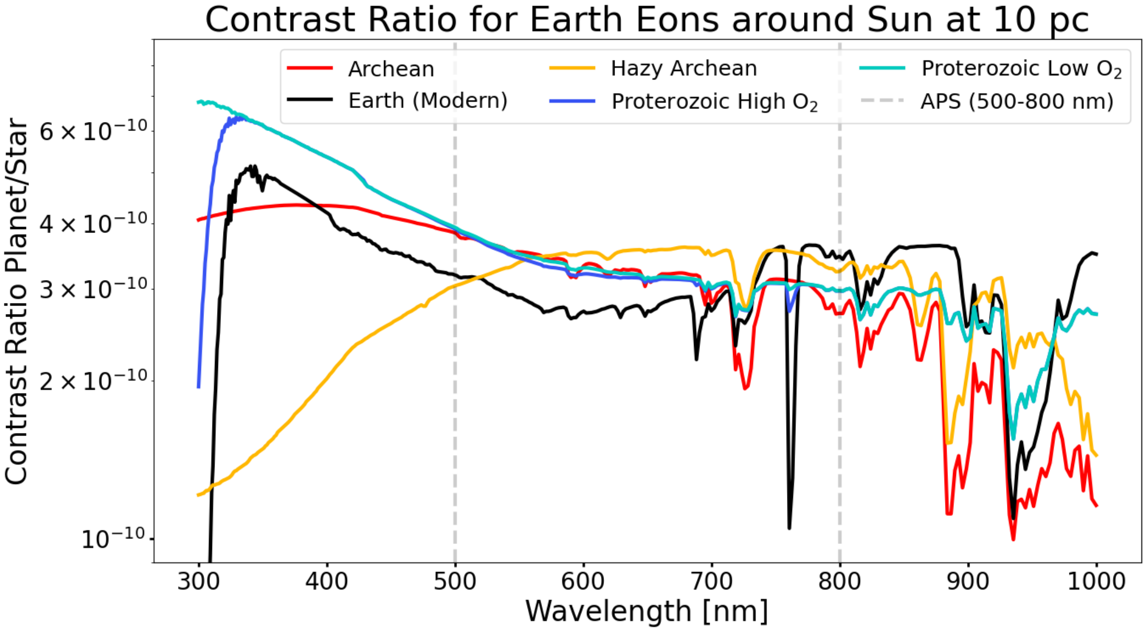

Figure 2.4: Plotted above are the contrast ratios for the planet against the star, for different eons. The planet's orbital position is selected such that the bottom of the O_2-A band absorption feature at 760 nm is just above a contrast of 10^{-10} to meet the coronagraph requirements. Notice that only modern Earth shows a deep O_2-A band feature, while the Proterozoic High O_2 Earth shows only a minor dip.

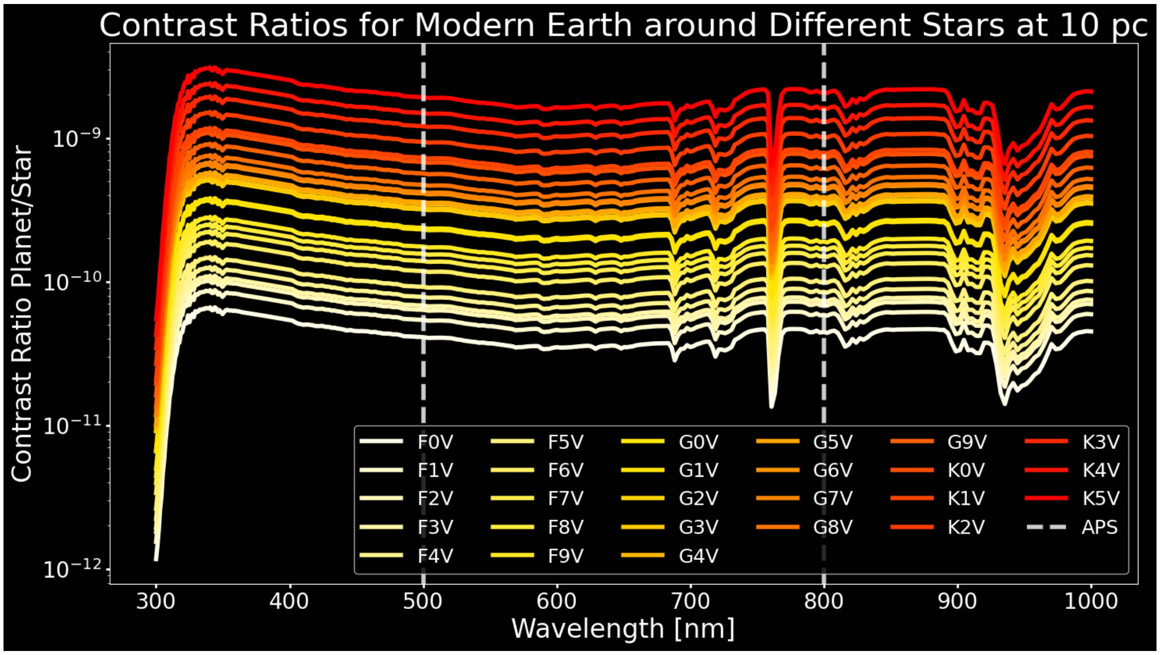

Figure 2.5: Plotted above are the contrast ratios for the planet against the star, for different stars, for Modern Earth only. Notice the contrast ratio for K dwarfs is higher than that of F dwarfs, meaning a K dwarf outshines the exoplanet less than an F dwarf.

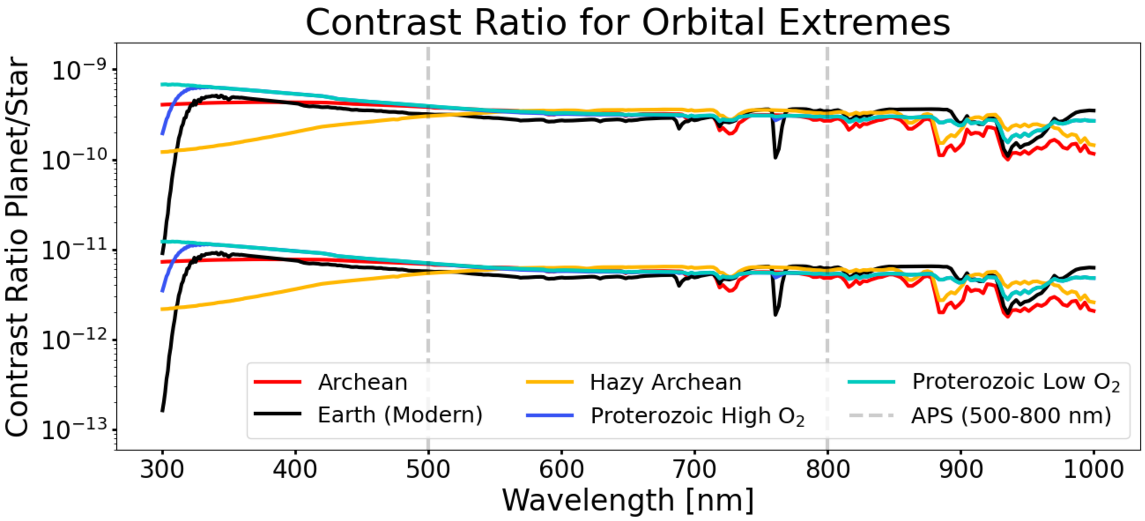

Figure 2.6: Displayed above is the effect of orbital position on the contrast ratio. The position of the planet around its star affects the area of the planet visible to the observer, similar to the phases of the moon or Venus. Notice that at the minimum, the contrast ratio of reflected light is at 10^{-11}, dipping below the coronagraph starlight suppression, and making the detection much more difficult.

The planet's position at the time of observation can affect its detection as it goes through phases like the moon or Venus: we could observe the right system at the wrong time. The selected planet location for the SST satisfies the coronagraph's 10^{-10} contrast requirement by having the bottom of the O_2-A band absorption feature just above that value. For stars brighter than the Sun (G2V), the O_2-A band contrast ratio decreases, making the detection more difficult (see Appendix B). The exozodiacal dust map in Figure 2.15 provides the selected planet location for the SST, the rest are compiled in Appendix C.

The first step is to recover the total flux of the planet. ExoVista divides the planetary spectrum by the stellar spectrum and returns the contrast ratio. Multiplying the contrast ratio by the stellar spectrum yields the total planet spectrum (reflected and emitted). This operation imprints the stellar spectrum in the planetary spectrum, which is inevitable but necessary to obtain the total flux from the planet. Indeed, direct imaging observations of exoplanets will contain spectral features of the light reflected from the star in addition to their own. The stellar spectrum (Sun) is shown in Figure 2.7, and those of other stars in Figure 2.8. The data for the stellar spectra are from [80], as listed in Table 1 of [78].

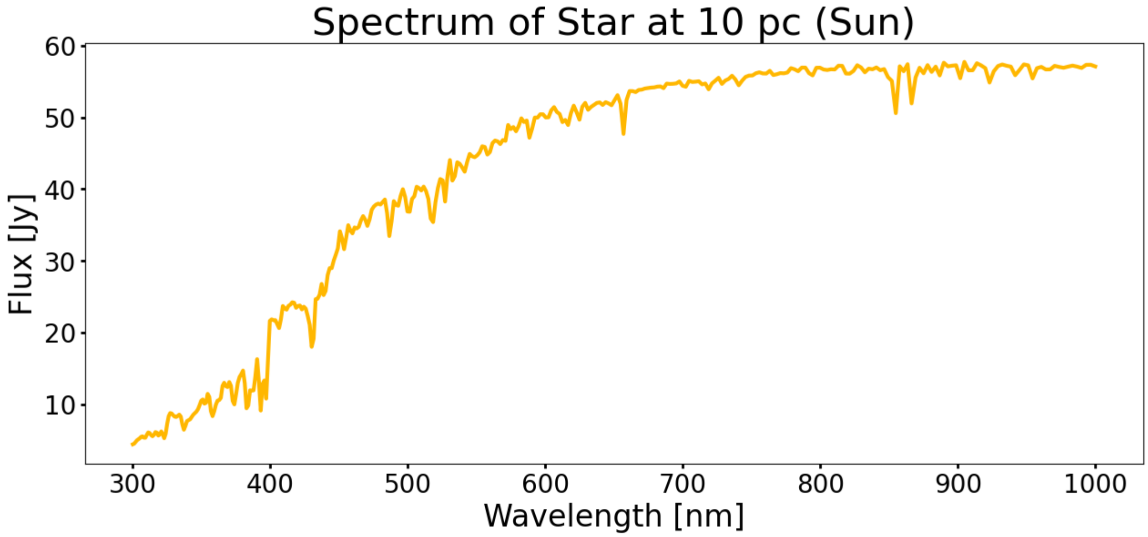

Figure 2.7: Shown above is the intensity of the stellar spectrum (Sun) output by exoVista for a distance of 10 pc. The flux is in Jansky and is later converted into photoelectron counts.

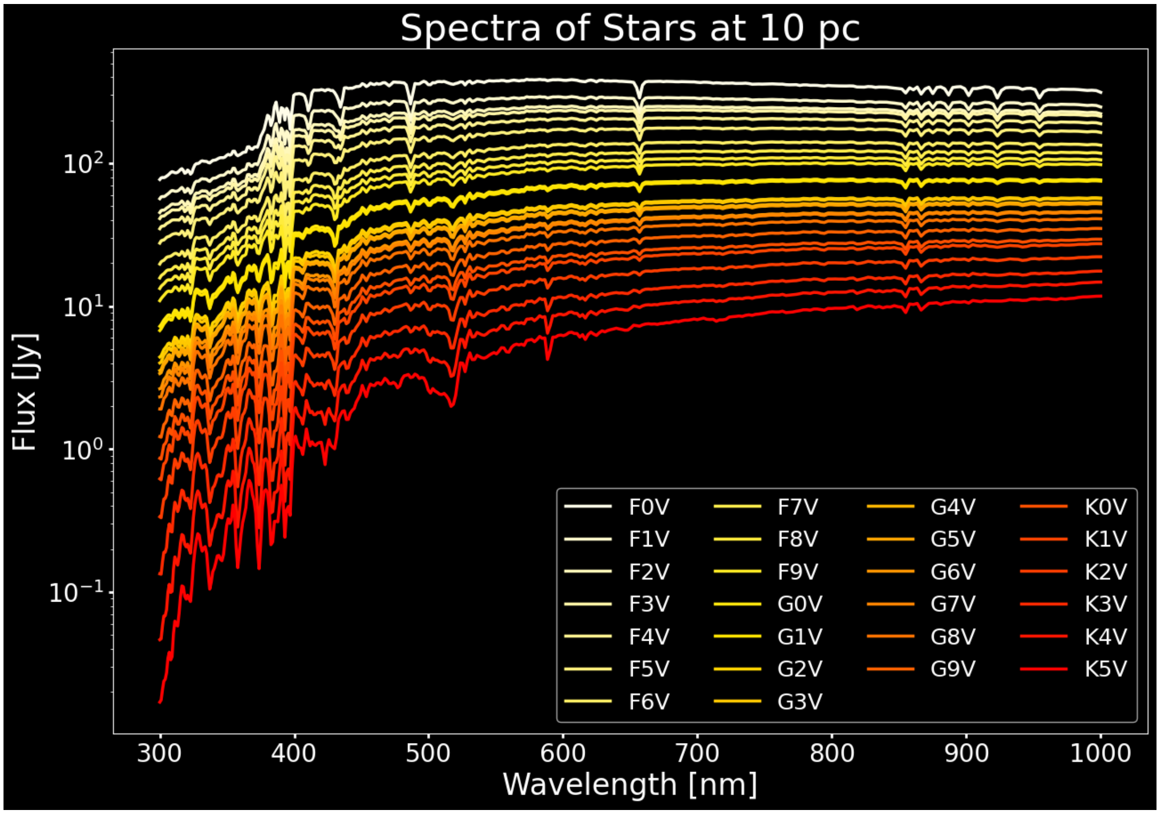

Figure 2.8: Shown above are the intensities of the stellar spectra output by exoVista for a distance of 10 pc. The flux is in Jansky and is later converted into photoelectron counts. Notice the different spectral features due to the stellar temperatures (spectral types). These different features will appear in the reflection spectrum of the exoplanet.

The total light received from the planet is shown in Figure 2.9 for the SST, and in Figure 2.10 for other stars. Recall that the systems are modeled such that the exoplanets receive the same energy (photon flux) as the Earth does at its current location. To first order, the light received from the exoplanets should be similar. Differences arise from the individual stellar spectra due to different blackbody emission and absorption features in the stellar atmospheres. The exoplanet receives the starlight, modulates the spectrum in its atmosphere, then reflects the light and emits its own spectrum. There is a considerable influence from the stellar spectrum in the optical and ultraviolet regimes, since a habitable planet should not be hot enough for significant self-luminosity in those regimes. In fact, the blackbody intensity in the optical (500 nm) at ~1500 K is the same as Earth's blackbody emission peak in the mid-IR (10 μm) for its average surface temperature of ~288 K.

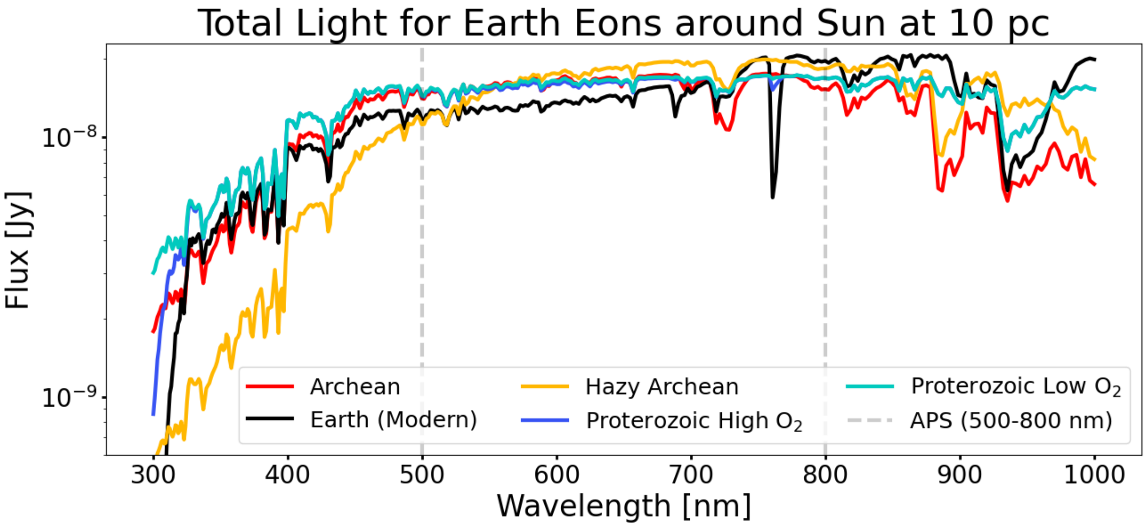

Figure 2.9: The total light spectrum of the planet is shown for different Earth eons. Notice the stellar spectrum contaminates the spectrum, especially below 700 nm. Habitable planets should not be hot enough to emit significant thermal radiation in the optical and ultraviolet regimes.

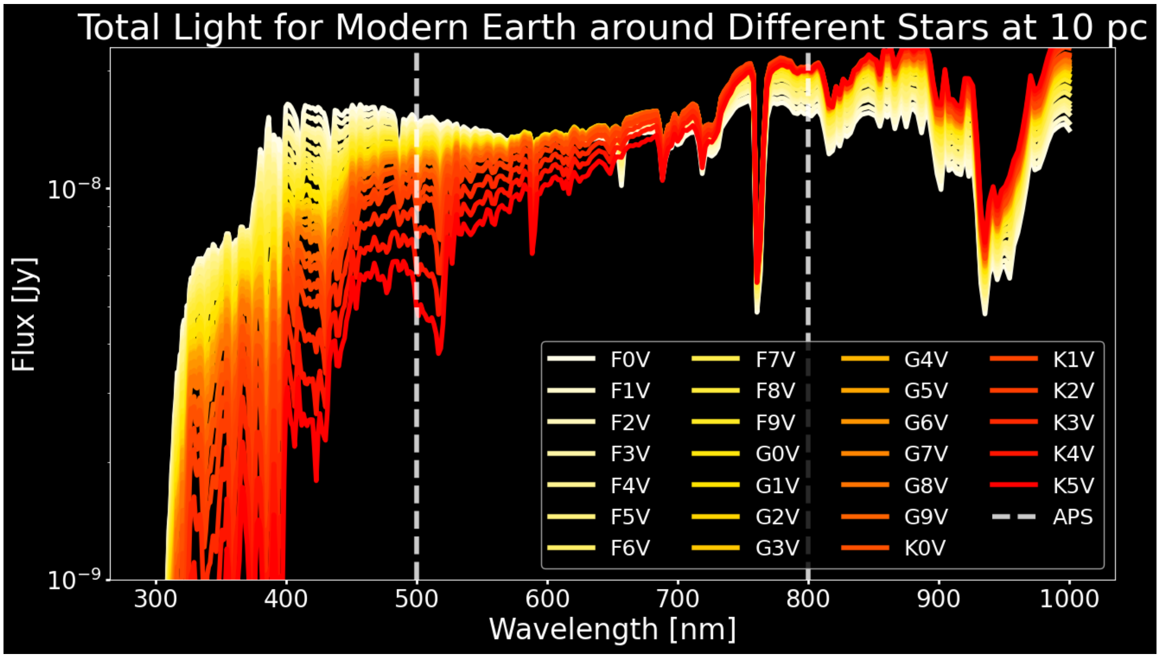

Figure 2.10: This figure shows the total light received from the exoplanet. It is equivalent to Figure 2.9 for Modern Earth only, around different stellar spectral types. Ignoring differences inherited from reflecting different stellar spectral profiles (such as large differences in the UV spectrum across stellar types), the amount of light reflected at 760 nm is roughly the same for all stellar types. This is a definitional effect from modelling all exoplanets in the habitable zone of their host star, since they receive the same integrated photon flux.

Integrating the total light from the planet gives the photon flux per channel. This operation requires defining the resolution of each channel from the input data given to exoVista. The bin size $\Delta\lambda_{\lambda,ExoV}$ is the distance between adjacent midpoints for neighboring data points. The bin sizes of the input data are different, with data at shorter wavelengths being more closely spaced together. The integration amounts to multiplying the bin size by the flux at the given wavelength. The integrated spectrum is then multiplied by the assumed 20% telescope throughput, the collecting area of the 8 m telescope, and the quantum efficiency of the detector using estimated values that match the channel wavelengths (Figure 1.6). The integration is expressed by Equation 2.5.3. Note that the detector QE changes the photon number γ into an electron number. The results for the SST are plotted in Figure 2.11 and Figure 2.12 for other systems.

$$S_{\lambda,p,ExoV} = F_{\lambda,p,ExoV}\,\frac{c}{\lambda^2}\,\frac{\lambda}{hc}\,\Delta\lambda_{\lambda,ExoV}\cdot QE_{\lambda,det}\cdot TP_{tel}\cdot A_{tel}\cdot(1\times10^{-23}\,erg/s/cm^2/Hz/Jy)$$
$$[e^-/s/channel_{ExoV}] \quad (2.5.3)$$

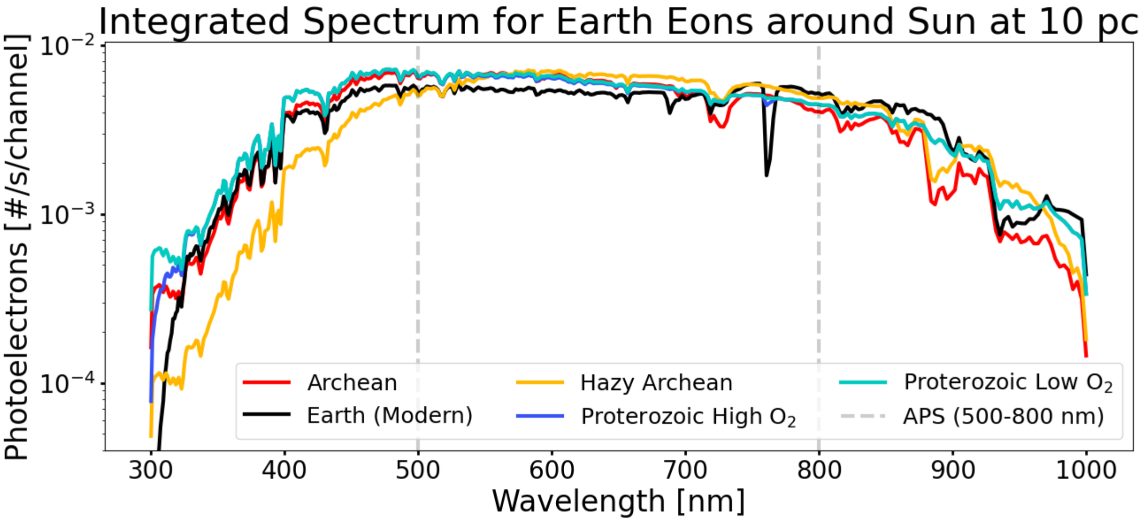

Figure 2.11: This figure illustrates the integrated light spectrum as computed by Equation 2.5.3. Notice the imprint of detector quantum efficiency from Figure 1.6 in the shape of the spectrum. There are only a few photons per hour for the O_2-A band.

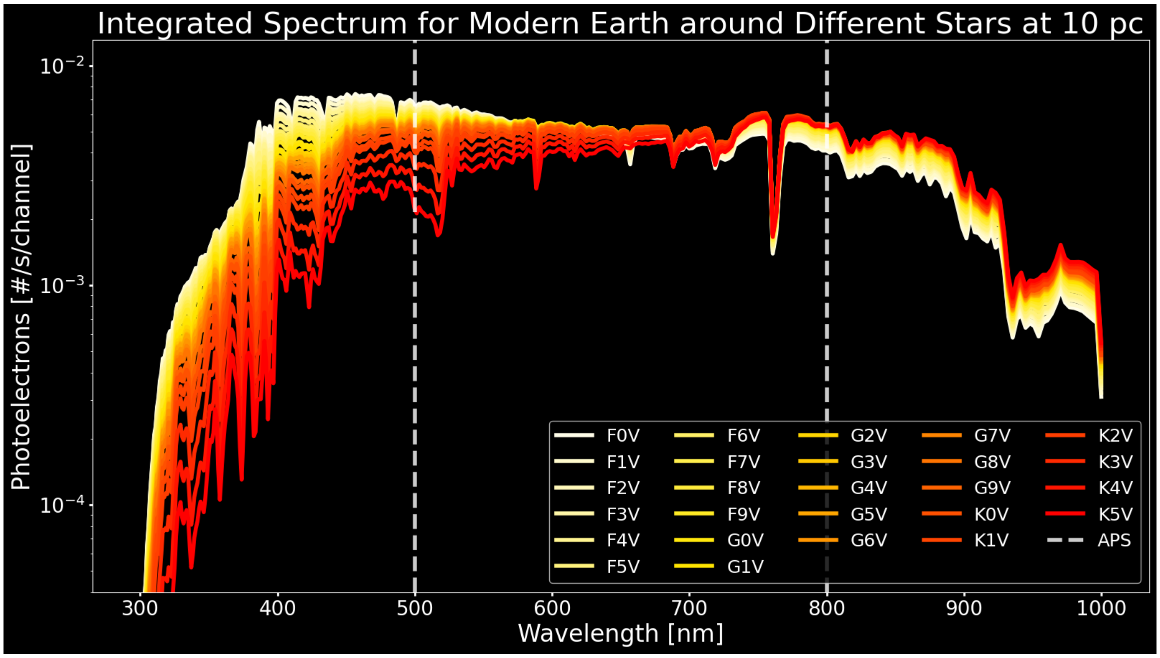

Figure 2.12: This figure is the equivalent of Figure 2.11 for Modern Earth only, for different stellar spectral types considered.

Following the integration of the total light spectrum is rebinning the data to match the APS channel resolution. The 46 APS channels are equally spaced, each having a bandwidth of ~6.5 nm. The results are then multiplied by the APS channel specific throughput. This process assigns the correct number of photoelectrons to each APS channel, and is encapsulated in Equation 2.5.4. The weight w_i represents the fraction of the exoVista channel that is assigned to the APS channel. The final result for the SST is plotted in Figure 2.13, and in Figure 2.14 for other stars.

$$S_{\lambda,p,APS} = TP_{\lambda,APS} \sum_{i=\lambda_1}^{\lambda_2} \frac{w_i \cdot S_{i,p,ExoV}}{\Delta\lambda_{\lambda,APS}} \quad [e^-/s/channel_{APS}] \tag{2.5.4}$$

Equation 2.5.3 and 2.5.4 are applied to the stellar spectrum $F_{\lambda,\star,ExoV}$ to get the stellar integrated flux, $S_{\lambda,\star,APS}$. The exozodiacal dust requires a more careful approach. ExoVista returns the contrast ratio for exozodiacal dust as a map using a broadband spectrum. The data for the dust are in part from [81] and in part from [78]. The results for 744 nm (closest data point to 760 nm), are in Figure 2.15 for the SST and in Appendix B for the other systems.

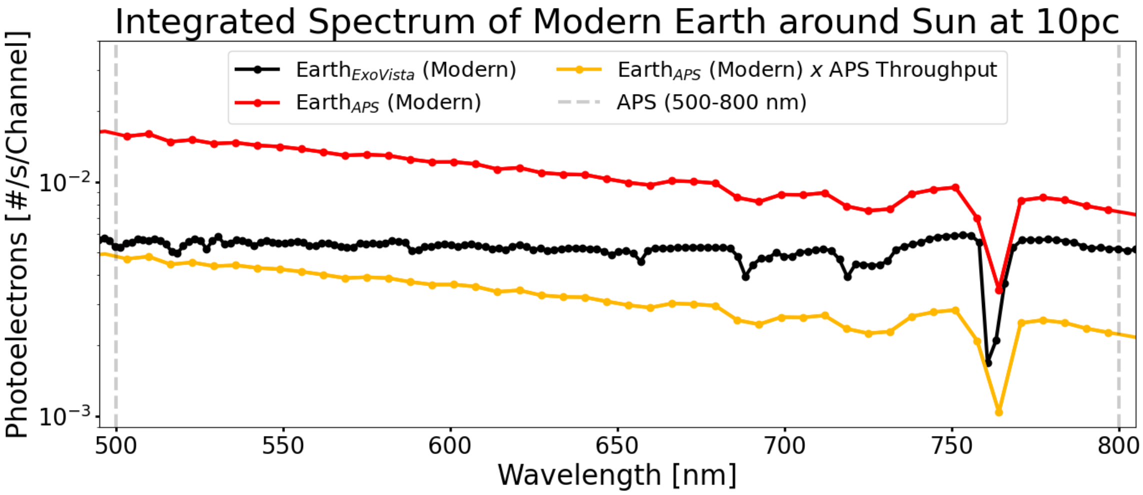

Figure 2.13: The black curve is the integrated spectrum for Modern Earth with resolution from data given to exoVista. The spacing for the input data increases with wavelength. In red is the rebinned integrated spectrum to match the 46 evenly spaced APS channels. Note that moving to lower resolutions (coarser bandwidth) increases the number of photons per channel, explaining the red curve being above the black curve. The effect of the APS channel throughput (30% for all channels), is shown in gold.

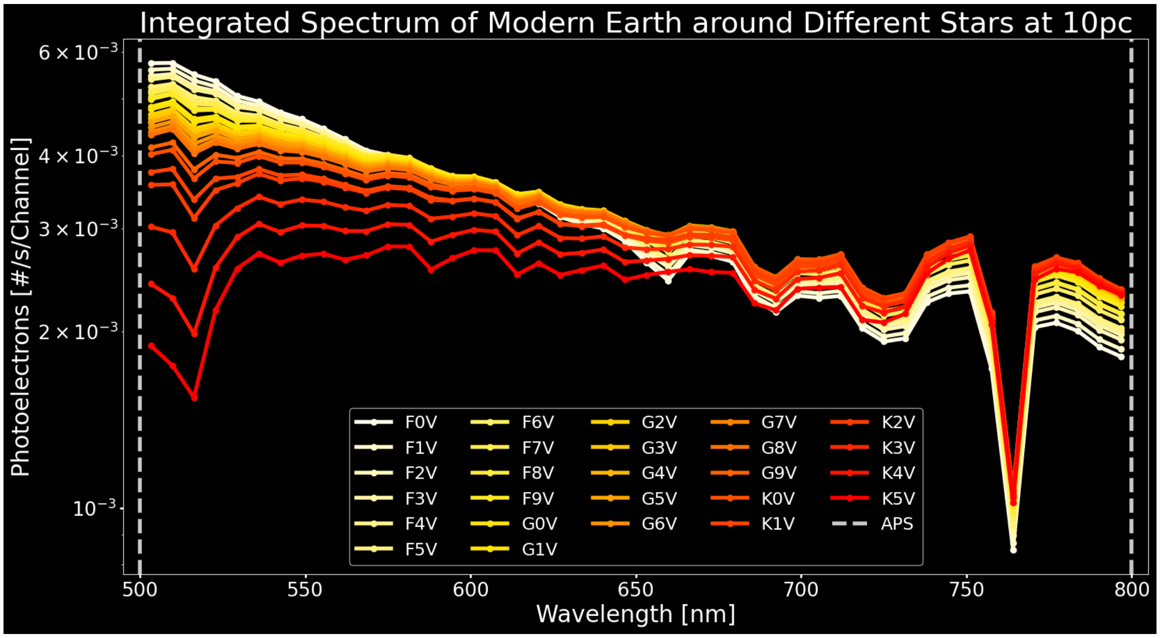

Figure 2.14: The curves above are the equivalent of the gold curve in Figure 2.13. They represent the integrated spectrum of the Earth twin, around other stars at 10 pc, and include the flat 30% spectrograph throughput.

ExoVista pixels in this model have an angular size of 2 mas and area of 4 mas^2. The contrast values thus define the surface brightness of the dust at the pixel location. This means exoVista returns an integrated angular area for the contribution of the exozodiacal dust. Taking the full pixel's surface brightness is too large an area to isolate the exoplanet. For comparison, at a distance of 10 pc, the Earth has an angular diameter of 8.52×10^{-3} mas and cross-section of 5.70×10^{-5} mas^2. That is, the Earth is ∼234 times smaller in length and ∼70,200 times smaller in area than the exoVista pixel. To minimize the integrated surface brightness, a square aperture isolates the planet, as was assumed in [75]. This project uses a square aperture of 0.3 mas in length, comparable to the pixel scale of the LUVOIR-B Optical Telescope Assembly (0.699 arcsec/mm or 0.699 mas/μm) [3]. The 0.3 mas square aperture reduces the integrated surface brightness from exozodiacal dust by ∼50 times the value it would have for the 2 mas pixel.

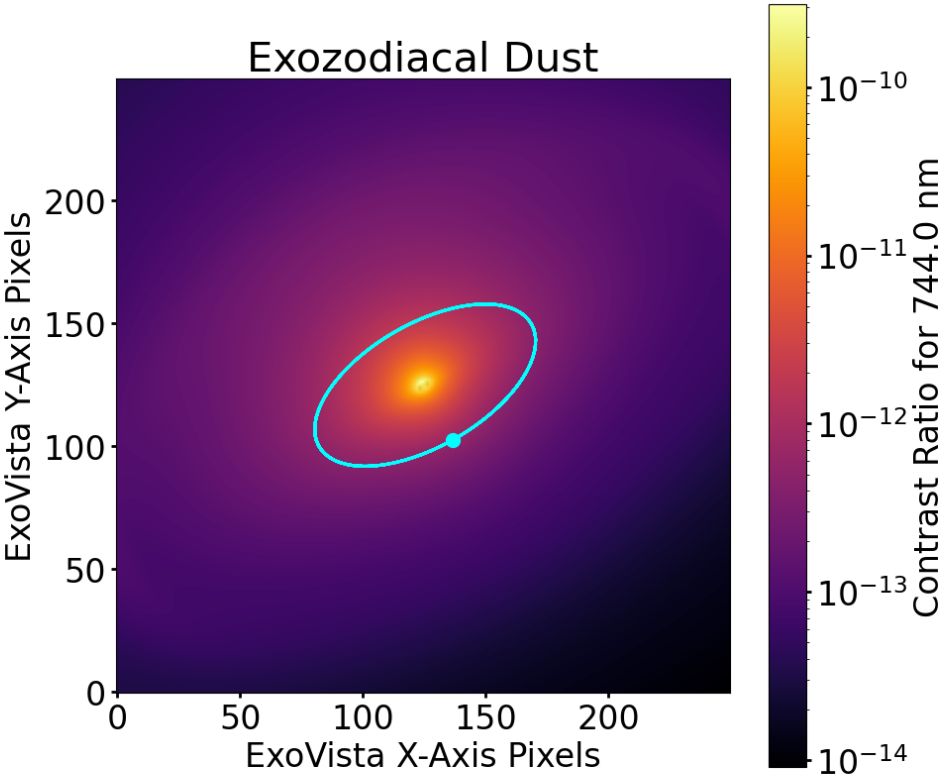

Figure 2.15: The map shows the contrast ratio of the exozodiacal dust computed by exoVista at ∼744 nm for the SST. The pixels are 2 mas in length. The orbit of the planet is shown, the dot is the position at which the bottom of the O_2-A band feature has a contrast of 10^{-10}.

Once the area of the exozodiacal dust is established, Equation 2.5.3 and Equation 2.5.4 recover the integrated spectrum (XZD), with the additional step to rebin the broadband contrast ratio to match the initial stellar spectrum resolution. Finally, the exozodiacal dust cloud appears about two times brighter than the solar system's zodiacal dust, which is observed from Earth as within the cloud [82]. This approximates the integrated local solar system zodiacal dust (ZD) contribution as half of XZD. The astronomical sources' integrated spectra will later apply to the achievable signal-to-noise ratio calculations.

Prior to this, the required SNR defines the limit that the achievable SNR must reach. Thus, Equation 2.5.5 uses the results from Equation 2.5.4 to provide SNR$_{req}$ of the O$_2$-A band absorption feature. Equation 2.5.5 derives from the error on the equivalent width as defined by the fractional error χ = W / ΔW, and then solving for SNR$_{req}$ (see Appendix A and [83]).

$$SNR_{req} = \frac{1.406}{\chi} \cdot \frac{S_{cont}}{S_{cont} - S_{line}} \cdot \sqrt{\frac{\Delta\lambda_{APS}}{FWHM}} \tag{2.5.5}$$

Equation 2.5.6 rewrites Equation 2.5.5 in terms of the equivalent width W, with the derivation shown in Appendix A.

$$SNR_{req} = \frac{1.5\sqrt{FWHM \cdot \Delta\lambda_{APS}}}{\chi \cdot W} \tag{2.5.6}$$

In Equation 2.5.5, the fractional term with S$_{cont}$ and S$_{line}$ defines the absorption line ratio, which is ~2.5 for the O$_2$-A band for the simulated SST observation (Figure 2.13). The equivalent width W in Equation 2.5.6 is ~1.84 nm. Results from Equation 2.5.5 and Equation 2.5.6 are illustrated in Figure 2.16. The black curves in Figure 2.16 represent the simulated observation in this paper (ratio = 2.5, W = 1.84 nm). The other curves demonstrate the line ratio and equivalent width parameter space. The SNR$_{req}$ for a detection with 20% error on the equivalent width is ~20, and is 10 for ~45% error on the equivalent width. The SNR = 10 case is selected for this paper.

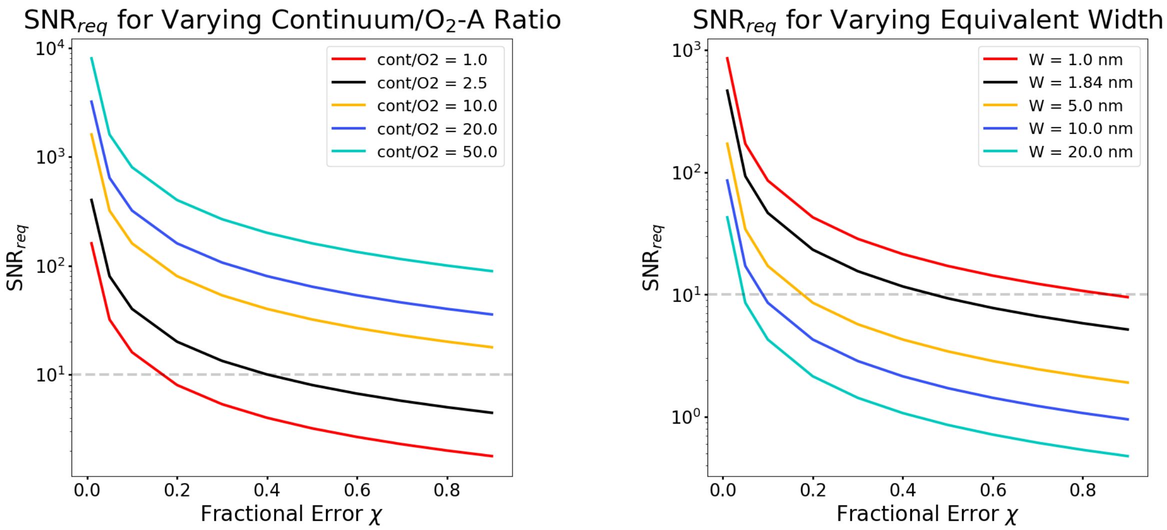

Figure 2.16: *(left)* The SNR$_{req}$ as computed by Equation 2.5.5 explores the parameter space of the continuum to line depth ratio, which is about ∼2.5 from Figure 2.13. *(right)* The SNR$_{req}$ as computed by Equation 2.5.6 considers the equivalent width. The O$_2$-A band has an equivalent width of ∼1.84 nm. *(both)* For a fractional error of 20%, SNR$_{req}$ ∼20. For a fractional error of ∼45%, SNR$_{req}$ ∼10.

2.6 Modelling the SPCPS

The single photon counting photonic spectrograph (SPCPS) has a simple design. It includes an on-chip APS, a collimating lens, a camera lens, and an SPCD. Ray tracing is accomplished using the proprietary Ansys Zemax OpticStudio software. The architecture of the APS is not included fully on Zemax. Instead, 46 source elements represent the 46 output channels. Dr. Gatkine and his team at UCLA are developing the APS using RSoft. Their research will provide the channel-specific throughput and crosstalk for the optical APS. For now, a flat 30% throughput is adopted for all channels, and crosstalk is ignored as it is expected to be less than 1% by design. Each channel will have a bandwidth of about 6.5 nm.

To incorporate the APS in the Zemax model, 46 “Source Radial” elements represent the output waveguides. “Source Radial” elements account for the aperture size of the source (6 μm diameter waveguides), the minimum and maximum opening angles (0 − 90°), and the intensity at each angle. The opening angle is the angle between the outermost ray and the axis of the waveguide. The output of all channels follows a Gaussian distribution that decays to $1/e^2$ at an opening angle of 30°. This implies that a 40° opening angle spans 99% of the channel's intensity. The angle bin resolution is set to 1° to finely sample the Gaussian intensity distribution weights from $0 - 90°$. The total power in each channel is weighted using the results from Figure 2.13 to represent the integrated spectrum, shown in Figure 3.4.

Then, a collimating lens focuses the light into parallel rays. The rays reach the camera lens, which produces the final image on the detector surface. Paraxial lenses keep the preliminary design simple, since these "perfect" lenses ignore wavelength-dependent diffraction effects. Furthermore, the paraxial lenses are perfectly flat. The omission of real lenses, which would account for wavelength-dependent effects and curved shape, relaxes focal length requirements. This makes all channels equidistant from the collimating lens regardless of their location on the APS. Both lenses are currently set to a focal length of 5 mm, which keeps the total SPCPS length to ∼15 mm. Since both lenses have the same focal length, there is no magnification by these lenses in the system. The detector lies at the focal plane of the camera lens. The detector surface on Zemax matches the BAE HWK4123 pixel plane. It contains 4096×2304 pixels with 4.6×4.6 μm dimensions.

The only variable this treatment leaves is the position of the APS channels with respect to the focal plane of the collimating lens, which relates to the number of pixels used to image each channel. For instance, placing the APS channels at exactly the focal plane of the collimating lens results in the 6 μm diameter waveguide image to be mapped onto the 4.6 μm pixels. That is close to a 1:1 ratio, which has benefits and drawbacks. The benefit is that using less pixels results in lower total dark current and read noise, since both scale as the number of pixels. The drawback is that the channel image is vulnerable to defective pixels and transient events, such as cosmic rays.

Thus, the parameter space of the distance between the APS channels and the focal plane of the collimating lens is explored in this work, with one limitation. Suppose the APS is sufficiently far away, such that the "output cones" of neighboring channels begin to overlap. This overlap will be present on the detector surface as well, resulting in channel contamination. I restrict this overlap to be 1% of the intensity of a neighboring channel, and define the maximum distance d_{max} the APS is allowed to be from the focal plane of the collimating lens as:

$$d_{max} = \frac{0.5\,(channel\ core\ spacing \quad - \quad waveguide\ diameter)}{\tan\theta_{99\%}} \tag{2.6.7}$$

where $\theta_{99\%}$ is the opening angle for which 99% of the Gaussian intensity profile is emitted, and the numerator comes from considering the geometry.

In our model, the channel core-to-core spacing is 100 μm and the waveguide diameter is 6 μm. The angle $\theta_{99\%}$ is 40°, which yields $d_{max} = 56$ μm. The channel core-to-core spacing sets the upper limit on the number of pixels, since the limiting case would allow the channel light cones to expand and graze each other on the detector surface. For 100 μm channel core spacing and 4.6 μm pixels, the maximum waveguide image spans a diameter of $\sim$22 pixels, so a maximum area of 416 pixels.

Chapter 3

Results

The performance of the single photon counting photonic spectrograph can be defined by the amount of time required to reach a desired SNR with a given error on the equivalent width of the target feature. Section 3.1 describes the achievable signal-to-noise ratio by the SPCPS on a LUVOIR-B class telescope, and Section 3.2 covers the SPCPS design based on SNR.

3.1 Achievable Signal-to-Noise Ratio

The achievable signal-to-noise ratio (SNR$_{achi}$) is the fraction of the total target counts over the square root of the total noise counts. The target is the integrated planet spectrum. The major sources of noise considered are: shot noise from detector dark current and read noise, and shot noise from astronomical sources which are the planet, starlight leaking from the coronagraph, zodiacal dust, and exozodiacal dust. Equation 2.5.4 defines the integrated planet spectrum (the square root of which gives planet shot noise), the starlight spectrum, and the exozodiacal dust (XZD). The zodiacal dust (ZD) is approximately half of the XZD [82]. The starlight leakage is defined as K$_{CR}$×S$_{\lambda,\star}$, where K$_{CR}$ is the contrast ratio achieved by the coronagraph [84]. The dark current is from Equation 2.2.1 and the read noise from Equation 2.2.2. Combining these parameters together, SNR$_{achi}$ becomes:

$$SNR_{achi} = \frac{S_{\lambda,p} \cdot t}{\sqrt{(S_{\lambda,p} + K_{CR}S_{\lambda,\star} + DC + ZD + XZD) \cdot t + RN^2}} \tag{3.1.1}$$

The variables implicit in Equation 3.1.1 are the detector temperature and the number of pixels n_{pix}, which affect the dark current and read noise (see Equation 2.2.1 and 2.2.2). Further, SNR_{achi} must meet the requirement of 10 set by the selected SNR_{req} from Equation 2.5.6 and Figure 2.16. Exploring the parameter space of detector temperature and number of pixels provides the integration time needed for a given combination. The temperatures considered are 70 K, 153 K, 170 K, and 270 K, motivated by the telescope parameters in Table 2.3. The areal number of pixels considered are 1, 4, 9, 25, and 416 pixels, which would span circles of diameter 1, 2, 3, 5, and 22 pixels respectively. The 22 pixel case is the upper limit before the channel images on the detector surface begin overlapping. Note that the areal number of pixels includes fully and partially covered pixels. This is because partially covered pixels cannot partially read out their charge, and thus the entire dark current and read noise contributions are made for those pixels.

Based on the desired integration time and SNR_{achi}, the number of pixels flows down to the SPCPS design. Recall the number of pixels used to image an APS channel on the detector affects the required distance between the channels and the focal plane of the collimating lens. The results for SNR_{achi} for the SST are shown in Figure 3.1 and Table 3.1. Similar plots to Figure 3.1 for other stars are in Appendix B. To first order, the time required to reach a desired SNR_{achi} decreases with decreasing stellar luminosity. However, the improvement in integration time shows oscillatory behavior or perhaps a plateau for G and K dwarfs, but is beyond the scope of this paper.

The achievable SNR by the system strongly depends on the number of pixels imaging the APS channel due to dark current. The blue curve in Figure 3.1 represents the LUVOIR 170 K detector temperature, for which $SNR_{achi} = 10$ takes 17, 35, 63, 154, and 2381 days of exposure time for 1, 4, 9, 25, and 416 pixels respectively. This gives a slope of $\sim$5.7 days/pixel (intercept $\sim$11.7) for $SNR = 10$, which is the integration time cost for using more than one pixel.

The 9-pixel case is selected as the upper limit for the pixel number requirement to flow

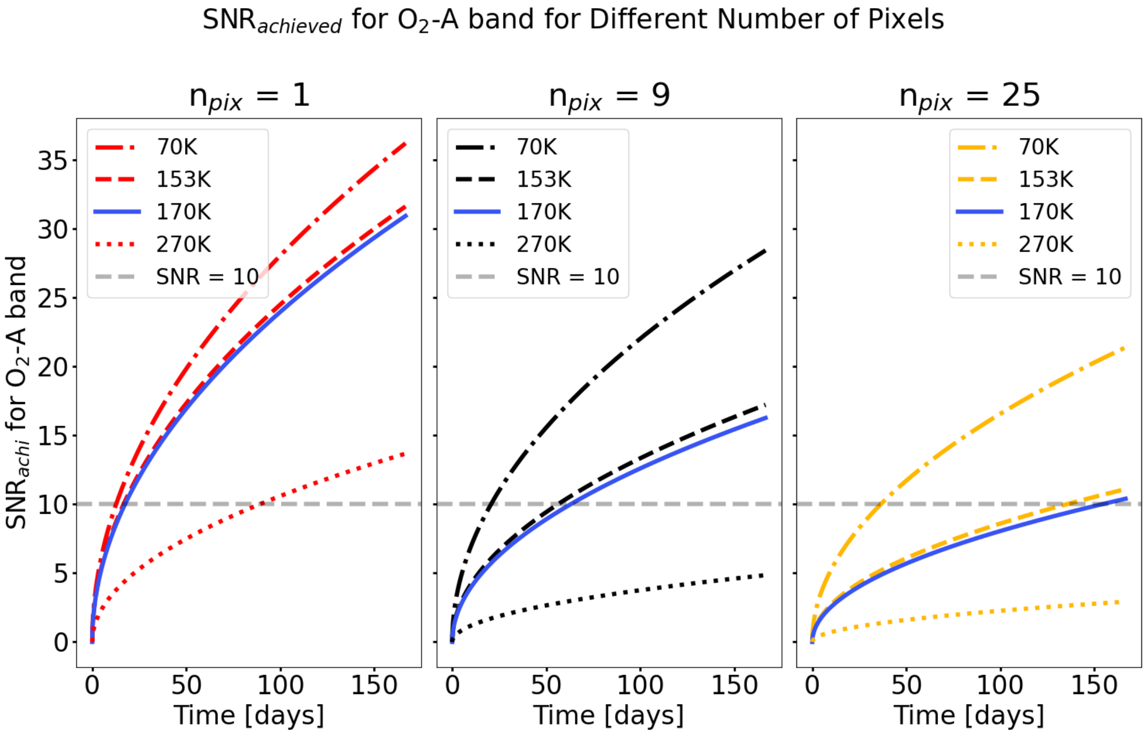

Figure 3.1: The panels show the effect of temperature and pixel number, both of which affect dark current, on the integration time required for SNR$_{achi}$, for the solar system twin. The LUVOIR detector temperature (170 K) is the solid blue curve. Considering the 170 K case, for 1 pixel, it takes ∼17 days to reach SNR = 10. For 9 pixels, it takes ∼63 days, and ∼154 days for 25 pixels. Not plotted above, the case for 4 pixels takes ∼35 days and 416 pixels takes ∼6.5 years to reach SNR = 10 for 170 K.

Table 3.1: SNR relation to pixel number and detector temperature

	1 pixel	4 pixels	9 pixels	25 pixels	416 pixels
Integration Time [days] *	**17.43**	**34.50**	**62.95**	**154.02**	**2381.4**
SNR (70 K)	11.17	14.84	17.48	20.57	23.73
SNR (153 K)	10.23	10.47	10.58	10.67	10.73
SNR (170 K)	**10.00**	**10.00**	**10.00**	**10.00**	**10.00**
SNR (270 K)	4.42	3.28	2.98	2.81	2.72

* the integration time is given such that SNR = 10 for 170 K.

down to the SPCPS design. The APS channel is sampled by 9 pixels, providing some robustness against defective pixels and single event upsets (i.e. cosmic rays), but incurring higher integration times. The HWK4123 characterization and investigation in the dark current floor at lower temperatures will determine whether the floor overestimates dark current values. If the sensor shows no dark current plateau, then the dark current values will be lower than those used here, and would decrease required integration times for the same number of pixels.

3.2 The Optical Setup of the SPCPS

The SPCPS has three main sections: the astrophotonic spectrograph, the collimating and camera lenses, and the single photon counting detector. The distance between the APS and the collimating lens focal plane determines how much the APS channel output light can spread, as described by Equation 2.6.7. To select this distance, replace the numerator in Equation 2.6.7 entirely by the desired channel image radius.

The achievable SNR provides the required number of pixels that the APS channel maps onto. The selected area of 9 pixels has a diameter of 3 pixels. Using the desired channel image radius (half of 3 pixels of 4.6 μm), and $\theta_{99\%}$=40°, the distance between the APS channels and the focal plane of the collimating lens is given as 8.22 μm by Equation 2.6.7. This offset allows the light of the channels to spread to a circle of diameter 3 pixels that contains 99% of the channel's intensity.

At this stage, the focal length of the lenses is arbitrary, given the choice to use paraxial lenses, which provide perfect optics. For now, the collimating lens has a focal length of 5 mm. This places the astrophotonic spectrograph at a total distance (offset + focal length) of 5.00822 mm away from the collimating lens. The camera lens has a focal length of 5 mm, positioning it 5 mm behind the collimating lens. To maintain the image size (i.e. no magnification), the detector surface is placed 5 mm behind the camera lens, which is the location of the camera lens focal plane. Thus, the total free space from the channels of the APS to the surface of the detector is the sum of the space between the APS and the collimating lens (5.000822 mm), the collimating lens and the camera lens (5 mm), and the camera lens and the detector (5 mm). The total free space is thus 15.00822 mm.

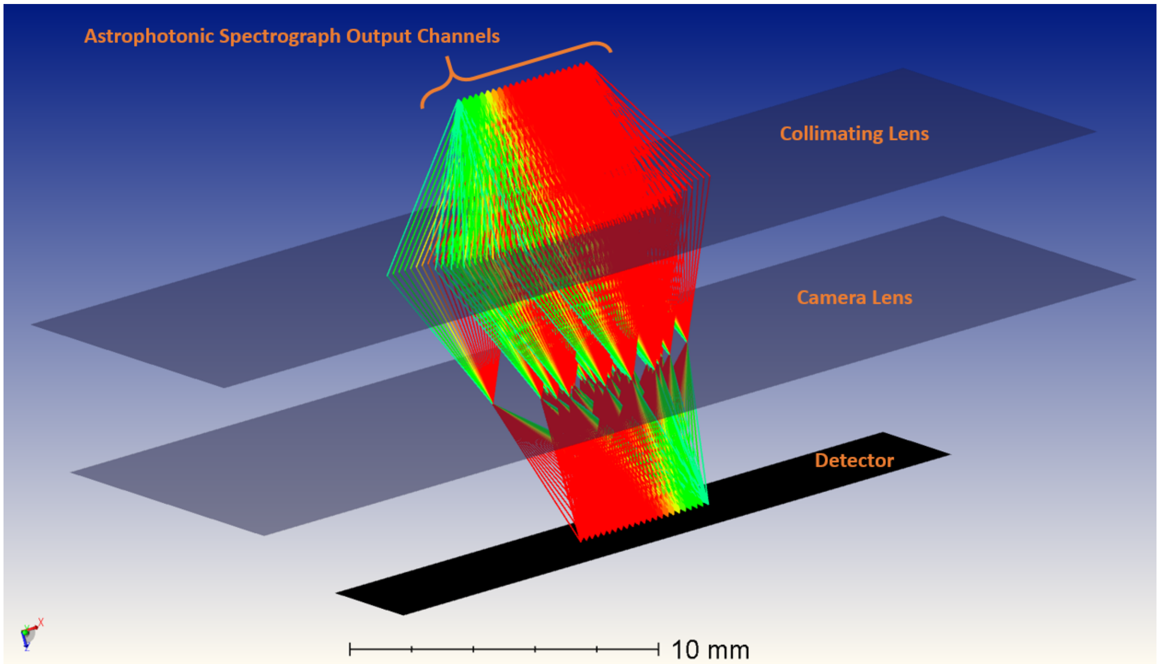

Figure 3.2: The SPCPS instrument is shown as modeled on Zemax. The collimating lens and camera lens each have a focal length of 5 mm. The offset between the astrophotonic spectrograph output channels and the focal plane of the collimating lens is 8.22 μm. The total system length is ~15 mm.

The setup returned by Zemax is in Figure 3.2. The spreading of channel light due to the offset is illustrated in Figure 3.3. Only 23 channels are shown in these figures, to provide a better view of the discretized channels. The colors displayed in the ray tracing are representative of the central wavelength of the channels, which span 500 – 800 nm.

For simplicity, the lenses used are paraxial lenses, which ignore all wavelength-dependent effects. Further, the lenses are perfectly flat, which ignores the effects of channel location on the APS with respect to the curvature of the lens. These dependencies will be explored in future work, and will affect the amount of pixels that the channels are imaged onto. That is to say, using real lenses will affect the APS output channels offset from the focal plane of the collimating lens.

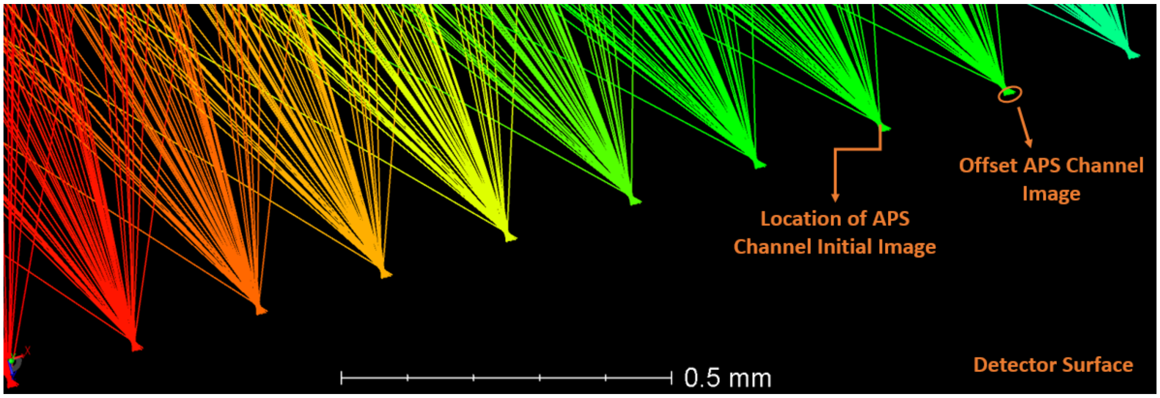

Figure 3.3: This image magnifies Figure 3.2 to highlight the effect of placing the APS channels at an offset from the focal plane of the collimating lens. The cross-section of the expanding light cone (a circle) from the channels reaches the focal plane of the collimating lens, and eventually the detector surface.

To further demonstrate the discretized nature of the output spectrum, the 22-pixel case is shown below in Figure 3.4. Although this is not the selected design for the SPCPS due to the oversampling of the channel in a photon-starved application, it best highlights the Gaussian shape of the channel output as well as the design choice to avoid overlap between channels. The "counts" values reported in Figure 3.4 are not to be used for interpretation in this paper, as the Zemax model used here normalized the results from Figure 2.13 and used Watts. A unit conversion with Zemax output is straightforward, but not required at this stage in the design considerations, since Zemax is used for the optical components only.

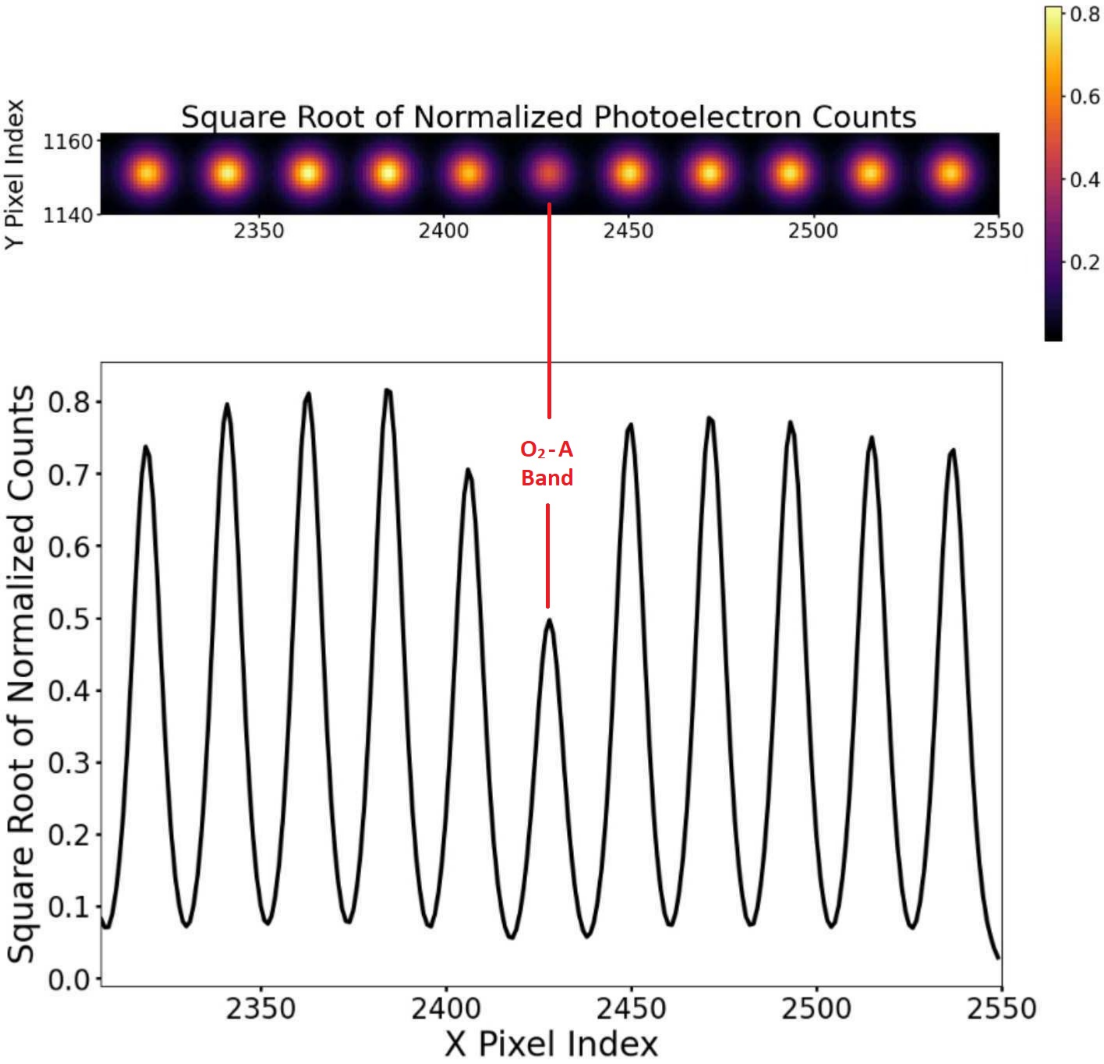

Figure 3.4: The image at the top shows the discretized output channels for the APS on the detector for the 22-pixel case. The selected channels span 728-800 nm and include the O_2-A band. The curves in the lower panel show the isolated Gaussian channels, with minimal overlap on the detector surface. The data used for the amplitude of the channels came from the results of Figure 2.13.

Chapter 4

Discussion

The single photon counting photonic spectrograph can provide measurements of the O_2-A band biosignature with an SNR of 10. The selected design of the SPCPS requires ∼15 mm of free space for the optics. The APS and SPCD are only a few centimeters in size, making the instrument about the size of a shoe box. The instrument includes all parts between the single mode fiber that feeds into the APS and the SPCD. The telescope parts, cooling systems, and readout circuits are not part of the optical model for the SPCPS.

The number of pixels used to image the APS output channel affects the required integration time. The selected 9-pixel case results in an integration time of $\sim 10^3$ hours. This timescale is comparable to that found on the HWO Planet Spectrum Simulator[1], which is based on methods from [75]. The number of pixels impacts SNR_{req} and the integration time as the planet's signal spreads over pixels that each contribute dark current and read noise.

The instrument resolution and the target biosignature also govern the total integration time. As demonstrated in Figure 2.16, biosignatures with larger equivalent widths require lower SNR for a given fractional error on the equivalent width, and thus lower integration times. The choice of the O_2-A band biosignature derives from its importance in the Earth's atmosphere as an indicator of photosynthesis. For instance, detecting water absorption features with broader equivalent widths may be easier to achieve, but water alone may not indicate photosynthesis,

---

[1] `https://hwo.stsci.edu/coron_model`

a biological process. Further, we caution that biosignatures need the context of the entire planetary spectrum and model atmospheres to avoid false positives, even for the O_2-A band [21] [24] [25] [27] [28] [29].

The required integration time uses assumed values that will change the current results when replaced with known values. The assumed values are listed from most to least impactful on SNR_{req} and integration time: the detector dark current, the square aperture to isolate the planet, the zodiacal dust model, and the telescope and spectrograph throughput. The following paragraphs describe the impact of each assumption.

The detector dark current is the highest source of noise in this study and directly correlates to SNR_{req} and integration time. Dark current values for the HWK4123 sensors for lower temperatures are anticipated from the CfD characterization program. For now, two methods estimated the dark current and returned contrasting values (Table 2.2). The doubling temperature gives dark current at the 10^{-5} magnitude required in Table 2.3 for the habitable exoplanet direct imaging application. However, the dark current floor and scaling method from the previous QIS characterization returns a dark current of about 10^{-3} $e^-/s/pix$. Scaling the results to the HWK4123 sensors provides conservative values for the dark current and thus higher integration times. Whether the dark current floor exists in the HWK4123 sensors is a question that the characterization by the CfD will answer.

The size of the square aperture determines the amount of background astronomical sources integrated with the planet. This means larger photometry apertures allow more zodiacal, exozodiacal, stellar, and interstellar backgrounds to permeate the region that feeds light into the spectrograph. The largest surface brightness component is the exozodiacal dust. The eventual HWO design should provide the photometry aperture.

Zodiacal dust is an astronomical background source that degrades the SNR and increases integration time. The zodiacal dust model in this study is approximated as twice as dim as the exozodiacal dust, but may not be entirely accurate depending on the inclination of the exozodiacal dust with respect to the observer [82]. As such, decoupling the zodiacal dust model in future works will affect the integration time, since zodiacal dust counts are on the same order of magnitude as those expected from the exoplanet.

Current efforts to model and design HWO will provide a value for the telescope throughput. The updated value will apply to future work in this project, if available. Similarly, the optical APS model will provide the simulated spectrograph throughput. Then, fabricating and characterizing the APS will provide measured throughput values to apply to this study.

The telescope and spectrograph throughput affect the astronomical sources, per wavelength, and should only have an order of magnitude effect on the derived values. Thus, they should have the least impact on the required integration time.

The assumed values above directly impact the total integration time required to achieve a desired SNR. The integration time directly relates to the number of pixels that can be used to image the channel, which in turn affects the design of the SPCPS. A reduction in the integration time may allow more pixels to image the channel, or to simply image more planets within a given time budget.

Additionally, cosmic rays are omitted from this project. The main effect of cosmic rays is to limit the maximum integration time of each read [75]. Currently, the number of reads required is determined by dividing the total noise counts (astronomical sources and dark current) by half of the full well depth of the HWK4123 pixels (7,000 e^-) to stay in the linear integration regime of the detector. Future work will investigate whether the full well depth or cosmic ray strikes are the limiting factor for the maximum read time.

The instrument design currently uses paraxial lenses that ignore all wavelength-dependent effects. The perfect lens assumption does not appreciably affect the achievable SNR, as low-loss lenses will transmit most of the light. Instead, the perfect lenses have simplified the optics of the system. Wavelength-dependent effects, such as diffraction, will affect the channel image location on the detector. Future work will extensively explore these effects on the SPCPS design.

Chapter 5

Conclusion

NASA plans to deploy New Great Observatories, the first of which is the Habitable Worlds Observatory. A primary goal of HWO is to directly image terrestrial exoplanets, which emit only a few photons per spectral channel per hour [6] [7]. This requires high contrast imaging using a coronagraph and detectors with low read noise and dark current. To determine the habitability of the terrestrial exoplanets, spectrographs provide the planet's spectrum. Current spectrograph designs, such as LUVOIR ECLIPS, will weigh $\sim$ 1000 kg [3] [9]. To reduce mission costs, instrument weight, and maintain instrument performance, we modelled a single photon counting photonic spectrograph (SPCPS), which uses a compact on-chip astrophotonic spectrograph to replace traditional designs and a single photon counting CMOS detector for its performance.

This study considers the O_2-A band biosignature at 760 nm for the Earth in a solar system twin located 10 pc away. This biosignature reveals the presence of O_2, a byproduct of photosynthesis and thus life on Earth. The SPCPS design flows from the SNR requirements to detect the biosignature. The current design uses perfect lenses, which ignores wavelength-dependent effects.

This project defines the required SNR (SNR_{req}) based on the error in the equivalent width of the target absorption line. We select an error of 45% in the equivalent width at an SNR_{req} of 10. The achievable SNR (SNR_{achi}) is then determined by system parameters and astronomical sources, which limit the integration time. The variable that drives the SPCPS design in the SNR_{achi} is the number of pixels used to map the APS channels on the detector. The number of pixels affects the dark current and read noise, and thus the integration time. The contribution to SNR_{achi} from astronomical sources is held constant. Thus, the number of pixels used to image the APS channels is derived from the integration time required to reach a desired SNR. The number of pixels used to map the channel should not oversample the channel and degrade SNR, but should also be resilient to damaged pixels, particularly due to radiation degradation in space. We choose to map the channels on a circle of 3 pixels in diameter (9 pixels total). We estimate that this choice places a constraint of two months of integration time to reach SNR_{achi} = 10. Using 3 pixels to span the width of the channel slightly oversamples the channel, at the cost of increased dark current, read noise, and integration time, but for the benefit of a more damage-resilient channel.

The number of pixels to image the channel also influences the system's optics. We find that an offset of 8.22 μm between the APS and the focal plane of the collimating lens is required to allow the channel light to spread sufficiently to produce a channel image that is 3 pixels in diameter on the detector surface.

The SPCPS presents a new technology with applications that are not limited to HWO. The SPCPS can be used in small satellite missions such as CubeSats, can enhance the bandwidth of telecommunication in the optical regime, and can serve in monitoring systems for environmental or military sensors. In its preliminary models, the SPCPS demonstrates competitiveness with current models made for the HWO, which estimate only half the integration time as the SPCPS needs to detect the O_2-A Band for SNR = 10, thus on the same order of magnitude (see `https://hwo.stsci.edu/coron_model`). The better integration time for the HWO models is partially due to the fact that a lower dark current is used for the detector.

Many assumptions made in this paper will be resolved in future work, which will provide a better understanding of the SPCPS performance. The most impactful assumption is the HWK4123 sensor's dark current at lower temperatures, which will be measured by the Center for Detectors at RIT with the NASA Strategic Astrophysics Technology (SAT) program Grant

No. 80NSSC24K0372.

The first order model presented in this paper shows potential for the SPCPS to perform well in low-flux spectroscopic applications, such as direct exoplanet imaging. The model will be updated and refined in future work to provide a new instrument for the astronomy community.

Appendices

Appendix A

Equivalent Width

This section describes the derivation of the required signal-to-noise ratio defined by the error on the equivalent width of the target line feature. The treatment in [83] assumes a Gaussian absorption line of depth "a," surrounded by a locally flat continuum S_c, and derives the error on the equivalent width of such a feature for a given sampling size (the "pixel" resolution element) of the spectrum.

Adapting Equation 6' from [83] gives the error on the equivalent width, ΔW, as:

$$\Delta W = \frac{1.5\sqrt{FWHM \cdot p}}{SNR_p} \tag{1.A}$$

where FWHM is the full-width at half maximum of the absorption line, "p" is the "pixel" size (resolution element), and SNR_p is the signal-to-noise ratio of the resolution element. The resolution element is defined by the astrophotonic spectrograph channel size $\Delta\lambda_{APS}$. Moving forward, "p" is rewritten as $\Delta\lambda_{APS}$, and SNR_p will be SNR_{req}, the required SNR on the equivalent width based on ΔW.

Another way to define ΔW is to represent it as a fraction χ of the equivalent width W, as:

$$\Delta W = \chi \cdot W \tag{2.A}$$

Given that the absorption feature is assumed to be Gaussian, a relation can be defined between the equivalent width W and the standard deviation of the Gaussian feature. Recall that a Gaussian $f_G(x)$ is defined as:

$$f_G = a \cdot e^{-\frac{1}{2}\left(\frac{x-b}{\sigma}\right)^2} \tag{3.A}$$

where “a” is the amplitude, “b” is the line center, σ is the standard deviation, and x is any location on the Gaussian. The relation between σ and FWHM (and thus W) is:

$$FWHM = 2\sqrt{2\, ln(2)} \cdot \sigma = 2.35\, \sigma \tag{4.A}$$

Finally, the non-normalized area under a Gaussian curve, A_G, is defined as:

$$A_G = \int_{-\infty}^{\infty} f_G(x)\, dx = a \cdot \sigma \cdot \sqrt{2\pi} = a \cdot FWHM \cdot \frac{\sqrt{2\pi}}{2.35} \tag{5.A}$$

The equivalent width is defined as the width of the rectangle that has the same height as the local flat continuum S_c surrounding the absorption line and has the same area as the absorption feature. This is expressed as:

$$A_G = S_c \cdot W \tag{6.A}$$

Solving Equation 6.A for W, and plugging in Equation 2.A for W gives:

$$\Delta W = \chi \cdot \frac{A_G}{S_c} \tag{7.A}$$

Then, plugging Equation 1.A in Equation 7.A for ΔW and Equation 5.A for A_G yields:

$$\frac{1.5\sqrt{FWHM \cdot \Delta\lambda_{APS}}}{SNR_{req}} = \chi \cdot \frac{a \cdot FWHM \cdot \frac{\sqrt{2\pi}}{2.35}}{S_c} \tag{8.A}$$

Rearranging for SNR_{req}, and noting that “a” is the amplitude of the Gaussian (the line depth) can be written as “S_c – S_{line},” we get:

$$SNR_{req} = \frac{1.406}{\chi} \cdot \frac{S_c}{S_c - S_{line}} \cdot \sqrt{\frac{\Delta\lambda_{APS}}{FWHM}} \tag{9.A}$$

Equation 9.A is one of the two useful forms for SNR$_{req}$. This one shows the effect of the line depth ratio in the second fraction term. The larger the fraction is, the shallower the feature appears, and the higher the SNR$_{req}$ needs to be. This is shown on the left panel of Figure 11. This form of the equation allows the user to explore the parameter space of the FWHM, $\Delta\lambda_{APS}$, line depth ratio, and the fractional error χ. Another form for SNR$_{req}$ can be obtained by going back to Equation 2.A and only replacing ΔW by Equation 1.A, then again solving for SNR$_{req}$ to yield:

$$SNR_{req} = \frac{1.5\sqrt{FWHM \cdot \Delta\lambda_{APS}}}{\chi \cdot W} \tag{10.A}$$

This form allows the user to explore the parameter space of the FWHM, $\Delta\lambda_{APS}$, equivalent width, and fractional error χ.

Appendix B

Achieved Signal-to-Noise Ratio for Other Stars

The figures below provide the achieved signal-to-noise ratio (SNR_{achi}) for the O_2-A band around other stars. These figures are the counterpart to Figure 3.2 in the text, and followed the same derivation as described in Chapter 2: Methods. These plots demonstrate that, to first order, the time to reach a desired SNR decreases with decreasing stellar luminosity. This is mainly caused by higher contrast ratios with dimmer stellar hosts, for which the star outshines the planet less. This trend may not be linear, as suggested by the oscillation in the required time to achieve a desired SNR in the G and K dwarf plots. The characterization of this trend is beyond the scope of this paper, but can be constrained by considering dimmer stars, such as M dwarfs.

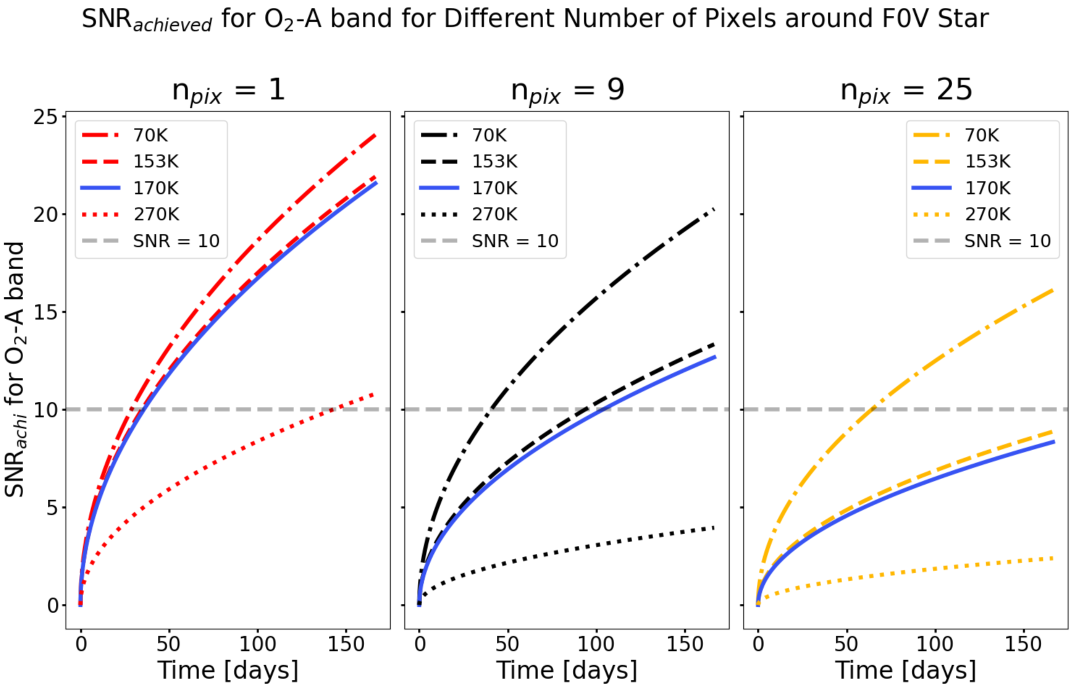

Figure B.1: The plots above show SNR$_{achi}$ for the O$_2$-A band around an F0V star.

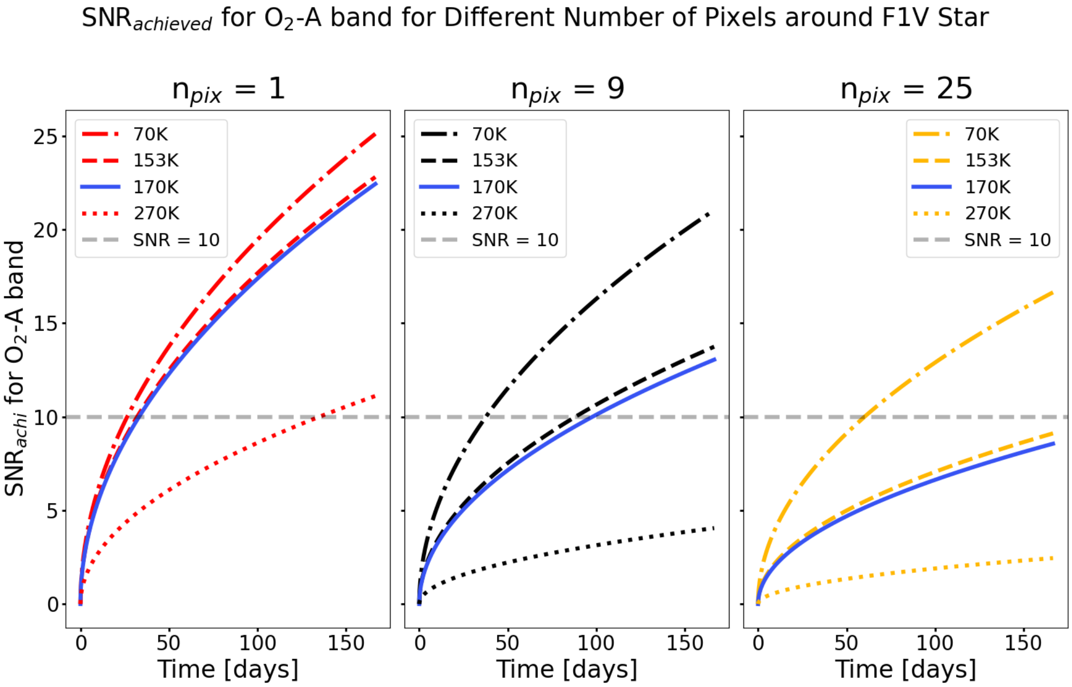

Figure B.2: The plots above show SNR$_{achi}$ for the O$_2$-A band around an F1V star.

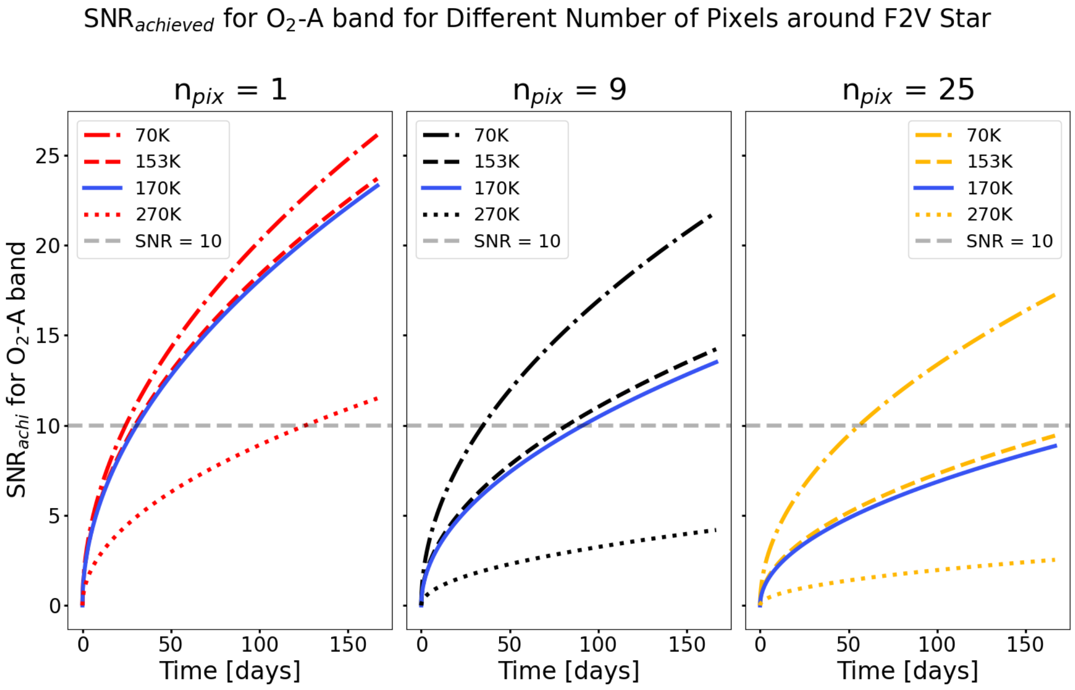

Figure B.3: The plots above show SNR$_{achi}$ for the O$_2$-A band around an F2V star.

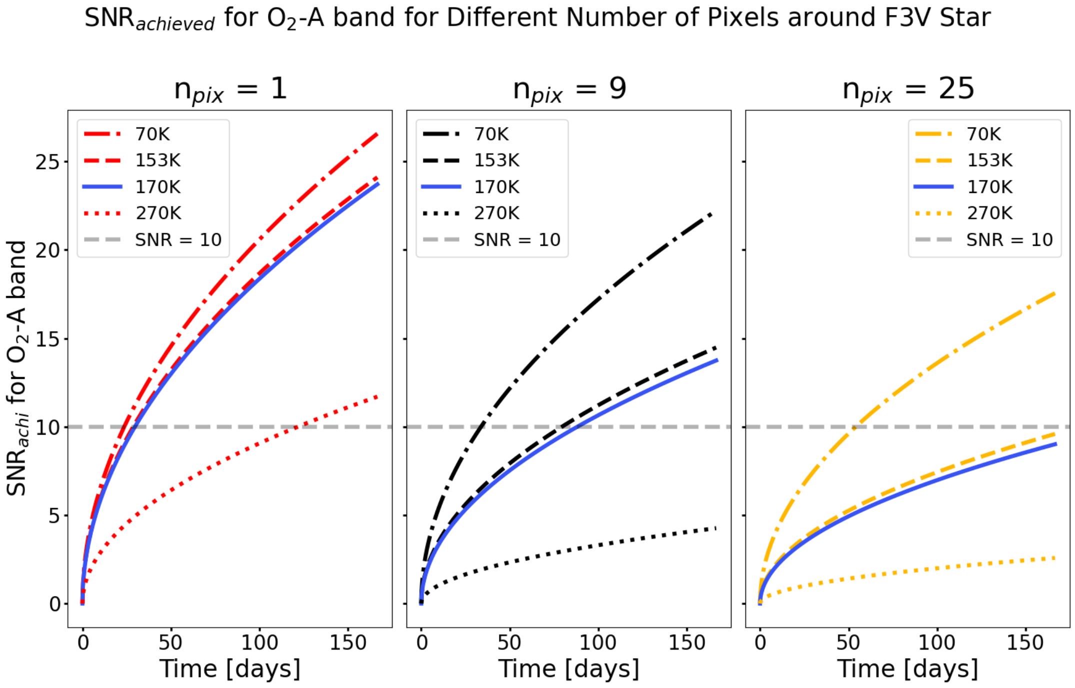

Figure B.4: The plots above show SNR$_{achi}$ for the O$_2$-A band around an F3V star.

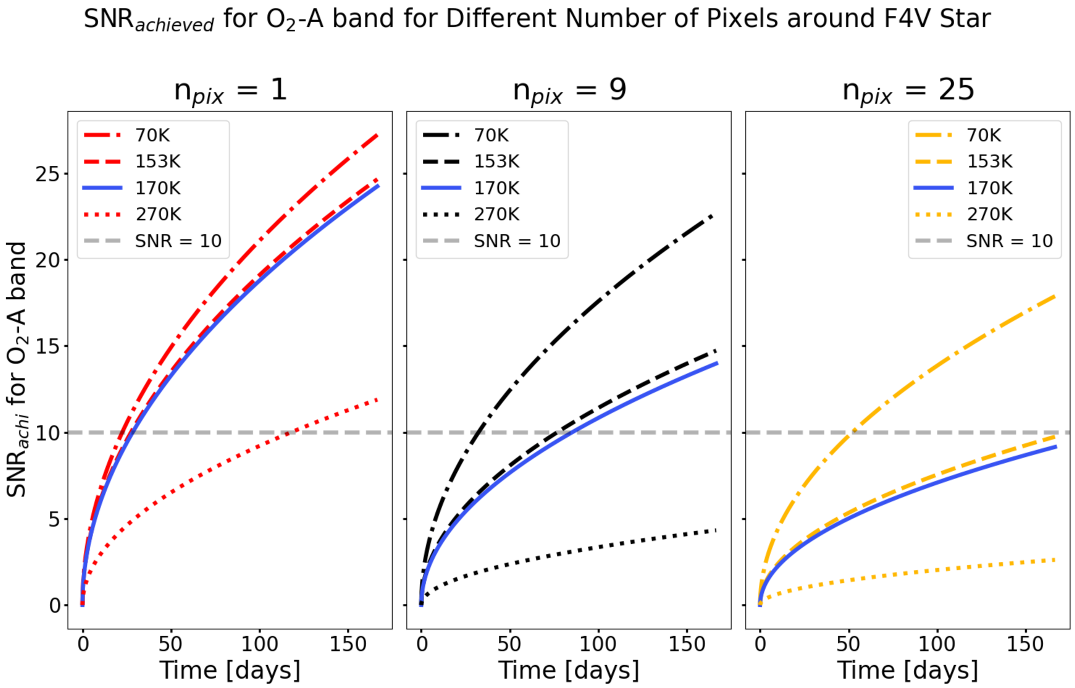

Figure B.5: The plots above show SNR$_{achi}$ for the O$_2$-A band around an F4V star.

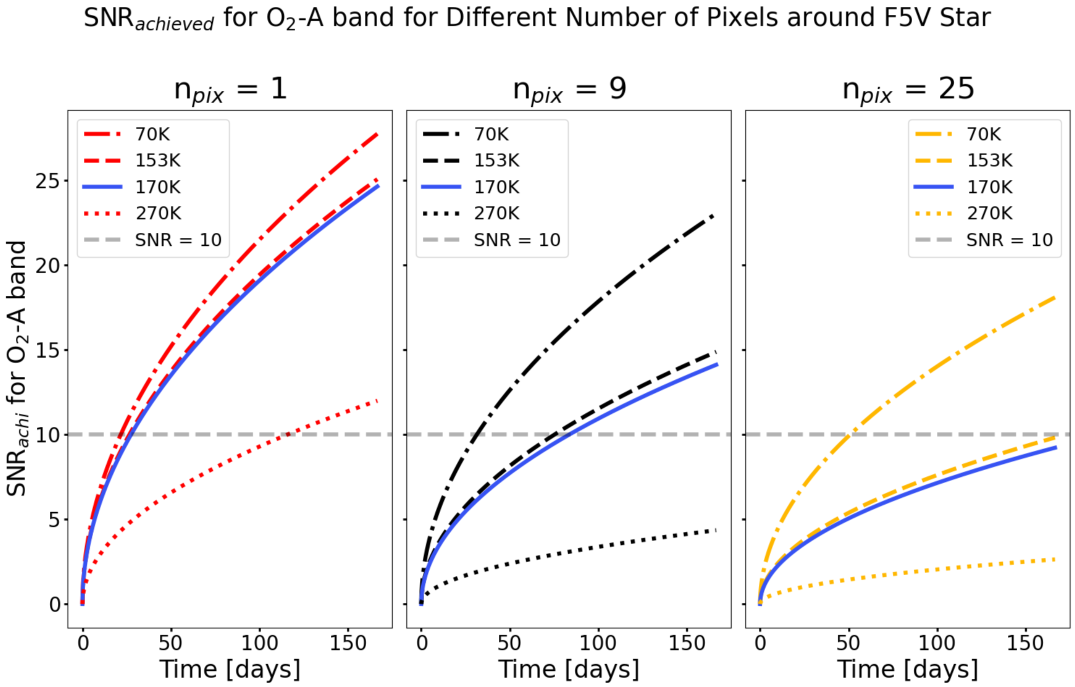

Figure B.6: The plots above show SNR$_{achi}$ for the O$_2$-A band around an F5V star.

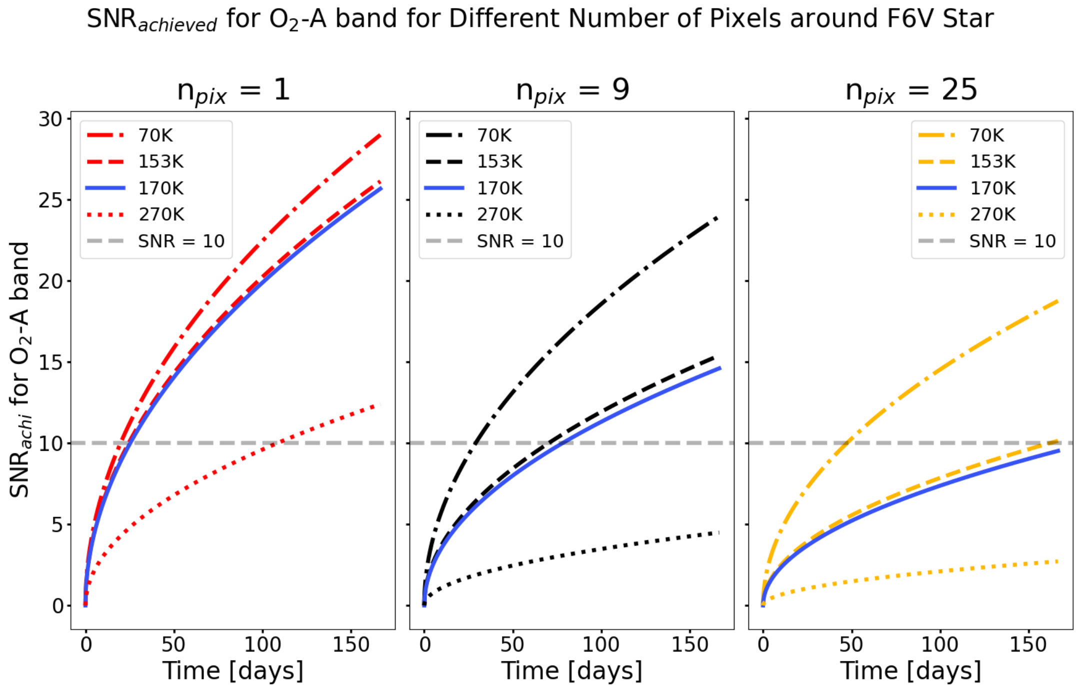

Figure B.7: The plots above show SNR$_{achi}$ for the O$_2$-A band around an F6V star.

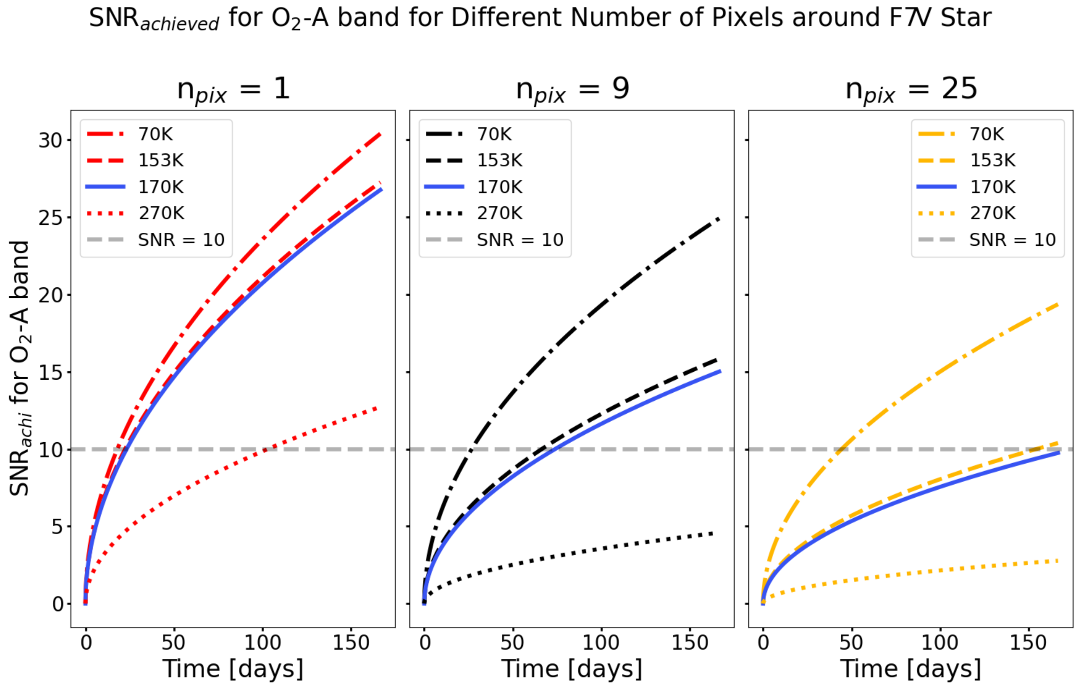

Figure B.8: The plots above show SNR$_{achi}$ for the O$_2$-A band around an F7V star.

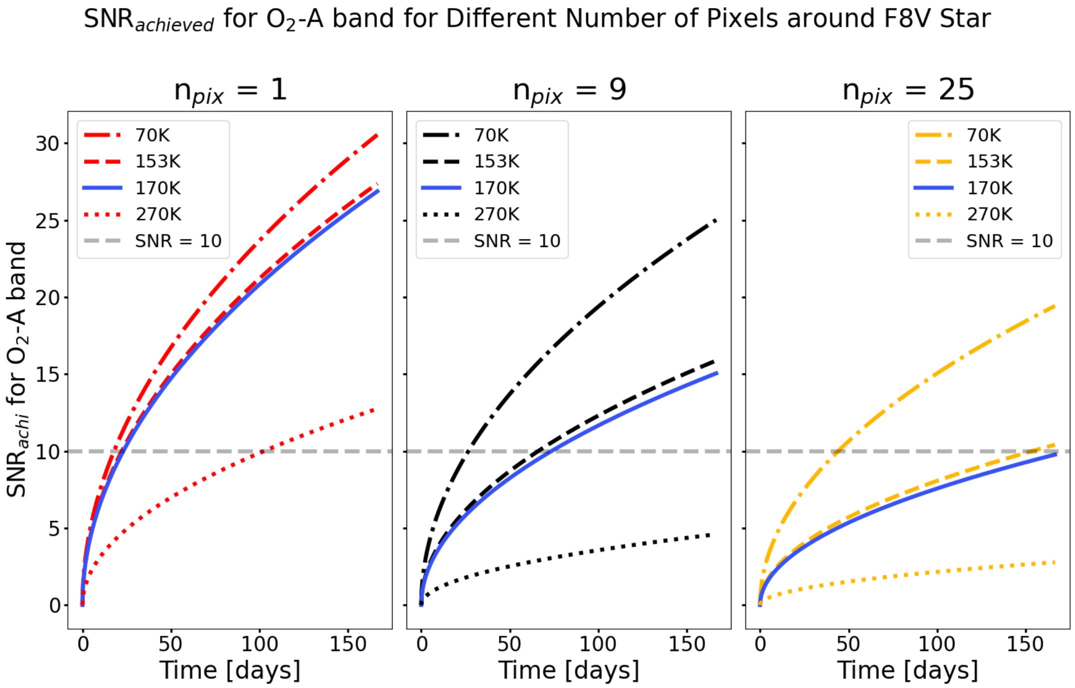

Figure B.9: The plots above show SNR$_{achi}$ for the O$_2$-A band around an F8V star.

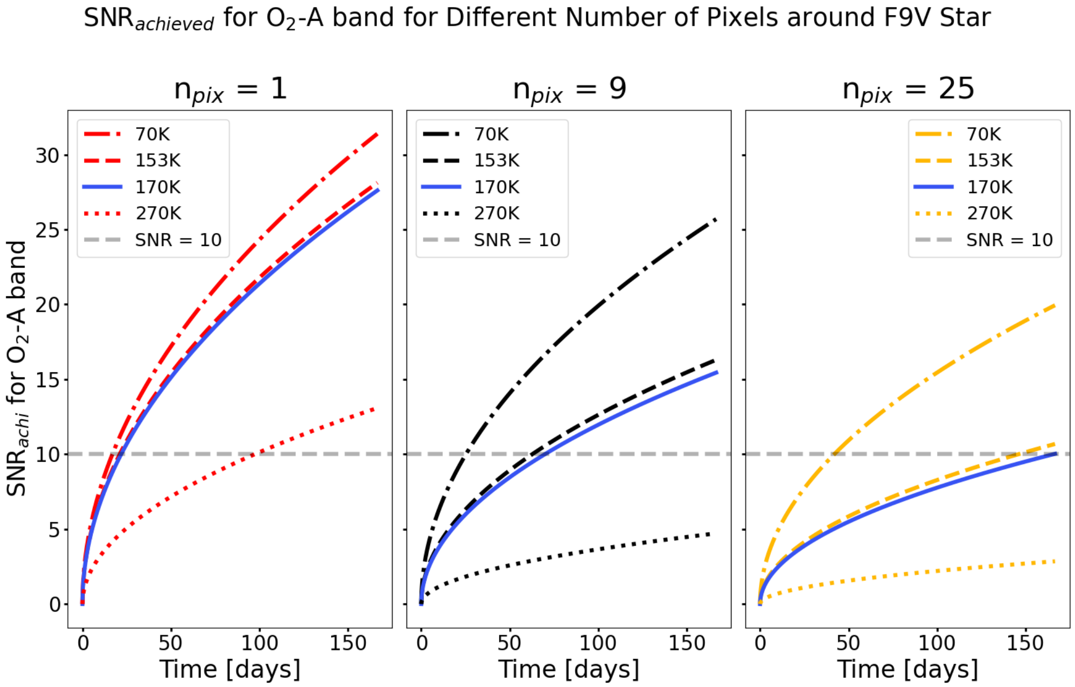

Figure B.10: The plots above show SNR$_{achi}$ for the O$_2$-A band around an F9V star.

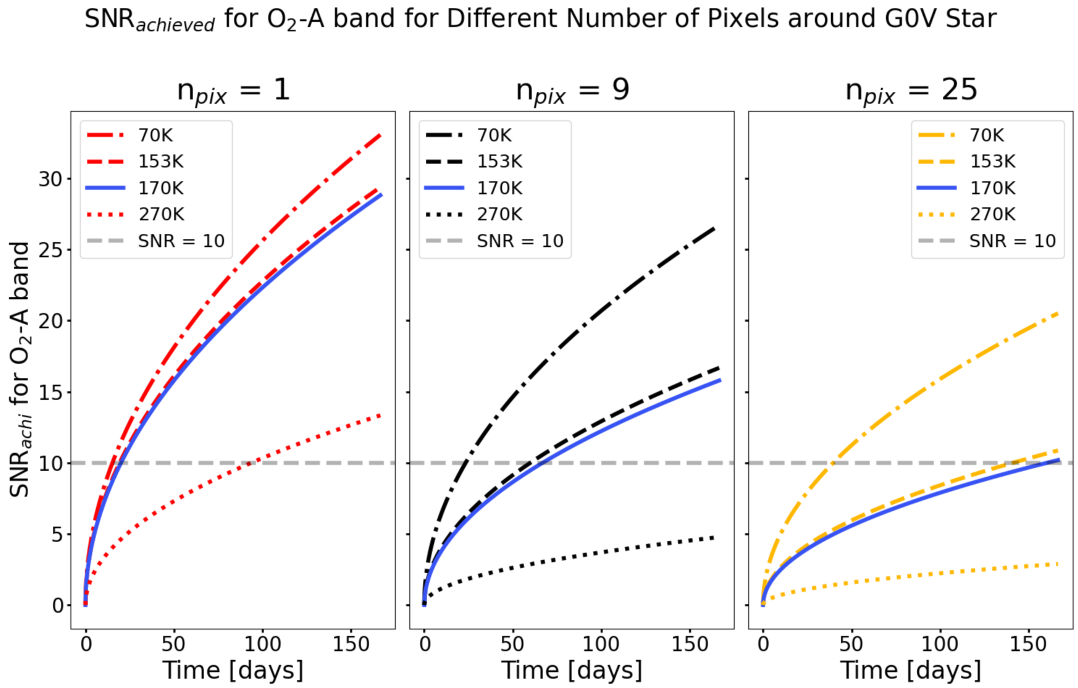

Figure B.11: The plots above show SNR$_{achi}$ for the O$_2$-A band around a G0V star.

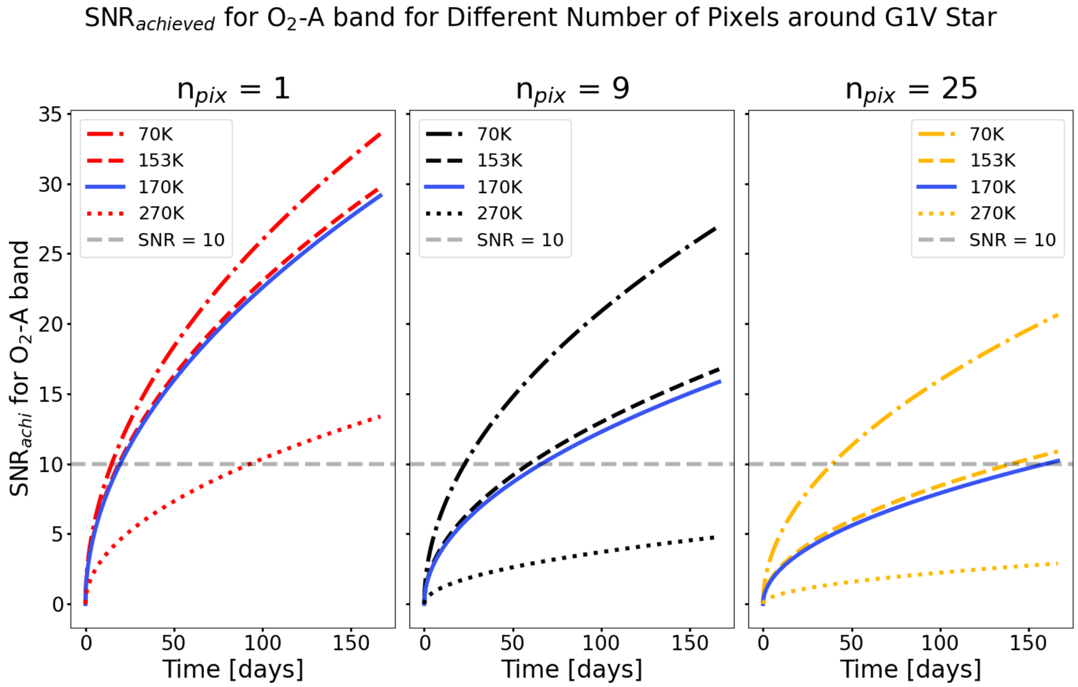

Figure B.12: The plots above show SNR$_{achi}$ for the O$_2$-A band around a G1V star.

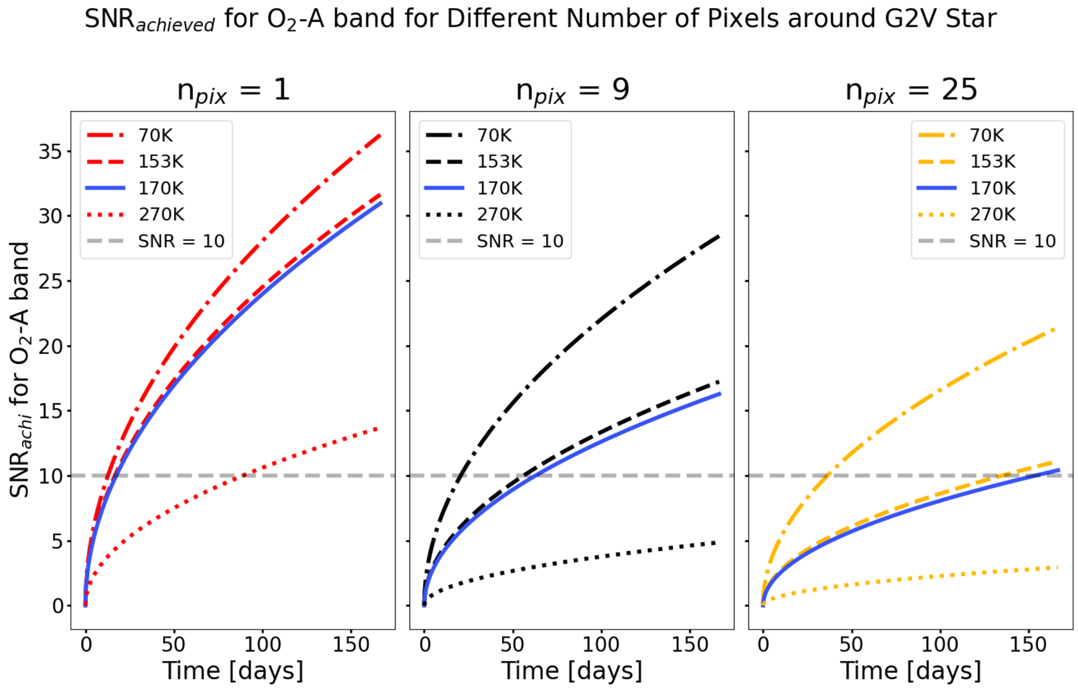

Figure B.13: The plots above show SNR$_{achi}$ for the O$_2$-A band around a G2V star.

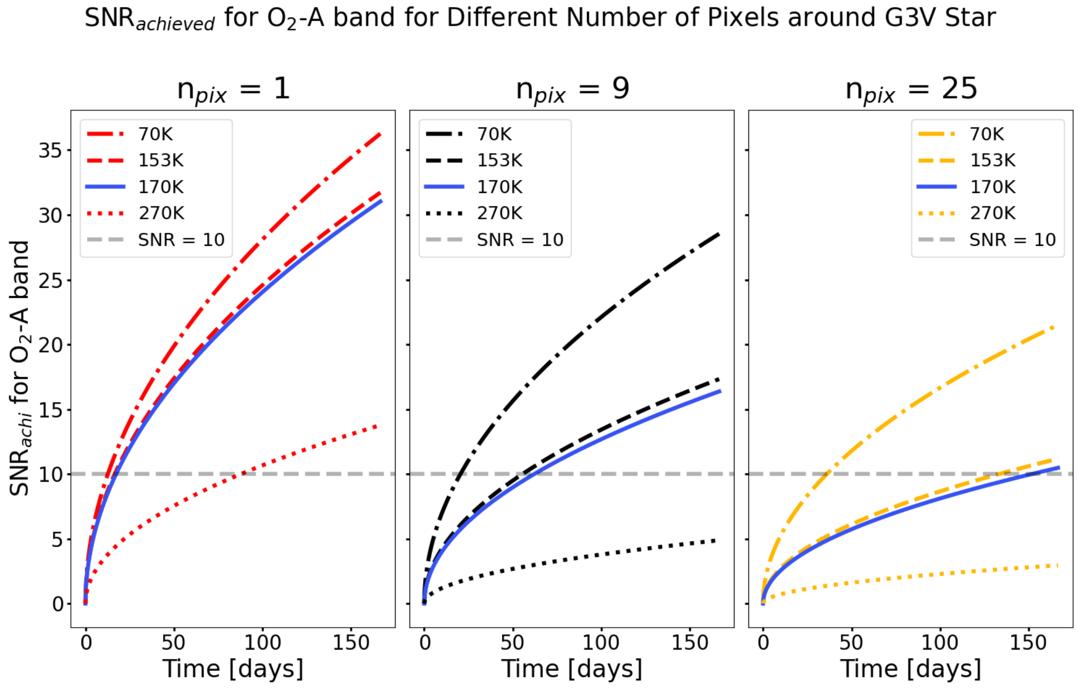

Figure B.14: The plots above show SNR$_{achi}$ for the O$_2$-A band around a G3V star.

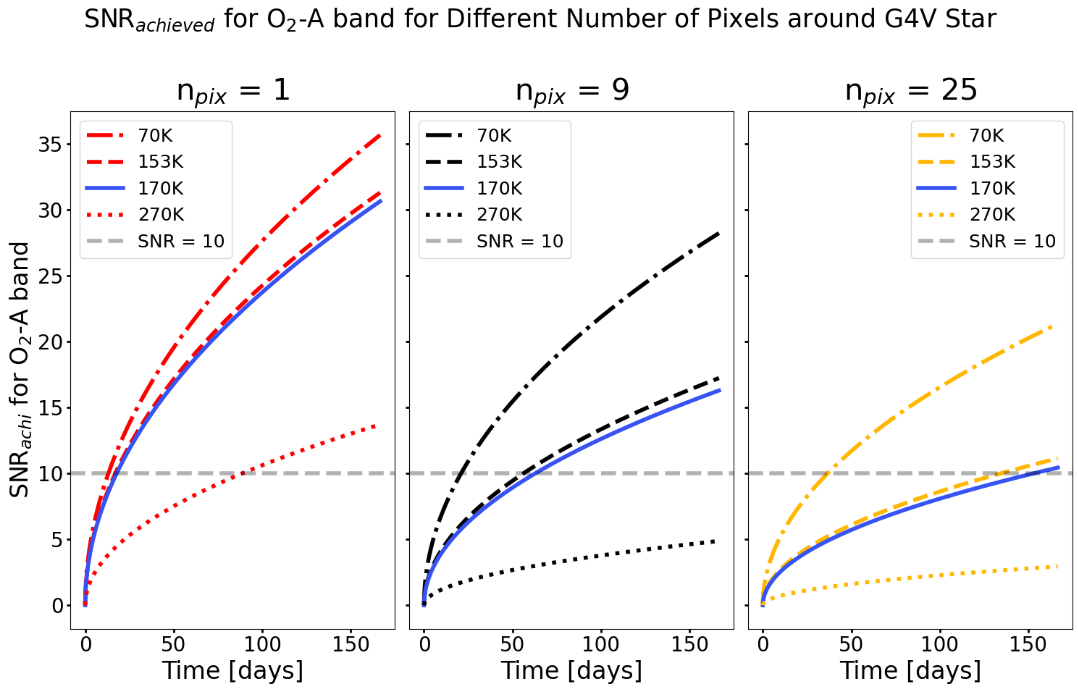

Figure B.15: The plots above show SNR$_{achi}$ for the O$_2$-A band around a G4V star.

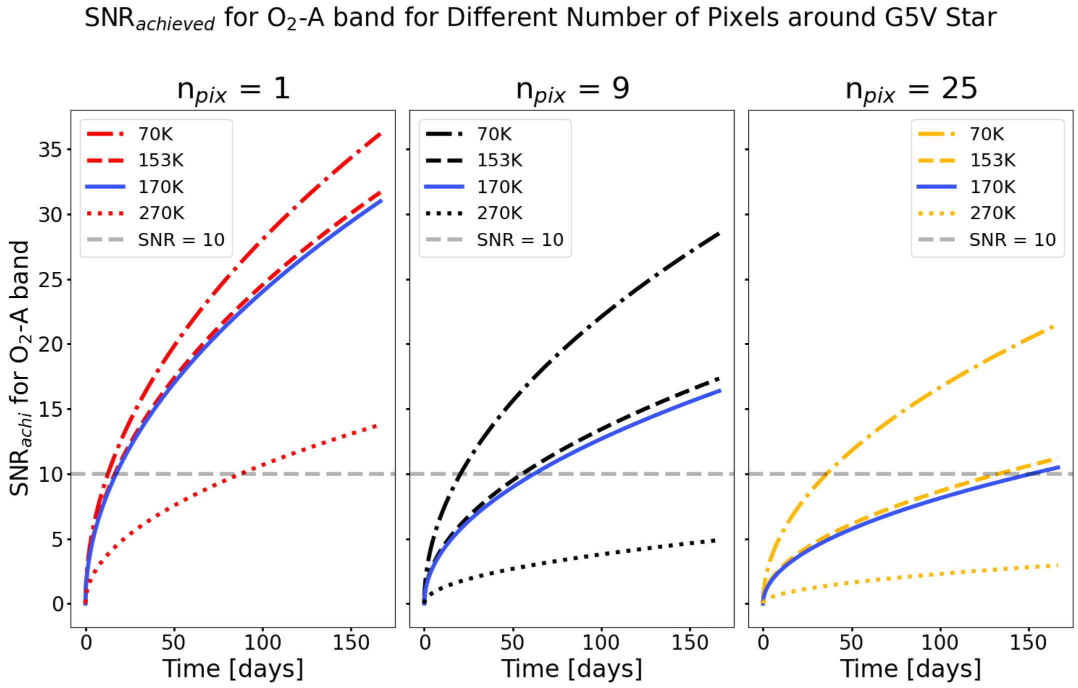

Figure B.16: The plots above show SNR$_{achi}$ for the O$_2$-A band around a G5V star.

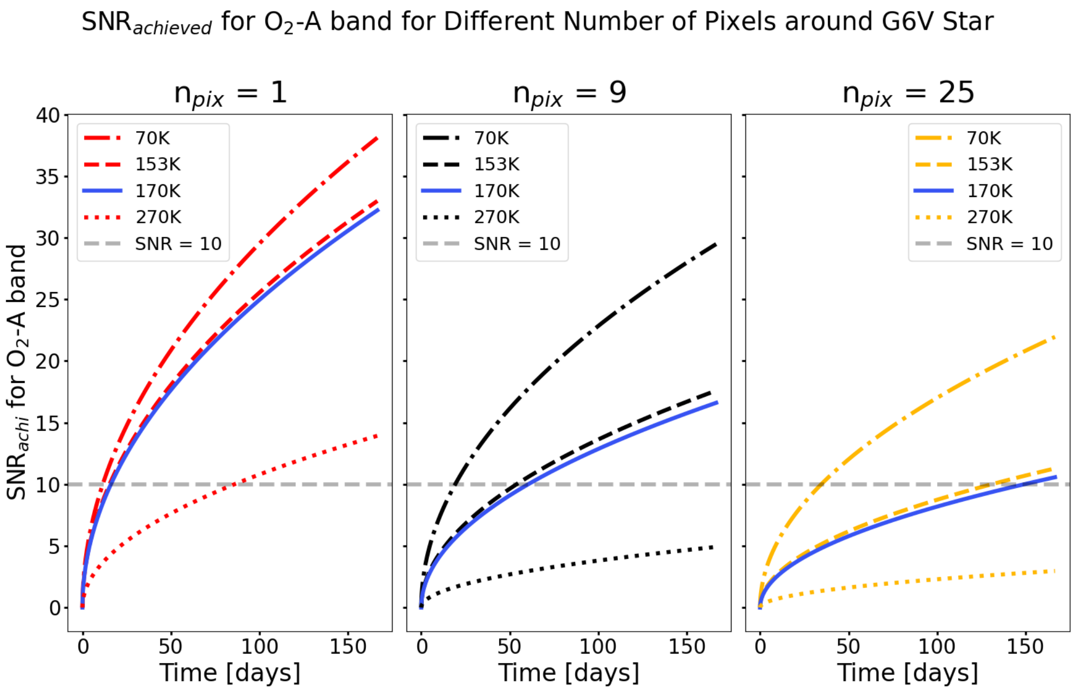

Figure B.17: The plots above show SNR$_{achi}$ for the O$_2$-A band around a G6V star.

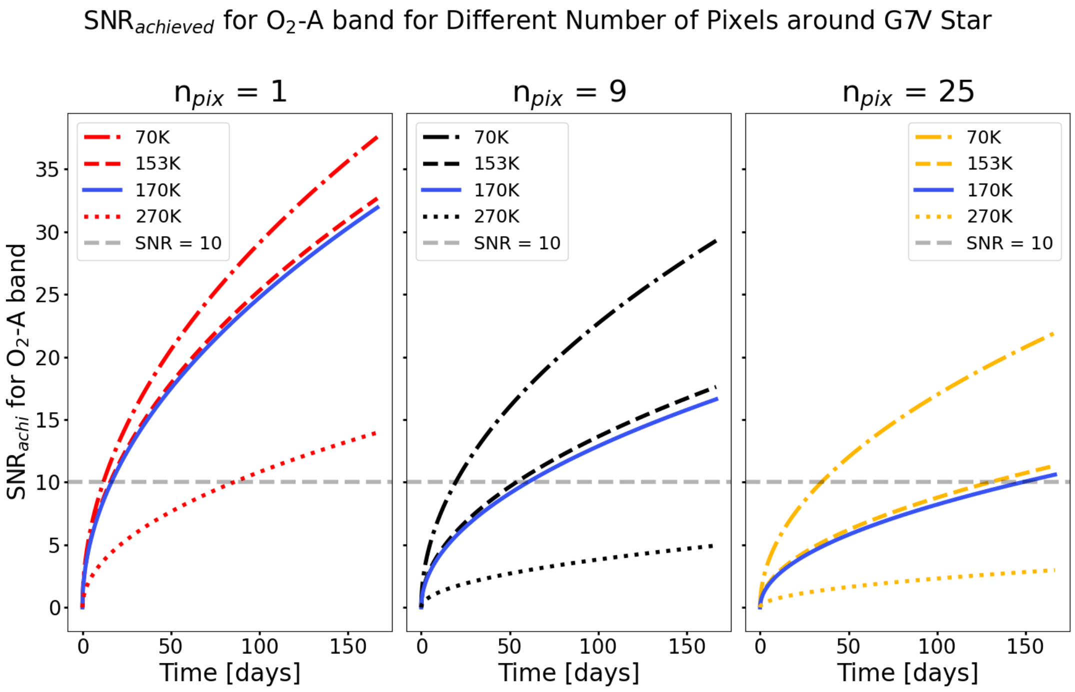

Figure B.18: The plots above show SNR$_{achi}$ for the O$_2$-A band around a G7V star.

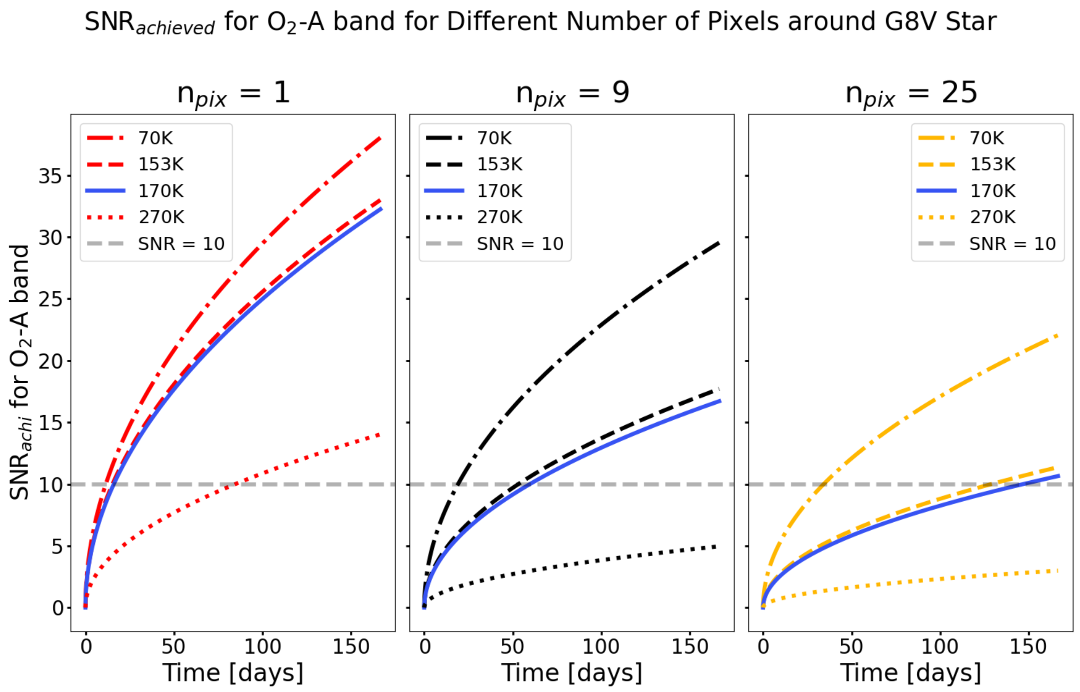

Figure B.19: The plots above show SNR$_{achi}$ for the O_2-A band around a G8V star.

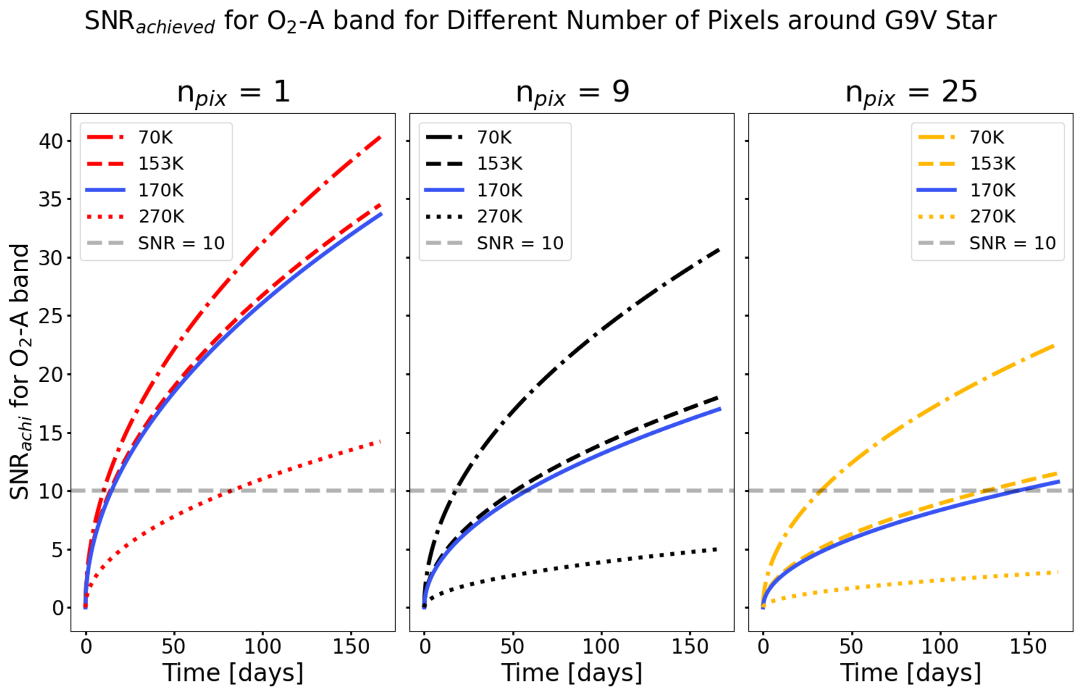

Figure B.20: The plots above show SNR$_{achi}$ for the O_2-A band around a G9V star.

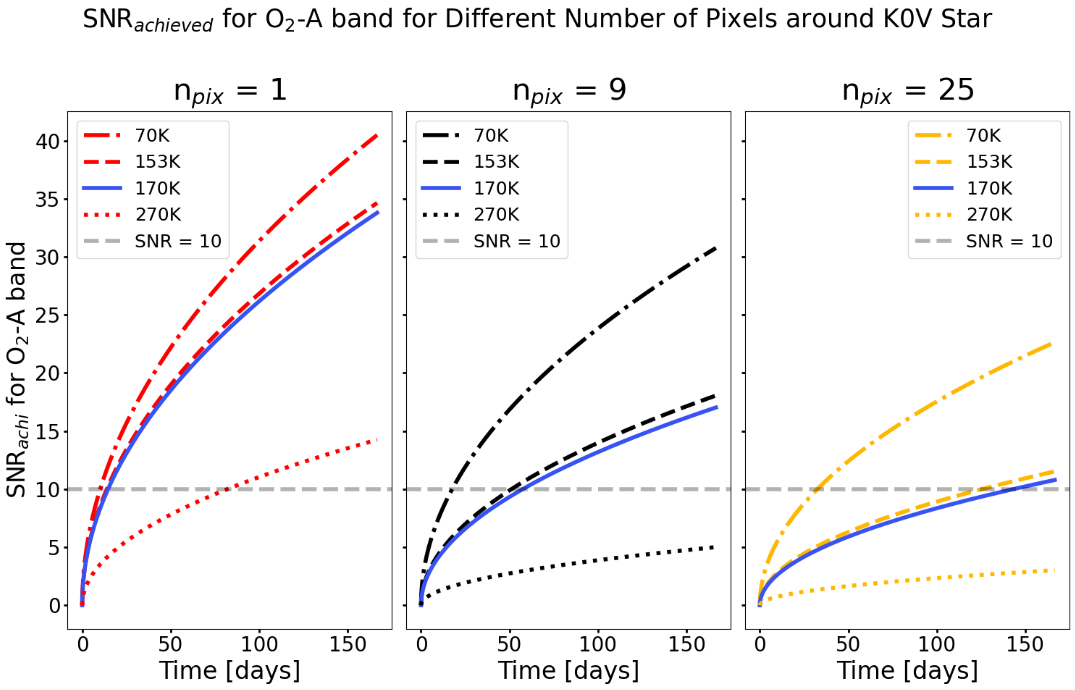

Figure B.21: The plots above show SNR$_{achi}$ for the O$_2$-A band around a K0V star.

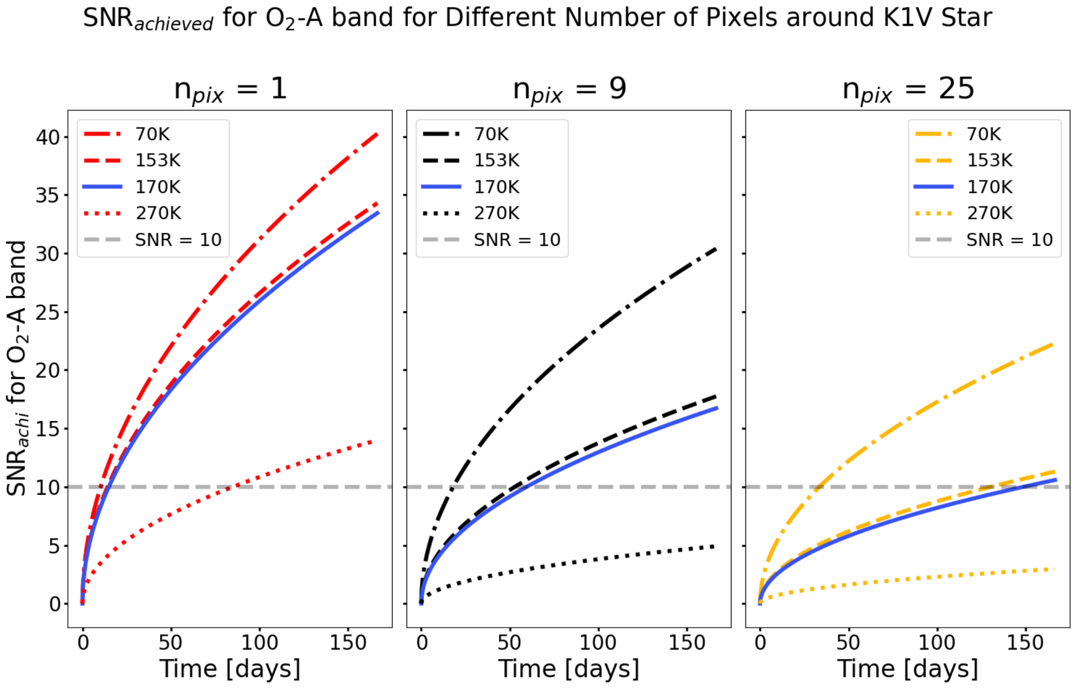

Figure B.22: The plots above show SNR$_{achi}$ for the O$_2$-A band around a K1V star.

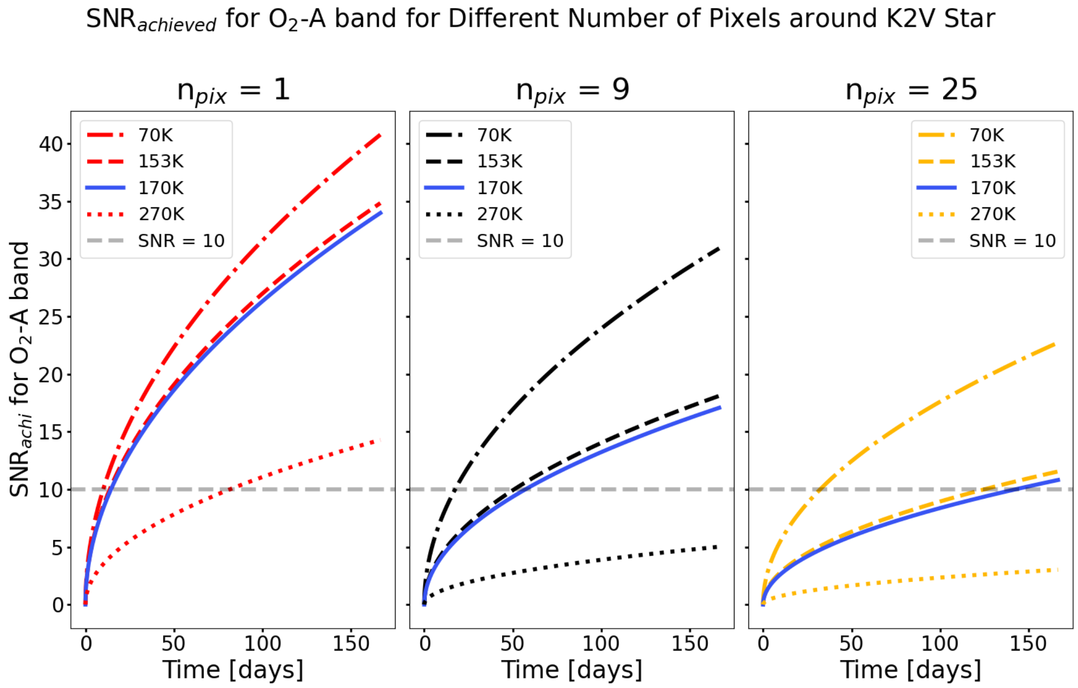

Figure B.23: The plots above show SNR$_{achi}$ for the O$_2$-A band around a K2V star.

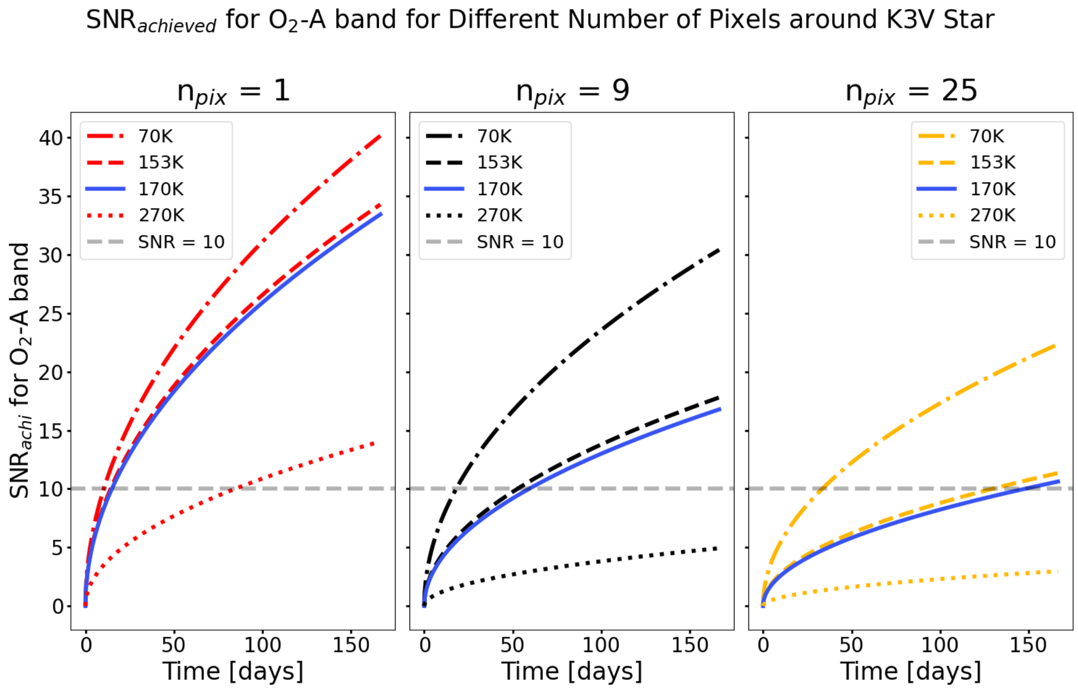

Figure B.24: The plots above show SNR$_{achi}$ for the O$_2$-A band around a K3V star.

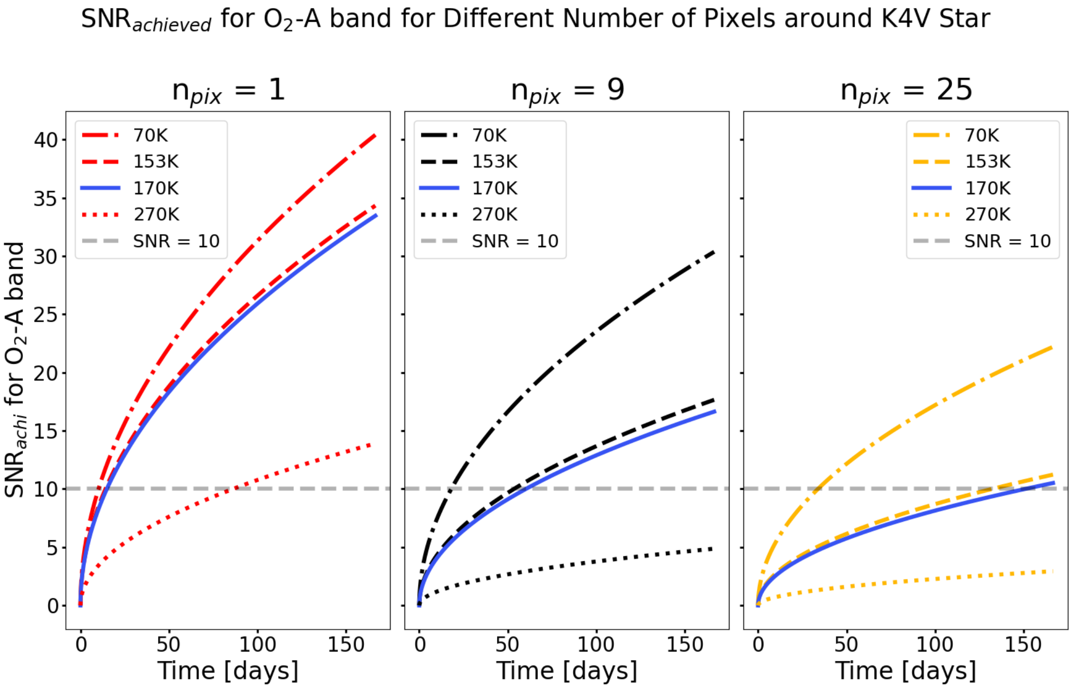

Figure B.25: The plots above show SNR$_{achi}$ for the O$_2$-A band around a K4V star.

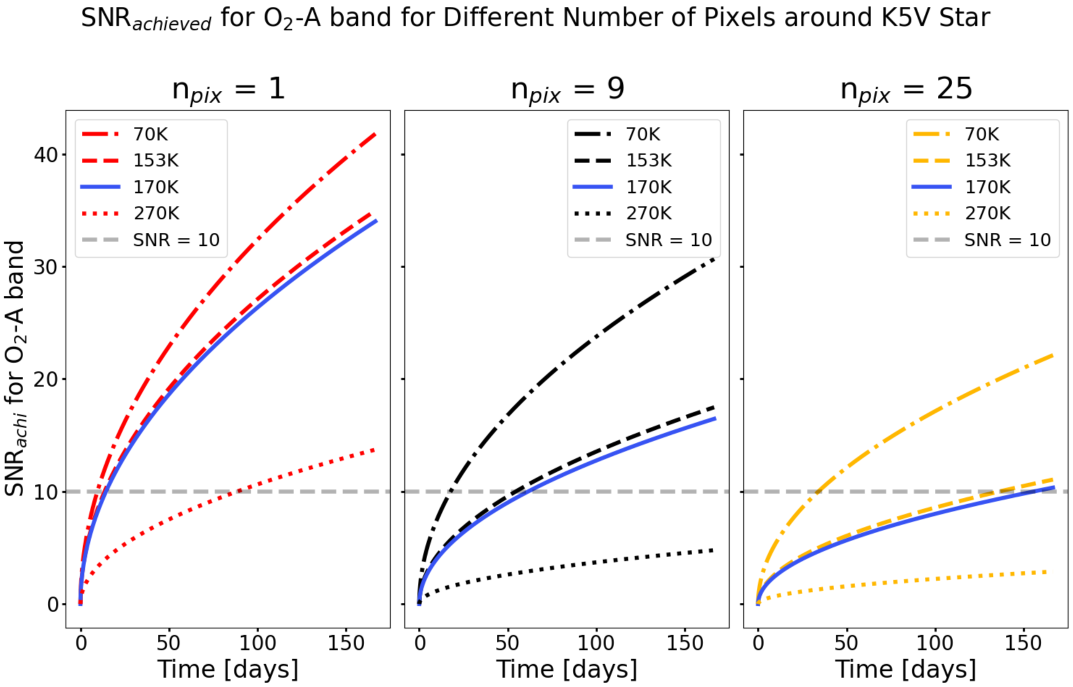

Figure B.26: The plots above show SNR$_{achi}$ for the O$_2$-A band around a K5V star.

Appendix C

Exozodiacal Disk and Planet Orbit around Other Stars

The figures below provide the exozodiacal dust map and planet location around other stars. These figures are the counterpart to Figure 2.8 in the text, and followed the same derivation as described in Chapter 2: Methods. These images demonstrate the effect of stellar type on the location of the habitable zone and its apparent size for different systems at the same distance away. Each pixel in the figures below is 2 milliarcseconds (mas). The inner working angle for LUVOIR-B at 760 nm is 68 mas (32 pixels).

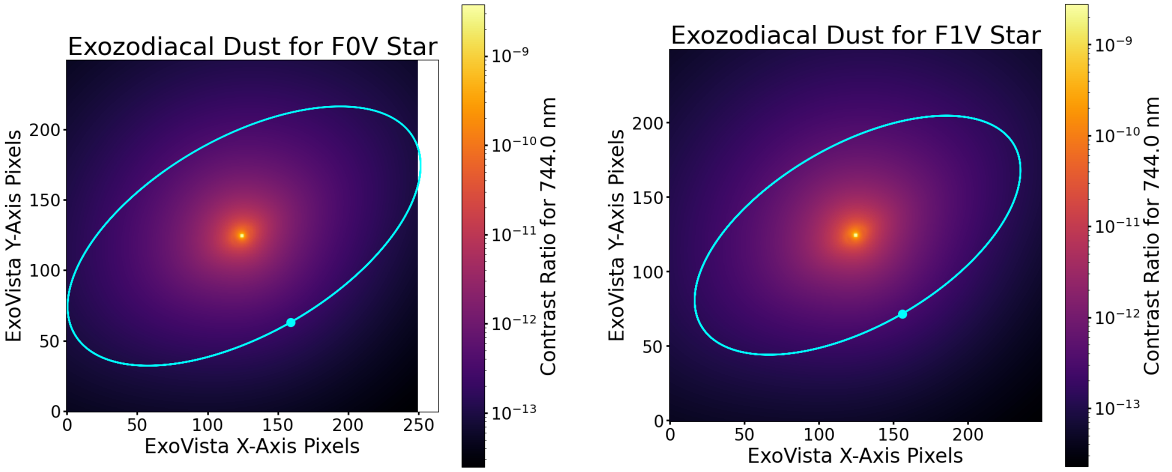

Figure C.1: The images above show the exozodiacal dust maps and exoplanet orbit in the habitable zone of *(left)* an F0V star, and *(right)* an F1V star, at 10 parsecs away.

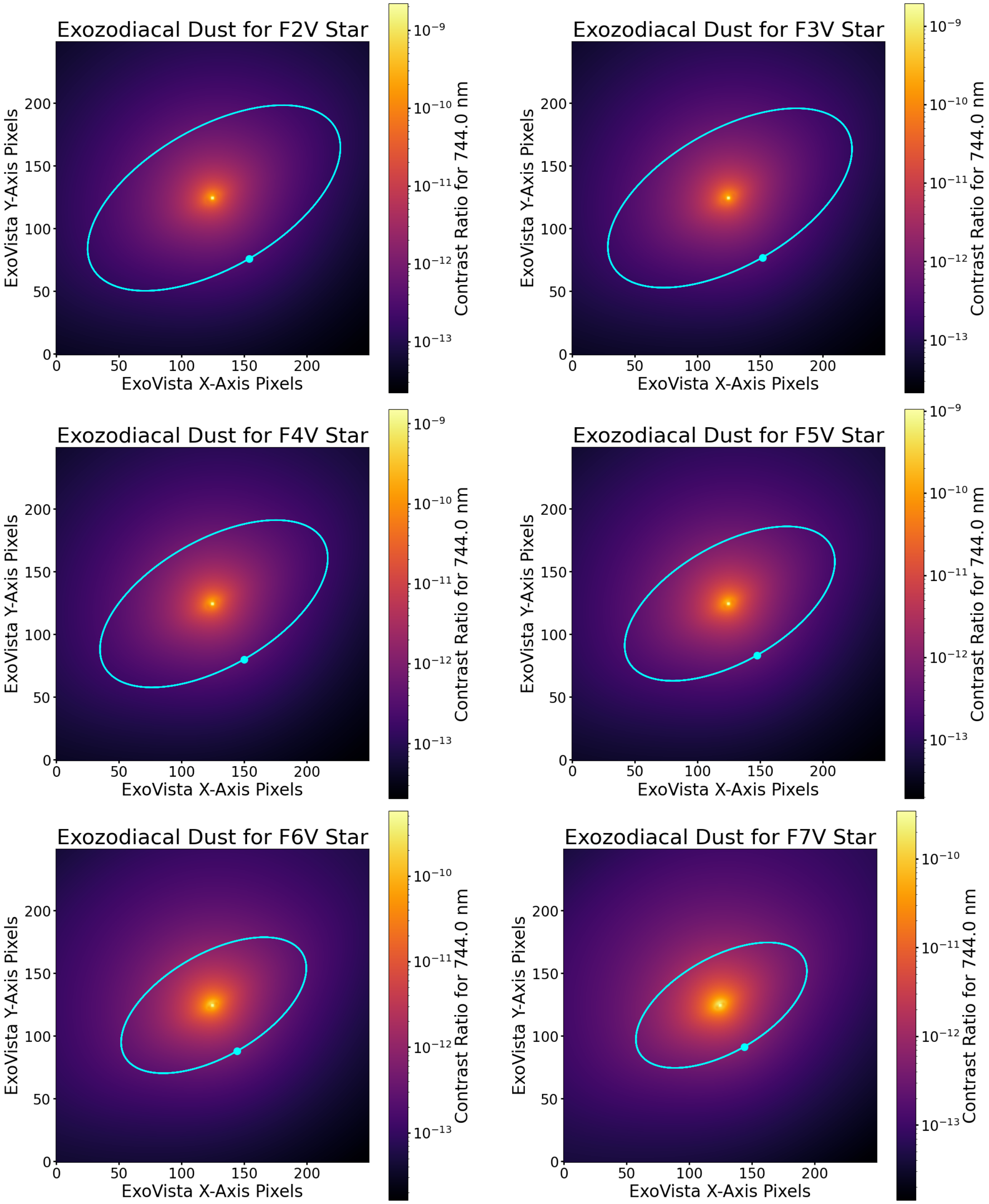

Exozodiacal Dust for F2V Star

Exozodiacal Dust for F3V Star

Exozodiacal Dust for F4V Star

Exozodiacal Dust for F5V Star

Exozodiacal Dust for F6V Star

Exozodiacal Dust for F7V Star

Figure C.2: The images above show the exozodiacal dust maps and exoplanet orbit in the habitable zone of *(top left)* an F2V star, *(top right)* an F3V star, *(center left)* an F4V star, *(center right)* an F5V star, *(bottom left)* an F6V star, and *(bottom right)* an F7V star, at 10 parsecs away.

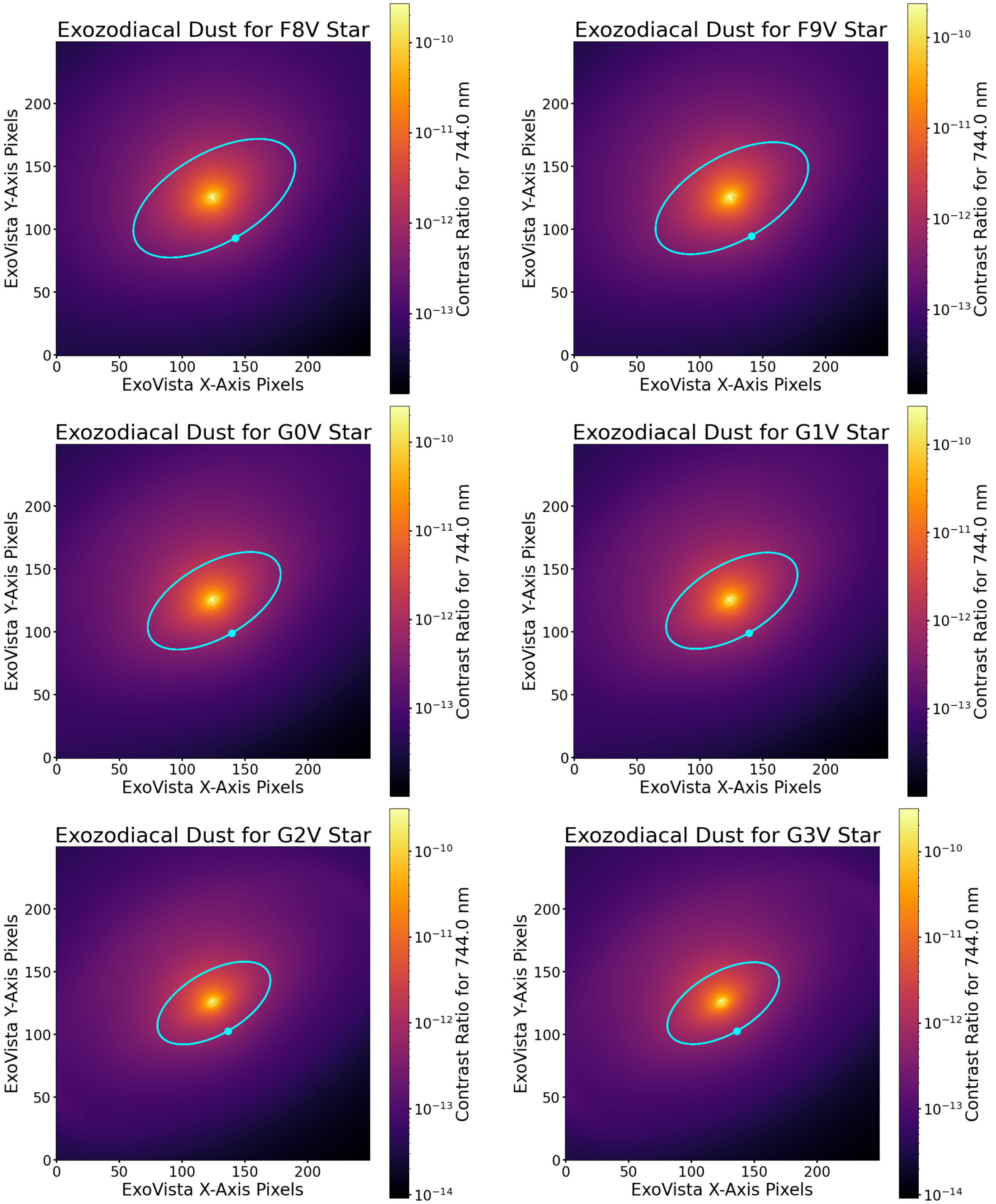

Figure C.3: The images above show the exozodiacal dust maps and exoplanet orbit in the habitable zone of *(top left)* an F8V star, *(top right)* an F9V star, *(center left)* a G0V star, *(center right)* a G1V star, *(bottom left)* a G2V star, and *(bottom right)* a G3V star, at 10 parsecs away.

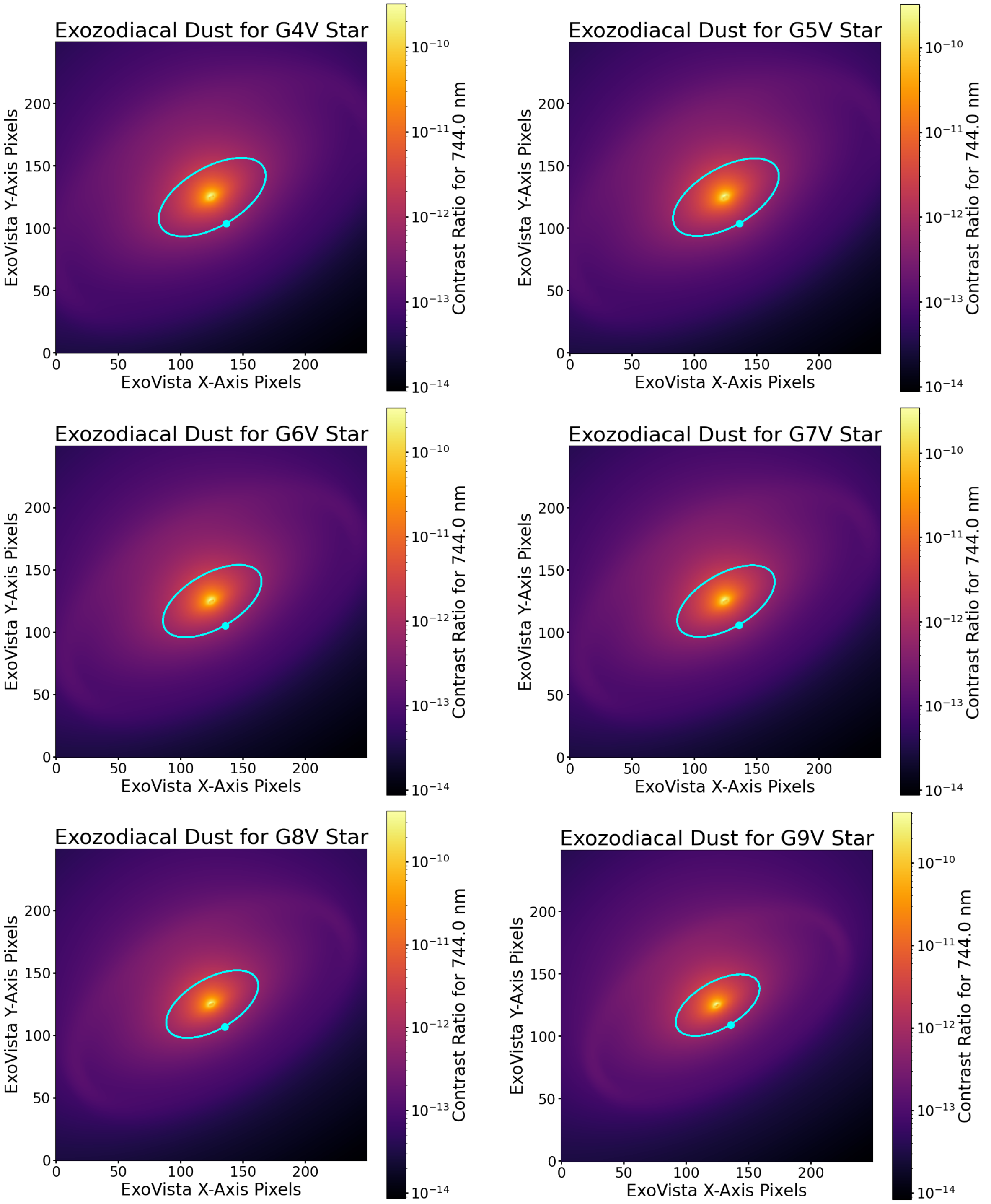

Exozodiacal Dust for G4V Star

Exozodiacal Dust for G5V Star

Exozodiacal Dust for G6V Star

Exozodiacal Dust for G7V Star

Exozodiacal Dust for G8V Star

Exozodiacal Dust for G9V Star

Figure C.4: The images above show the exozodiacal dust maps and exoplanet orbit in the habitable zone of *(top left)* a G4V star, *(top right)* a G5V star, *(center left)* a G6V star, *(center right)* a G7V star, *(bottom left)* a G8V star, and *(bottom right)* an G9V star, at 10 parsecs away.

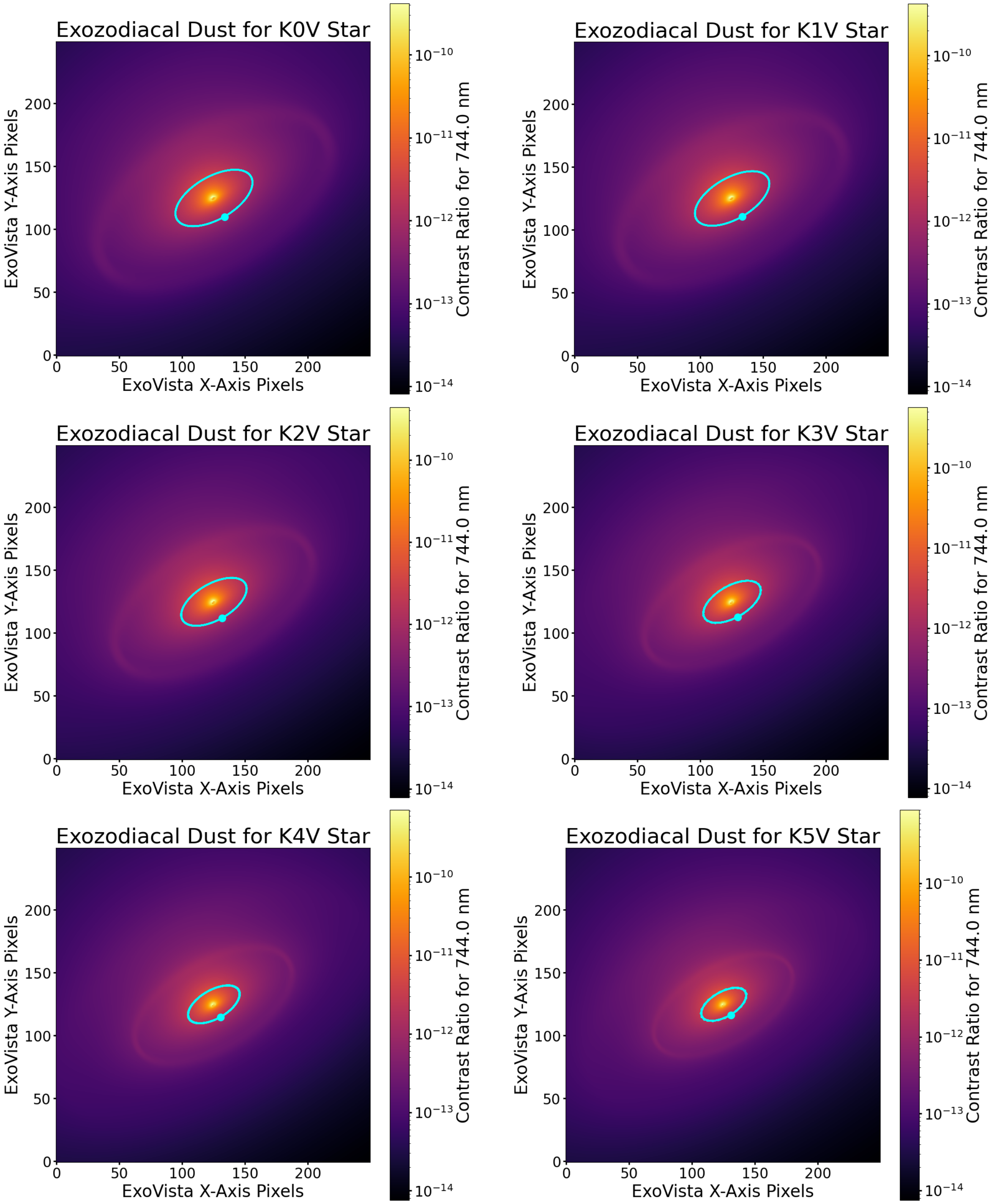

Figure C.5: The images above show the exozodiacal dust maps and exoplanet orbit in the habitable zone of *(top left)* a K0V star, *(top right)* a K1V star, *(center left)* a K2V star, *(center right)* a K3V star, *(bottom left)* a K4V star, and *(bottom right)* an K5V star, at 10 parsecs away.

Appendix D

Using exoVista on a Windows Operating System

The open source software exoVista created by Christopher Stark [78] provides a way to simulate randomized and customized stellar systems. It is available on GitHub at `https://github.com/alexrhowe/ExoVista`, and is maintained by Christopher Stark and Alex Howe. Installation instructions are provided on the GitHub page, along with a PDF document that offers a comprehensive description of the software and its usage. For other works and software developed by Christopher Stark, please visit `https://starkspace.com/`.

Using exoVista on a Windows operating system requires certain prerequisites. The computer must have a C compiler (such as gcc or g++), with Visual Studio recommended as the compiler. Additionally, Python and required packages (such as Cython) must be installed and accessible to exoVista for compiling and executing files. Based on personal experience, I recommend downloading Visual Studio for the C compiler, installing Anaconda to get Python and required packages, and to then proceeding with the installation of exoVista by following the GitHub instructions.

Once exoVista is successfully installed, it is executed through the command line. I strongly suggest using Anaconda's Windows Powershell shortcut (accessible through the Anaconda Navigator) so that the correct environment variable paths are set.

To create a customized system using exoVista, we must first navigate through the command line to reach the folder containing the exoVista code. This folder is chosen by the user upon the installation of exoVista. Specifically, we navigate to the directory that contains the file "solar_system.dat" and the executable "ExoVistaSystem.py". The "solar_system.dat" file contains default parameters for the solar system. This file can be modified to change the star, the distance to the system, the system's inclination, the planets in the system (orbit, albedo), and the zodiacal dust disks. The "ExoVistaSystem.py" executable reads in a data file, such as "solar_system.dat", to create the customized system. Once we are in the directory that contains the executable, type:

```
python ExoVistaSystem.py
```

This command will launch exoVista with the specified data, producing a FITS file that can be opened and manipulated with Python. I recommend using Jupyter Notebooks to explore the data and create plots.

In this work, customized stellar systems for other stars are used in addition to the default "solar_system.dat". To do this, I suggest copying the default file, renaming it to match the stellar type (i.e. K0V, F2V, etc), and then modifying the stellar parameters such as temperature, surface gravity, radius, etc. Next, the exozodiacal dust disk is scaled linearly using the habitable zone equation: Equation 1.5.3. This approach assumes that the nebular hypothesis is correct for the formation of stellar systems, meaning dust forms according to snow lines and temperature gradients in the natal debris disk around the protostar. Finally, as is done in this work, the planet is placed in the habitable zone of its new star. All other default values, such as system inclination and data files for dust and planet albedo, are kept the same.

There are default albedo files and exozodiacal dust files available in exoVista, the sources of which are listed in Table 1 of [78]. Customized files may be used if desired, but must be properly formatted to match the input and output structure within exoVista.

Acknowledgements

This project was supported by The National Aeronautics and Space Administration (NASA) Cosmic Origins (COR) program office under the Strategic Astrophysics Technology (SAT) program Grant No. 80NSSC24K0372. This research has made use of the NASA Exoplanet Archive, which is operated by the California Institute of Technology, under contract with the National Aeronautics and Space Administration under the Exoplanet Exploration Program. This work builds upon research presented on June 19, 2024 at the SPIE Astronomical Telescopes + Instrumentation (AS24) in Yokohama, Japan, with a manuscript submitted to SPIE [85]. We also recognize exoVista [78] as an open source tool for generating realistic planetary systems.

I extend my gratitude to the Astrophysical Sciences and Technology PhD Program faculty, staff, and students for support and guidance. I am deeply grateful to my advisor, Dr. Figer, for his steadfast support, invaluable guidance, and encouragement throughout my research. I thank Justin Gallagher for sharing his expertise about detector technologies, Lazar Buntic for reminding me to sleep, and both for helping me structure my thoughts efficiently. I am indebted to all committee members, Dr. Figer, Dr. Zemcov, and Dr. Ninkov for their willingness to review and provide feedback on this project. I would also like to recognize Cheryl Merrell and program director Dr. Robinson for their assistance and mentorship during my time at RIT.

Finally, and importantly, my heartfelt gratitude goes to my family for their unwavering love and trust in my endeavors. Thank you Fiona for picking up the phone after long days, thank you mom for sending me cat videos, and thank you dad for listening to me talk about space and not *fall asleep* like Fiona used to.

Bibliography

[1] "Pathways to Discovery in Astronomy and Astrophysics for the 2020s," 2021. [Online]. Available: https://nap.nationalacademies.org/catalog/26141/pathways-to-discovery-in-astronomy-and-astrophysics-for-the-2020s 1, 1.4, 1.5.2, 2.4

[2] "HabEx Final Report," Aug. 2019. [Online]. Available: https://www.jpl.nasa.gov/habex/pdf/HabEx-Final-Report-Public-Release.pdf 1, 1.1.2, 2.3

[3] "LUVOIR Final Report," Aug. 2019. [Online]. Available: https://asd.gsfc.nasa.gov/luvoir/reports/LUVOIR_FinalReport_2019-08-26.pdf 1, 1.1.2, 1.4, 2.3, 2.5, 5

[4] T. Currie, B. Biller, A. Lagrange, C. Marois, O. Guyon, E. L. Nielsen, M. Bonnefoy, and R. J. De Rosa, "Direct Imaging and Spectroscopy of Extrasolar Planets," in *Protostars and Planets VII*, ser. Astronomical Society of the Pacific Conference Series, S. Inutsuka, Y. Aikawa, T. Muto, K. Tomida, and M. Tamura, Eds., vol. 534, Jul. 2023, p. 799. [Online]. Available: https://ui.adsabs.harvard.edu/abs/2023ASPC..534..799C 1, 1.1.1

[5] O. Guyon, "Habitable exoplanets detection: overview of challenges and current state-of-the-art;," *Opt. Express*, vol. 25, no. 23, pp. 28 825–28 837, Nov 2017. [Online]. Available: https://opg.optica.org/oe/abstract.cfm?URI=oe-25-23-28825 1, 1.1.1, 1.1.1

[6] C. C. Stark, R. Belikov, M. R. Bolcar, E. Cady, B. P. Crill, S. Ertel, T. Groff, S. Hildebrandt, J. Krist, P. D. Lisman, J. Mazoyer, B. Mennesson, B. Nemati, L. Pueyo, B. J. Rauscher, A. J. Riggs, G. Ruane, S. B. Shaklan, D. Sirbu, R. Soummer, K. S. Laurent, and N. Zimmerman, "ExoEarth yield landscape

for future direct imaging space telescopes," *Journal of Astronomical Telescopes, Instruments, and Systems*, vol. 5, p. 024009, Apr. 2019. [Online]. Available: https://ui.adsabs.harvard.edu/abs/2019JATIS...5b4009S 1, 5

[7] J. Wang, D. Mawet, G. Ruane, J.-R. Delorme, N. Klimovich, and R. Hu, "Baseline requirements for detecting biosignatures with the HabEx and LUVOIR mission concepts," in *Society of Photo-Optical Instrumentation Engineers (SPIE) Conference Series*, ser. Society of Photo-Optical Instrumentation Engineers (SPIE) Conference Series, S. Shaklan, Ed., vol. 10400, Sep. 2017, p. 104000Z. [Online]. Available: https://ui.adsabs.harvard.edu/abs/2017SPIE10400E..0ZW 1, 5

[8] NASA, "2022 Astrophysics Strategic Technology Gaps," 2022. [Online]. Available: https://apd440.gsfc.nasa.gov/images/tech/Tech_Gaps_for_PCOS-COR_2022.xlsx 1

[9] Q. Gong, M. R. Bolcar, J. A. Corsetti, J. A. Crooke, J. Generie, T. D. Groff, J. Hylan, A. Jones, R. J. Parramon, A. M. Mandell, G. J. West, and N. T. Zimmerman, "Optical design of the Extreme Coronagraph for Living Planetary Systems instrument for the LUVOIR mission study," *Journal of Astronomical Telescopes, Instruments, and Systems*, vol. 5, p. 025002, Apr. 2019. [Online]. Available: https://ui.adsabs.harvard.edu/abs/2019JATIS...5b5002G 1, 5

[10] J. F. Kasting, D. P. Whitmire, and R. T. Reynolds, "Habitable Zones around Main Sequence Stars," *Icarus*, vol. 101, no. 1, pp. 108–128, Jan. 1993. [Online]. Available: https://ui.adsabs.harvard.edu/abs/1993Icar..101..108K 1.1.1, 1.5.2

[11] "Terrestrial Planet Finder Coronagraph," Jun. 2006. [Online]. Available: https://exoplanets.nasa.gov/exep/files/exep/STDT_Report_Final_Ex2FF86A.pdf 1.1.1

[12] N. B. Cowan, T. Greene, D. Angerhausen, N. E. Batalha, M. Clampin, K. Colón, I. J. M. Crossfield, J. J. Fortney, B. S. Gaudi, J. Harrington, N. Iro, C. F. Lillie, J. L. Linsky, M. Lopez-Morales, A. M. Mandell, and K. B. Stevenson, "Characterizing Transiting Planet Atmospheres through 2025," *Publications of the*

Astronomical Society of the Pacific, vol. 127, no. 949, p. 311, Mar. 2015. [Online]. Available: https://ui.adsabs.harvard.edu/abs/2015PASP..127..311C 1.1.1

[13] N. JPL, “Exoplanet Exploration Program Science Gap List 2023,” Jun. 2023. [Online]. Available: https://exoplanets.nasa.gov/internal_resources/2749/ExEP_Science_Gap_List_2023_Final.pdf 1.1.1, 1.5.2

[14] R. K. Kopparapu, E. Hébrard, R. Belikov, N. M. Batalha, G. D. Mulders, C. Stark, D. Teal, S. Domagal-Goldman, and A. Mandell, “Exoplanet Classification and Yield Estimates for Direct Imaging Missions,” *Astrophysical Journal*, vol. 856, no. 2, p. 122, Apr. 2018. [Online]. Available: https://ui.adsabs.harvard.edu/abs/2018ApJ...856..122K 1.1.1

[15] C. C. Stark, C. Dressing, S. Dulz, E. Lopez, M. S. Marley, P. Plavchan, and J. Sahlmann, “Toward Complete Characterization: Prospects for Directly Imaging Transiting Exoplanets,” *The Astronomical Journal*, vol. 159, no. 6, p. 286, Jun. 2020. [Online]. Available: https://ui.adsabs.harvard.edu/abs/2020AJ....159..286S 1.1.1, 1.4

[16] P. Baudoz, *Handbook of Exoplanets.* Cham: Springer International Publishing, 2018, ch. Future Exoplanet Research: High-Contrast Imaging Techniques, pp. 3285–3300. [Online]. Available: https://doi.org/10.1007/978-3-319-55333-7_160 1.1.1

[17] R. Juanola-Parramon, N. T. Zimmerman, L. Pueyo, M. R. Bolcar, Q. Gong, T. D. Groff, J. E. Krist, A. Roberge, G. Ruane, and C. C. Stark, “Modeling and performance analysis of the LUVOIR coronagraph instrument,” *Journal of Astronomical Telescopes, Instruments, and Systems*, vol. 8, no. 3, p. 034001, 2022. [Online]. Available: https://doi.org/10.1117/1.JATIS.8.3.034001 1.1.2

[18] J. Olejarz, Y. Iwasa, A. H. Knoll, and M. A. Nowak, “The Great Oxygenation Event as a consequence of ecological dynamics modulated by planetary change,” *Nature Communications*, vol. 12, p. 3985, Jan. 2021. [Online]. Available: https://ui.adsabs.harvard.edu/abs/2021NatCo..12.3985O 1.1.3, 1.5.1

[19] G. Arney, V. Meadows, S. Domagal-Goldman, D. Deming, T. D. Robinson, G. Tovar, E. Wolf, and E. Schwieterman, "Pale Orange Dots: The Impact of Organic Haze on the Habitability and Detectability of Earthlike Exoplanets," in *AAS/Division for Planetary Sciences Meeting Abstracts #48*, ser. AAS/Division for Planetary Sciences Meeting Abstracts, vol. 48, Oct. 2016, p. 122.13. [Online]. Available: https://ui.adsabs.harvard.edu/abs/2016DPS....4812213A 1.1.3

[20] T. D. Brandt and D. S. Spiegel, "Prospects for detecting oxygen, water, and chlorophyll on an exo-Earth," *Proceedings of the National Academy of Science*, vol. 111, no. 37, pp. 13 278–13 283, Sep. 2014. [Online]. Available: https://ui.adsabs.harvard.edu/abs/2014PNAS..11113278B 1.1.3, 2.1

[21] M. Damiano and R. Hu, "Reflected Spectroscopy of Small Exoplanets II: Characterization of Terrestrial Exoplanets," *The Astronomical Journal*, vol. 163, no. 6, p. 299, Jun. 2022. [Online]. Available: https://ui.adsabs.harvard.edu/abs/2022AJ....163..299D 1.1.3, 4

[22] M. Tessenyi, G. Tinetti, G. Savini, and E. Pascale, "Molecular Detectability in Exoplanetary Emission Spectra," in *European Planetary Science Congress*, Sep. 2013, pp. EPSC2013–817. [Online]. Available: https://ui.adsabs.harvard.edu/abs/2013EPSC....8..817T 1.1.3

[23] S. Seager, W. Bains, and J. Petkowski, "Toward a List of Molecules as Potential Biosignature Gases for the Search for Life on Exoplanets and Applications to Terrestrial Biochemistry," *Astrobiology*, vol. 16, no. 6, pp. 465–485, Jun. 2016. [Online]. Available: https://pubmed.ncbi.nlm.nih.gov/27096351/ 1.1.3

[24] S. Seager and D. Deming, "Exoplanet Atmospheres," *Annual Reviews of Astronomy and Astrophysics*, vol. 48, pp. 631–672, Sep. 2010. [Online]. Available: https://ui.adsabs.harvard.edu/abs/2010ARA&A..48..631S 1.1.3, 4

[25] E. W. Schwieterman, N. Y. Kiang, M. N. Parenteau, C. E. Harman, S. DasSarma, T. M. Fisher, G. N. Arney, H. E. Hartnett, C. T. Reinhard, S. L. Olson, V. S.

Meadows, C. S. Cockell, S. I. Walker, J. L. Grenfell, S. Hegde, S. Rugheimer, R. Hu, and T. W. Lyons, "Exoplanet Biosignatures: A Review of Remotely Detectable Signs of Life," *Astrobiology*, vol. 18, no. 6, pp. 663–708, Jun. 2018. [Online]. Available: https://ui.adsabs.harvard.edu/abs/2018AsBio..18..663S 1.1.3, 4

[26] J. L. Grenfell, *Handbook of Exoplanets.* Cham: Springer International Publishing, 2018, ch. Atmospheric Biosignatures, pp. 3159–3172. [Online]. Available: https://doi.org/10.1007/978-3-319-55333-7_68 1.1.3

[27] Y. K. Feng, T. D. Robinson, J. J. Fortney, R. E. Lupu, M. S. Marley, N. K. Lewis, B. Macintosh, and M. R. Line, "Characterizing Earth Analogs in Reflected Light: Atmospheric Retrieval Studies for Future Space Telescopes," *The Astronomical Journal*, vol. 155, no. 5, p. 200, May 2018. [Online]. Available: https://ui.adsabs.harvard.edu/abs/2018AJ....155..200F 1.1.3, 4

[28] V. S. Meadows, C. T. Reinhard, G. N. Arney, M. N. Parenteau, E. W. Schwieterman, S. D. Domagal-Goldman, A. P. Lincowski, K. R. Stapelfeldt, H. Rauer, S. DasSarma, S. Hegde, N. Narita, R. Deitrick, J. Lustig-Yaeger, T. W. Lyons, N. Siegler, and J. L. Grenfell, "Exoplanet Biosignatures: Understanding Oxygen as a Biosignature in the Context of Its Environment," *Astrobiology*, vol. 18, no. 6, pp. 630–662, Jun. 2018. [Online]. Available: https://ui.adsabs.harvard.edu/abs/2018AsBio..18..630M 1.1.3, 4

[29] C. E. Harman and S. Domagal-Goldman, *Handbook of Exoplanets.* Cham: Springer International Publishing, 2018, ch. Biosignature False Positives, pp. 3203–3224. [Online]. Available: https://doi.org/10.1007/978-3-319-55333-7_71 1.1.3, 4

[30] O. Daigle, J. Turcotte, É. Artigau, and R. Doyon, "Preliminary characterization results of a large format 4k × 4k EMCCD," in *High Energy, Optical, and Infrared Detectors for Astronomy VIII*, ser. Society of Photo-Optical Instrumentation Engineers (SPIE) Conference Series, A. D. Holland and J. Beletic, Eds., vol. 10709, Jul. 2018, p. 107090A. [Online]. Available: https://ui.adsabs.harvard.edu/abs/2018SPIE10709E..0AD 1.2

[31] C. J. Marshall, P. W. Marshall, A. Wacynski, E. Polidan, S. D. Johnson, and A. Campbell, "Comparisons of the proton-induced dark current and charge transfer efficiency responses of n- and p-channel CCDs," in *Optical and Infrared Detectors for Astronomy*, ser. Society of Photo-Optical Instrumentation Engineers (SPIE) Conference Series, J. D. Garnett and J. W. Beletic, Eds., vol. 5499, Sep. 2004, pp. 542–552. [Online]. Available: https://ui.adsabs.harvard.edu/abs/2004SPIE.5499..542M 1.2

[32] K. Dawson, C. Bebek, J. Emes, S. Holland, S. Jelinsky, A. Karcher, W. Kolbe, N. Palaio, N. Roe, J. Saha, K. Takasaki, and G. Wang, "Radiation tolerance of fully-depleted p-channel ccds designed for the snap satellite," *IEEE Transactions on Nuclear Science*, vol. 55, no. 3, pp. 1725–1735, 2008. [Online]. Available: https://ieeexplore.ieee.org/document/4545101 1.2

[33] B. J. Rauscher, S. E. Holland, E. Kan, D. Kelly, L. Miko, D. B. Mott, and A. Waczynski, "Radiation tolerant, photon counting, visible, and near-IR detectors for space coronagraphs," in *Space Telescopes and Instrumentation 2022: Optical, Infrared, and Millimeter Wave*, ser. Society of Photo-Optical Instrumentation Engineers (SPIE) Conference Series, L. E. Coyle, S. Matsuura, and M. D. Perrin, Eds., vol. 12180, Aug. 2022, p. 1218065. [Online]. Available: https://ui.adsabs.harvard.edu/abs/2022SPIE12180E..65R 1.2

[34] A. Drlica-Wagner, E. Marrufo Villalpando, J. O'Neil, J. Estrada, S. Holland, N. Kurinsky, T. Li, G. Fernandez Moroni, J. Tiffenberg, and S. Uemura, "Characterization of skipper CCDs for cosmological applications," in *X-Ray, Optical, and Infrared Detectors for Astronomy IX*, ser. Society of Photo-Optical Instrumentation Engineers (SPIE) Conference Series, A. D. Holland and J. Beletic, Eds., vol. 11454, Dec. 2020, p. 114541A. [Online]. Available: https://ui.adsabs.harvard.edu/abs/2020SPIE11454E..1AD 1.2

[35] L. Barak, I. M. Bloch, M. Cababie, G. Cancelo, L. Chaplinsky, F. Chierchie, M. Crisler, A. Drlica-Wagner, R. Essig, J. Estrada, E. Etzion, G. F. Moroni, D. Gift, S. Munagavalasa, A. Orly, D. Rodrigues, A. Singal, M. S. Haro, L. Stefanazzi,

J. Tiffenberg, S. Uemura, T. Volansky, T.-T. Yu, and Sensei Collaboration, "SENSEI: Direct-Detection Results on sub-GeV Dark Matter from a New Skipper CCD," *Physical Review Letters*, vol. 125, no. 17, p. 171802, Oct. 2020. [Online]. Available: https://ui.adsabs.harvard.edu/abs/2020PhRvL.125q1802B 1.2, 1.2

[36] B. A. Cervantes-Vergara, S. Perez, J. C. D'Olivo, J. Estrada, D. J. Grimm, S. Holland, M. Sofo-Haro, and W. Wong, "Skipper-CCDs: Current applications and future," *Nuclear Instruments and Methods in Physics Research A*, vol. 1046, p. 167681, Jan. 2023. [Online]. Available: https://ui.adsabs.harvard.edu/abs/2023NIMPA104667681C 1.2

[37] K. Karatsu, A. Dominjon, T. Fujino, T. Funaki, M. Hazumi, F. Irie, H. Ishino, Y. Kida, T. Matsumura, K. Mizukami, M. Naruse, T. Nitta, T. Noguchi, N. Oka, S. Sekiguchi, Y. Sekimoto, M. Sekine, S. Shu, Y. Yamada, and T. Yamashita, "Radiation Tolerance of Aluminum Microwave Kinetic Inductance Detector," *Journal of Low Temperature Physics*, vol. 184, no. 3-4, pp. 540–546, Aug. 2016. [Online]. Available: https://ui.adsabs.harvard.edu/abs/2016JLTP..184..540K 1.2

[38] G. Ulbricht, M. De Lucia, and E. Baldwin, "Applications for microwave kinetic induction detectors in advanced instrumentation," *Applied Sciences*, vol. 11, no. 6, 2021. [Online]. Available: https://www.mdpi.com/2076-3417/11/6/2671 1.2

[39] A. N. McCaughan, Y. Zhai, B. Korzh, J. P. Allmaras, B. G. Oripov, M. D. Shaw, and S. W. Nam, "The thermally coupled imager: A scalable readout architecture for superconducting nanowire single photon detectors," *Applied Physics Letters*, vol. 121, no. 10, p. 102602, Sep. 2022. [Online]. Available: https://ui.adsabs.harvard.edu/abs/2022ApPhL.121j2602M 1.2

[40] J. Ma, S. Masoodian, D. A. Starkey, and E. R. Fossum, "Photon-number-resolving megapixel image sensor at room temperature without avalanche gain," *Optica*, vol. 4, no. 12, pp. 1474–1481, Dec 2017. [Online]. Available: https://opg.optica.org/optica/abstract.cfm?URI=optica-4-12-1474 1.2

[41] J. P. Gallagher, L. Buntic, D. F. Figer, and W. Deng, “Characterization of single-photon sensing and photon-number resolving CMOS image sensors,” in *X-Ray, Optical, and Infrared Detectors for Astronomy X*, ser. Society of Photo-Optical Instrumentation Engineers (SPIE) Conference Series, A. D. Holland and J. Beletic, Eds., vol. 12191, Aug. 2022, p. 121910T. [Online]. Available: https://ui.adsabs.harvard.edu/abs/2022SPIE12191E..0TG 1.2

[42] J. Gallagher, L. Buntic, W. Deng, E. Fossum, and D. F. Figer, “Radiation Tolerance of a Single Photon Counting CMOS Image Sensor,” *Journal of Astronomical Telescopes, Instruments, and Systems*, 2024, accepted. 1.2, 2.2.2, 2.2.3, 2.2

[43] B. Fowler, X. Liu, and P. Vu, “CMOS Image Sensors - Past Present and Future,” *Society for Imaging Science and Technology*, vol. 132, pp. 134–141, Jan. 2006. [Online]. Available: https://www.imaging.org/common/uploaded%20files/pdfs/Papers/2006/ICIS-0-736/33711.pdf 1.2

[44] Hamamatsu Photonics K.K., “ORCA-Quest qCMOS camera C15550-20UP Technical note,” 2021, document unavailable. [Online]. Available: https://www.hamamatsu.com/content/dam/hamamatsu-photonics/sites/documents/99_SALES_LIBRARY/sys/SCAS0151E_C15550-20UP.pdf 1.2, 1.2, 2.2

[45] Nüvü Cameras, “HNu_1024_v3.4.5,” May 2024. [Online]. Available: https://www.nuvucameras.com/wp-content/uploads/hnu1024v3.4.5.pdf 1.2

[46] B. A. Mazin, S. R. Meeker, M. J. Strader, P. Szypryt, D. Marsden, J. C. van Eyken, G. E. Duggan, A. B. Walter, G. Ulbricht, M. Johnson, B. Bumble, K. O’Brien, and C. Stoughton, “ARCONS: A 2024 Pixel Optical through Near-IR Cryogenic Imaging Spectrophotometer,” *Publications of the Astronomical Society of the Pacific*, vol. 125, no. 933, p. 1348, Nov. 2013. [Online]. Available: https://ui.adsabs.harvard.edu/abs/2013PASP..125.1348M 1.2

[47] K. B. Cho and B. Johnson, “0.5e- rms Read Noise CMOS Image Sensors and Sub-Electron Image Processing for Night Vision Application,” *International Image Sensor Society*, 2023. [Online]. Available: https://doi.org/10.60928/kjuq-vezm 1.2, 2.2.3, 2.2

[48] P. Szypryt, G. E. Duggan, B. A. Mazin, S. R. Meeker, M. J. Strader, J. C. van Eyken, D. Marsden, K. O’Brien, A. B. Walter, G. Ulbricht, T. A. Prince, C. Stoughton, and B. Bumble, “Direct detection of SDSS J0926+3624 orbital expansion with ARCONS,” *Monthly Notices of the Royal Astronomical Society*, vol. 439, no. 3, pp. 2765–2770, Apr. 2014. [Online]. Available: https://ui.adsabs.harvard.edu/abs/2014MNRAS.439.2765S 1.2

[49] J. Crass, A. Bechter, B. Sands, D. King, R. Ketterer, M. Engstrom, R. Hamper, D. Kopon, J. Smous, J. R. Crepp, M. Montoya, O. Durney, D. Cavalieri, R. Reynolds, M. Vansickle, E. Onuma, J. Thomes, S. Mullin, C. Shelton, K. Wallace, E. Bechter, A. Vaz, J. Power, G. Rahmer, and S. Ertel, “Final design and on-sky testing of the iLocater SX acquisition camera: broad-band single-mode fibre coupling,” *Monthly Notices of the Royal Astronomical Society*, vol. 501, no. 2, pp. 2250–2267, Feb. 2021. [Online]. Available: https://ui.adsabs.harvard.edu/abs/2021MNRAS.501.2250C 1.3

[50] N. Jovanovic, N. Cvetojevic, B. Norris, C. Betters, C. Schwab, J. Lozi, O. Guyon, S. Gross, F. Martinache, P. Tuthill, D. Doughty, Y. Minowa, N. Takato, and J. Lawrence, “Demonstration of an efficient, photonic-based astronomical spectrograph on an 8-m telescope,” *Opt. Express*, vol. 25, no. 15, pp. 17 753–17 766, Jul 2017. [Online]. Available: https://opg.optica.org/oe/abstract.cfm?URI=oe-25-15-17753 1.3, 2.1

[51] B. Norris and J. Bland-Hawthorn, “Astrophotonics: The Rise of Integrated Photonics in Astronomy,” *Optics & Photonics News*, vol. 30, no. 5, p. 26, May 2019. [Online]. Available: https://ui.adsabs.harvard.edu/abs/2019OptPN..30...26N 1.3

[52] A. Desmet, A. Radosavljević, J. Missinne, D. Van Thourhout, and G. Van Steenberge, “Laser written glass interposer for fiber coupling to silicon photonic integrated

circuits," *IEEE Photonics Journal*, vol. 13, no. 1, pp. 1–12, 2021. [Online]. Available: https://ui.adsabs.harvard.edu/abs/2021IPhoJ..1339900D 1.3

[53] A. Li, C. Yao, J. Xia, H. Wang, Q. Cheng, R. Penty, Y. Fainman, and S. Pan, "Advances in cost-effective integrated spectrometers," *Nature, Light: Science & Applications*, vol. 11, Jun. 2022. [Online]. Available: https://doi.org/10.1038/s41377-022-00853-1 1.3

[54] N. Cvetojevic, N. Jovanovic, C. Betters, J. S. Lawrence, S. C. Ellis, G. Robertson, and J. Bland-Hawthorn, "First starlight spectrum captured using an integrated photonic micro-spectrograph," *Astronomy & Astrophysics*, vol. 544, p. L1, Aug. 2012. [Online]. Available: https://ui.adsabs.harvard.edu/abs/2012A&A...544L...1C 1.3

[55] P. Gatkine, M. Sitaram, S. Veilleux, M. Dagenais, and J. Bland-Hawthorn, "Development of an integrated near-IR astrophotonic spectrograph," in *Advances in Optical and Mechanical Technologies for Telescopes and Instrumentation IV*, ser. Society of Photo-Optical Instrumentation Engineers (SPIE) Conference Series, R. Navarro and R. Geyl, Eds., vol. 11451, Dec. 2020, p. 114516L. [Online]. Available: https://ui.adsabs.harvard.edu/abs/2020SPIE11451E..6LG 1.3

[56] P. Gatkine, G. Sercel, N. Jovanovic, R. Broeke, K. Ławniczuk, M. Passoni, A. Balakrishnan, S. Bidnyk, J. Yin, J. Jewell, J. K. Wallace, and D. Mawet, "Efficient ultra-broadband low-resolution astrophotonic spectrographs," *Optics Express*, vol. 32, no. 10, p. 17689, May 2024. [Online]. Available: https://ui.adsabs.harvard.edu/abs/2024OExpr..3217689G 1.3, 2.1, 2.1

[57] N. Jovanovic, P. Gatkine, N. Anugu, R. Amezcua-Correa, R. B. Thakur, C. Beichman, C. F. Bender, J.-P. Berger, A. Bigioli, J. Bland-Hawthorn, G. Bourdarot, C. M. Bradford, R. Broeke, J. Bryant, K. Bundy, R. Cheriton, N. Cvetojevic, M. Diab, S. A. Diddams, A. N. Dinkelaker, J. Duis, S. Eikenberry, S. Ellis, A. Endo, D. F. Figer, M. P. Fitzgerald, I. Gris-Sanchez, S. Gross, L. Grossard, O. Guyon, S. Y. Haffert, S. Halverson, R. J. Harris, J. He, T. Herr, P. Hottinger, E. Huby, M. Ireland, R. Jenson-Clem, J. Jewell, L. Jocou, S. Kraus, L. Labadie, S. Lacour, R. Laugier, K. Ławniczuk, J. Lin,

S. Leifer, S. Leon-Saval, G. Martin, F. Martinache, M.-A. Martinod, B. A. Mazin, S. Minardi, J. D. Monnier, R. Moreira, D. Mourard, A. S. Nayak, B. Norris, E. Obrzud, K. Perraut, F. Reynaud, S. Sallum, D. Schiminovich, C. Schwab, E. Serbayn, S. Soliman, A. Stoll, L. Tang, P. Tuthill, K. Vahala, G. Vasisht, S. Veilleux, A. B. Walter, E. J. Wollack, Y. Xin, Z. Yang, S. Yerolatsitis, Y. Zhang, and C.-L. Zou, "2023 astrophotonics roadmap: pathways to realizing multi-functional integrated astrophotonic instruments," *Journal of Physics: Photonics*, vol. 5, no. 4, p. 042501, oct 2023. [Online]. Available: https://dx.doi.org/10.1088/2515-7647/ace869 1.3

[58] R. Marchetti, C. Lacava, L. Carroll, K. Gradkowski, and P. Minzioni, "Coupling strategies for silicon photonics integrated chips," *Photon. Res.*, vol. 7, no. 2, pp. 201–239, Feb 2019. [Online]. Available: https://opg.optica.org/prj/abstract.cfm?URI=prj-7-2-201 1.3

[59] K. K. Mehta and R. J. Ram, "Precise and diffraction-limited waveguide-to-free-space focusing gratings," *Scientific Reports*, vol. 7, May 2017. [Online]. Available: https://ui.adsabs.harvard.edu/abs/2017NatSR...7.2019M 1.3

[60] H. Nishi, T. Tsuchizawa, R. Kou, H. Shinojima, T. Yamada, H. Kimura, Y. Ishikawa, K. Wada, and K. Yamada, "Monolithic integration of a silica AWG and Ge photodiodes on Si photonic platform for one-chip WDM receiver," *Optics Express*, vol. 20, no. 8, p. 9312, Apr. 2012. [Online]. Available: https://ui.adsabs.harvard.edu/abs/2012OExpr..20.9312N 1.3

[61] M. M. Smit and C. van Dam, "Phasar-based wdm-devices: Principles, design and applications," *IEEE Journal of Selected Topics in Quantum Electronics*, vol. 2, pp. 236–250, 1996. [Online]. Available: https://api.semanticscholar.org/CorpusID:45514914 1.3, 1.7

[62] S. Dana, *Arrayed Waveguide Gratings*, ser. Spotlight. SPIE Press, 2016, vol. SL16. [Online]. Available: http://dx.doi.org/10.1117/3.2242852 1.3, 1.7

[63] P. Gatkine, S. Veilleux, and M. Dagenais, "Astrophotonic Spectrographs," *Applied Sciences*, vol. 9, no. 2, p. 290, Jan. 2019. [Online]. Available: https://ui.adsabs.harvard.edu/abs/2019ApSci...9..290G 1.3, 2.1

[64] N. Blind, E. Le coarer, P. Kern, and S. Gousset, "Spectrographs for astrophotonics," *Optics Express*, vol. 25, no. 22, p. 27341, Oct. 2017. [Online]. Available: https://ui.adsabs.harvard.edu/abs/2017OExpr..2527341B 1.3

[65] H. Takahashi, K. Oda, H. Toba, and Y. Inoue, "Transmission characteristics of arrayed waveguide N×N wavelength multiplexer," *Journal of Lightwave Technology*, vol. 13, no. 3, pp. 447–455, Mar. 1995. [Online]. Available: https://ui.adsabs.harvard.edu/abs/1995JLwT...13..447T 1.3

[66] J. W. Valley, "A Cool Early Earth?" *Scientific American*, pp. 58–65, Oct. 2005. [Online]. Available: https://astrobiology.nasa.gov/nai/media/medialibrary/2013/10/Cooler-Early-Earth-Article.pdf 1.5.1

[67] P. Gatkine, S. Veilleux, J. Mather, C. Betters, J. Bland-Hawthorn, J. Bryant, S. B. Cenko, M. Dagenais, D. Deming, S. Ellis, M. Greenhouse, A. Harris, N. Jovanovic, S. Kuhlmann, A. Kutyrev, S. Leon-Saval, K. Madhav, S. Moseley, B. Norris, B. Rauscher, M. Roth, and S. Vogel, "State of the Profession: Astrophotonics," in *Bulletin of the American Astronomical Society*, vol. 51, Sep. 2019, p. 285. [Online]. Available: https://ui.adsabs.harvard.edu/abs/2019BAAS...51g.285G 2.1

[68] P. Gatkine, S. Veilleux, Y. Hu, J. Bland-Hawthorn, and M. Dagenais, "Arrayed waveguide grating spectrometers for astronomical applications: new results," *Optics Express*, vol. 25, no. 15, p. 17918, Jul. 2017. [Online]. Available: https://ui.adsabs.harvard.edu/abs/2017OExpr..2517918G 2.1

[69] P. Gatkine, N. Jovanovic, C. Hopgood, S. Ellis, R. Broeke, K. Ławniczuk, J. Jewell, J. K. Wallace, and D. Mawet, "Potential of commercial SiN MPW platforms for developing mid/high-resolution integrated photonic spectrographs for

astronomy," *Applied Optics*, vol. 60, no. 19, p. D15, Jul. 2021. [Online]. Available: https://ui.adsabs.harvard.edu/abs/2021ApOpt..60D..15G 2.1

[70] N. Jovanovic, Y. Xin, M. P. Fitzgerald, O. Guyon, P. Tuthill, B. Norris, P. Gatkine, G. Sercel, S. Soda, Y. J. Kim, J. Lin, S. Leon-Saval, R. Amezcua-Correa, S. Yerolatsitis, J. Lozi, S. Vievard, C. Betters, S. Sallum, D. Levinstein, D. Mawet, J. Jewell, J. K. Wallace, and N. Cvetojevic, "The path to detecting extraterrestrial life with astrophotonics," *arXiv e-prints*, p. arXiv:2309.08732, Sep. 2023. [Online]. Available: https://ui.adsabs.harvard.edu/abs/2023arXiv230908732J 2.1

[71] P. Gatkine, N. Jovanovic, J. Jewell, J. K. Wallace, and D. Mawet, "A continuously-sampled high-resolution astrophotonic spectrograph using silicon nitride," in *Advances in Optical and Mechanical Technologies for Telescopes and Instrumentation*, ser. Society of Photo-Optical Instrumentation Engineers (SPIE) Conference Series, vol. 12188, Aug. 2022, p. 121882D. [Online]. Available: https://ui.adsabs.harvard.edu/abs/2022SPIE12188E..2DG 2.1

[72] D. J. Blumenthal, R. Heideman, D. Geuzebroek, A. Leinse, and C. Roeloffzen, "Silicon nitride in silicon photonics," *Proceedings of the IEEE*, vol. 106, no. 12, pp. 2209–2231, 2018. [Online]. Available: https://ieeexplore.ieee.org/document/8472140 2.1

[73] J. Gallagher, L. Buntic, E. Alexani, K. Bouthsarath, and D. F. Figer, "Characterizing Radiation-tolerant Single Photon Resolving CMOS Detectors," *Proceedings of the SPIE*, 2024, submitted. [Online]. Available: https://spie.org/astronomical-telescopes-instrumentation/presentation/Characterizing-Radiation-tolerant-Single-Photon-Resolving-CMOS-Detectors/13103-41 2.2.2

[74] Hamamatsu Photonics K.K., "ORCA-Quest qCMOS camera C15550-20UP Technical note," May 2022. [Online]. Available: https://camera.hamamatsu.com/content/dam/hamamatsu-photonics/sites/

documents/99_SALES_LIBRARY/sys/SCAS0154E_C15550-20UP_tec.pdf 2.2.2, 2.2.2, 2.2.2, 2.2.3

[75] T. D. Robinson, K. R. Stapelfeldt, and M. S. Marley, "Characterizing Rocky and Gaseous Exoplanets with 2 m Class Space-based Coronagraphs," *Publications of the Astronomical Society of the Pacific*, vol. 128, no. 960, p. 025003, Feb. 2016. [Online]. Available: https://ui.adsabs.harvard.edu/abs/2016PASP..128b5003R 2.3, 2.5, 4

[76] A. Calamida, J. Mack, J. Medina, C. Shanahan, V. Bajaj, and S. Deustua, "New time-dependent WFC3 UVIS inverse sensitivities," Instrument Science Report WFC3 2021-4, 33 pages, p. 4, Feb. 2021. [Online]. Available: https://ui.adsabs.harvard.edu/abs/2021wfc..rept....4C 2.4

[77] "The LUVOIR Final Report Appendices," Aug. 2019. [Online]. Available: https://asd.gsfc.nasa.gov/luvoir/reports/LUVOIR_FinalReportAppendices_2019-08-26.pdf 2.4

[78] C. C. Stark, "ExoVista: A Suite of Planetary System Models for Exoplanet Studies," *The Astronomical Journal*, vol. 163, no. 3, p. 105, Mar. 2022. [Online]. Available: https://ui.adsabs.harvard.edu/abs/2022AJ....163..105S 2.5, 2.5, 2.5, D, 5

[79] A. Roberge, M. J. Rizzo, A. P. Lincowski, G. N. Arney, C. C. Stark, T. D. Robinson, G. F. Snyder, L. Pueyo, N. T. Zimmerman, T. Jansen, E. R. Nesvold, V. S. Meadows, and M. C. Turnbull, "Finding the Needles in the Haystacks: High-fidelity Models of the Modern and Archean Solar System for Simulating Exoplanet Observations," *Publications of the Astronomical Society of the Pacific*, vol. 129, no. 982, p. 124401, Dec. 2017. [Online]. Available: https://ui.adsabs.harvard.edu/abs/2017PASP..129l4401R 2.5

[80] F. Castelli and R. L. Kurucz, "Is missing Fe I opacity in stellar atmospheres a significant problem?" *Astronomy and Astrophysics*, vol. 419, pp. 725–733, May 2004. [Online]. Available: https://ui.adsabs.harvard.edu/abs/2004A&A...419..725C 2.5

[81] S. Ertel, D. Defrère, P. Hinz, B. Mennesson, G. M. Kennedy, W. C. Danchi, C. Gelino, J. M. Hill, W. F. Hoffmann, J. Mazoyer, G. Rieke, A. Shannon, K. Stapelfeldt,

E. Spalding, J. M. Stone, A. Vaz, A. J. Weinberger, P. Willems, O. Absil, P. Arbo, V. P. Bailey, C. Beichman, G. Bryden, E. C. Downey, O. Durney, S. Esposito, A. Gaspar, P. Grenz, C. A. Haniff, J. M. Leisenring, L. Marion, T. J. McMahon, R. Millan-Gabet, M. Montoya, K. M. Morzinski, S. Perera, E. Pinna, J. U. Pott, J. Power, A. Puglisi, A. Roberge, E. Serabyn, A. J. Skemer, K. Y. L. Su, V. Vaitheeswaran, and M. C. Wyatt, "The HOSTS Survey for Exozodiacal Dust: Observational Results from the Complete Survey," *The Astronomical Journal*, vol. 159, no. 4, p. 177, Apr. 2020. [Online]. Available: https://ui.adsabs.harvard.edu/abs/2020AJ....159..177E 2.5

[82] C. C. Stark, A. Roberge, A. Mandell, and T. D. Robinson, "Maximizing the ExoEarth Candidate Yield from a Future Direct Imaging Mission," *Astrophysical Journal*, vol. 795, no. 2, p. 122, Nov. 2014. [Online]. Available: https://ui.adsabs.harvard.edu/abs/2014ApJ...795..122S 2.5, 3.1, 4

[83] R. Cayrel, "Data Analysis," in *The Impact of Very High S/N Spectroscopy on Stellar Physics*, G. Cayrel de Strobel and M. Spite, Eds., vol. 132, Jan. 1988, p. 345. [Online]. Available: https://ui.adsabs.harvard.edu/abs/1988IAUS..132..345C 2.5, A

[84] I. Snellen, R. de Kok, J. L. Birkby, B. Brandl, M. Brogi, C. Keller, M. Kenworthy, H. Schwarz, and R. Stuik, "Combining high-dispersion spectroscopy with high contrast imaging: Probing rocky planets around our nearest neighbors," *Astronomy & Astrophysics*, vol. 576, p. A59, Apr. 2015. [Online]. Available: https://ui.adsabs.harvard.edu/abs/2015A&A...576A..59S 3.1

[85] E. Alexani, D. F. Figer, and P. Gatkine, "Simulation of a single photon counting photonic spectrograph for exoplanet atmospheric characterization," *Proceedings of the SPIE*, 2024, submitted. [Online]. Available: https://spie.org/astronomical-telescopes-instrumentation/presentation/Simulation-of-a-Single-Photon-Counting-Photonic-Spectrograph-for-Exoplanet/13092-154 5